Revista Brasileira de Ciências Mecânicas

Journal of the Brazilian Society of Mechanical Sciences

1

PUBLICAÇÃO DA ABCM - ASSOCIAÇÃO BRASILEIRA DE CIÊNCIAS MECÂNICAS

VOL. XV - Nº 1 - 1993

ISSN 0100-738

REVISTA BRASILEIRA DE CIÊNCIAS MECÂNICAS
JOURNAL OF THE BRAZILIAN SOCIETY OF MECHANICAL SCIENCES

REVISTA BRASILEIRA DE CIÊNCIAS MECÂNICAS
JOURNAL OF THE BRAZILIAN SOCIETY OF MECHANICAL SCIENCES
Vol. 1. Nº 1 (1979) -
Rio de Janeiro: Associação Brasileira de Ciências Mecânicas
Trimestral
Inclui referências bibliográficas.
1. Mecânica
ISSN-0100-7386

A REVISTA BRASILEIRA DE CIÊNCIAS MECÂNICAS publica trabalhos que cobrem os vários aspectos da ciência e da tecnologia em Engenharia Mecânica, incluindo interfaces com as Engenharias Civil, Elétrica, Química, Naval, Nuclear, Aeroespacial, Alimentos, Agrícola, Petróleo, Materiais, etc., bem como aplicações da Física e da Matemática à Mecânica.

Publicação da /Published by
ASSOCIAÇÃO BRASILEIRA DE CIÊNCIAS MECÂNICAS
THE BRAZILIAN SOCIETY OF MECHANICAL SCIENCES

Secretária da ABCM: Ana Lucia Fróes de Souza
Av. Rio Branco, 124-18º andar - Rio de Janeiro - Brasil
Tel. / Fax (021) 222-7128

Presidente: **Arthur Palmeira Ripper**
Vice-Presidente: **Sidney Stuckenbruk**
Secret. Geral: **Agamenon R. E. Oliveira**
Secretário: **Carlos Alberto de Almeida**
Diretor de Patrimônio: **Luiz Fernando Salgado Candiota**

EDITOR:
Leonardo Goldstein Jr.
UNICAMP - FEM - DETF - C.P. 6122
13083-970 Campinas - SP
Tel: (0192) 39-3006 Fax: (0192) 39-3722

EDITORES ASSOCIADOS:
Agenor de Toledo Fleury
IPT - Instituto de Pesquisas Tecnológicas
Divisão de Mecânica e Eletricidade - Agrupamento de Sistemas de Controle
Cidade Universitária - C.P. 7141
01064-970 São Paulo - SP
Tel: (011) 268-2211 R-504 Fax: (011) 869-3353

Carlos Alberto Carrasco Altemani
UNICAMP - FEM - DE - C.P. 6122
13083-970 Campinas - SP
Tel: (0192) 39-8435 Fax: (0192) 39-3722

José Augusto Ramos do Amaral
NUCLEN - NUCLEBRÁS ENGENHARIA. S.A.
Superintendência de Estruturas e Componentes Mecânicos.
R: Visconde de Ouro Preto, 5
22250-180 - Rio de Janeiro - RJ
Tel: (021) 552-2772 R-269 ou 552-1095 Fax: (021) 552-2993

Walter L. Weingaertner
Universidade Federal de Santa Catarina
Deptº de Engª Mecânica - Lab. Mecânica de Precisão
Campus - Trindade - C.P. 476
88049 Florianópolis - SC
Tel: (0482) 31-9395/34-5277 Fax: (0482) 34-1519

REVISTA FINANCIADA COM RECURSOS DO

Programa de Apoio a Publicações Científicas

MCT ***CNPq*** FINEP

FAPESP - Fundação de Amparo a Pesquisa do Estado de São Paulo

RBCM - J. of the Braz. Soc. Mechanical Sciences
Vol. XV - nº 1 - 1993 - pp. 1-20

ISSN 0100-7386
Printed in Brazil

Chaotic Vibrations of an Oscillator with Shape Memory

Vibrações Caóticas de um Oscilador com Memória de Forma

Marcelo A. Savi
Arthur M. B. Braga
Departamento de Engenharia Mecânica
Pontifícia Universidade Católica do Rio de Janeiro
22453 Rio de Janeiro, RJ - Brasil

Abstract

This article reports results from some investigation on the dynamical behavior of mechanical systems containing elements with shape memory. some phenomenological theories that describe shape memory and pseudoelastic effects in metallic alloys that undergo thermoelastic martensitic transformations are reviewed. One of these theories is used to model a helical spring. The dynamic response of an oscillator with a shape memory spring is investigated. It is shown that the system may behave chaotically under certain conditions.

Keywords: Chaotic Vibrations - Nonlinear Dynamics - Shape Memory

Resumo

Este trabalho apresenta resultados de um estudo sobre a resposta dinâmica de sistemas mecânicos contendo elementos com memória de forma. São discutidas algumas teorias fenomenológicas que descrevem os efeitos de memória de forma e pseudoelasticidade associados a transformações martensíticas termoelásticas em ligas metálicas. Uma destas teorias é utilizada na modelagem de uma mola helicoidal. O comportamento dinâmico de um oscilador com memória de forma é investigado. Verifica-se que o sistema pode responder caoticamente sob determinadas condições.

Palavras-chave: Vibrações Caóticas - Dinâmica Não-Linear - Memória de Forma

Introduction

Shape memory and stress-induced pseudoelasticity are effects observed in metallic alloys that undergo thermoelastic martensitic transformations (see, e.g., Buehler et al., 1963; Jackson et al., 1972; Delaey et al., 1974; Warlimont et al., 1974; Schetky, 1979). Qualitative plots in Fig. 1 illustrate both behaviors. The stress-strain curve in Fig. 1a is obtained at constant temperature, and shows the

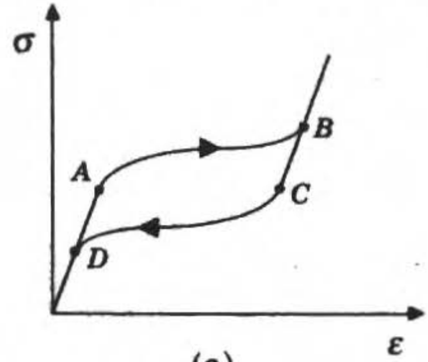

(a)

Fig. 1a. The pseudoelastic effect

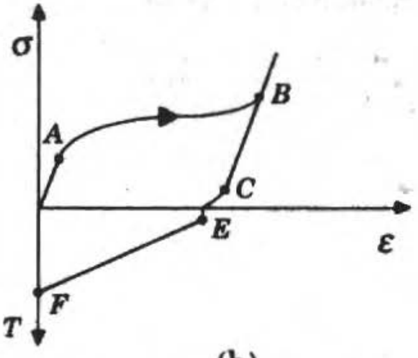

(b)

Fig 1b. The shape memory effect

Manuscript received December 1992. Associate Technical Editor: Agenor de Toledo Fleury

pseudoelastic strain recovery during a loading-unloading cycle. This behavior is typical at a temperature where the parent phase, austenite, is stable. At the point A in the diagram, the stress-induced transformation starts to cause the appearance of martensite. This process is completed at B, and the now all martensitic specimen deforms elastically again. During unloading, the transformation is reversed in the path CD, and the sample returns to its undeformed austenitic state.

The plot in Fig. 1b is obtained at a different temperature. The reverse transformation is not completed after the load is removed, and some permanent strain is still observed in the stress-free specimen. The shape memory effect consists in the recovery of this residual deformation by heating the sample to a temperature where the parent phase is stable. The temperature-induced reverse transformation occurs in the segment EF of the diagram.

The shape memory effect and other related thermoelastic processes associated with martensitic transformations have been known since at least 1938. But it has been the investigations of Buehler and co-workers (see, e.g., Buehler et al., 1963) on phase changes in NiTi alloys, in the early sixties, that instigated the technological interest in the shape memory effect. Experiments where NiTi objects were restored to their original shape after being "permanently" deformed, revealed the potential for the use of these alloys in engineering (Jackson et al., 1972; Schetky, 1979). Among other applications, one could mention self-actuating fasteners, self-erectable structures for aerospace hardware, thermally actuated switches, and a number of bioengineering devices. Most recently, shape memory alloys have also been employed as actuators for the active vibration control of flexible structures (Rogers, 1990; Rogers et al., 1991; Venkatesh et al., 1992).

The phenomena associated with martensitic transformations are intrinsically nonlinear. As a consequence, when subjected to dynamic inputs, a mechanical system which contains shape memory elements may experience a number of quite complex behaviors. One of them is chaos.

Chaotic response is characterized by long term unpredictability. A nonlinear system which is deterministic may experience completely irregular behavior even when excited periodically. This apparently random response has nevertheless a structure. The study of the structure underlying chaos has been a very active field in recent years. We refer to the books by Thompson and Stewart (1986) and Moon (1987) for lists of publications on the subject.

In this paper we are concerned with the chaotic response of mechanical system with shape memory. Firstly, we briefly review some of the available phenomenological theories that describe thermoelastic martensitic transformations in metallic alloys. One of these theories is used to build a model of an helical spring with shape memory. The dynamics of a simple, one degree-of-freedom oscillator is then investigated.

Phenomenological Theories for Shape Memory

Shape memory and other related effects associated with thermoelastic martensitic transformations may be modeled at either the microscopic or macroscopic levels. For descriptions at the microscopic level we refer to the articles by Achenbach and Müller (1982) and Warlimont et al. (1974). Here we are interested in phenomenological theories that describe the transformations macroscopically. These transformations are caused by changes in temperature as well as by mechanical actions. Hence, the macroscopic thermodynamical variables needed to describe the phenomena are temperature, T, and strain, ε. We consider small deformations only, in which case ε represents the infinitesimal strain tensor.

In order to account for the influence of phase transitions on the properties of shape memory alloys, there may also be a need for internal variables. The free energy, ψ, is then assumed to have the form

$$\psi = \psi(\varepsilon , T, \beta) \tag{1}$$

where β is a vector representing the internal variables.

If thermal dissipation is not considered, the Clausius-Duhem inequality may be written as (see, e.g., Germain, 1973)

$$\boldsymbol{\sigma} : \dot{\boldsymbol{\varepsilon}} - \rho\,(\dot{\psi} + s\dot{T}) \geq 0 \tag{2}$$

where ρ is the mass density, s the total entropy per unit of mass, and σ the Cauchy stress tensor.

From Eq. (1) one has

$$\dot{\psi} = \nabla_{\varepsilon}\,\psi : \dot{\varepsilon} + \nabla_{\beta}\,\psi \cdot \dot{\beta} + \frac{\partial\psi}{\partial T}\dot{T} \tag{3}$$

where $\nabla_{\varepsilon}\,\psi$ and $\nabla_{\beta}\,\psi$ represent the gradients of the free energy with respect to ε and β respectively. If we now define

$$\boldsymbol{\sigma} = \rho\nabla_{\varepsilon}\,\psi \tag{4}$$

$$B = -\rho\nabla_{\beta}\,\psi \tag{5}$$

and assume that (Germain, 1973)

$$\frac{\partial\psi}{\partial T} = -s \tag{6}$$

the inequality (2) may be rewritten as

$$(\boldsymbol{\sigma} - \bar{\boldsymbol{\sigma}}) : \dot{\varepsilon} + B \cdot \dot{\beta} \geq 0 \tag{7}$$

If dissipation is not considered, Eq. (7) becomes an equality, otherwise we introduce a pseudo-potential of dissipation, $\phi\,(\varepsilon, \beta)$, which is convex, positive, and vanishes at the origin. In this case, if we let

$$\boldsymbol{\sigma} = \bar{\sigma}\,(\varepsilon, \beta, T) + \nabla_{\dot{\varepsilon}}\,\phi\,(\dot{\varepsilon}\,, \dot{\beta}) \tag{8}$$

and

$$B = \nabla_{\dot{\beta}}\,\phi\,(\dot{\varepsilon}\,, \dot{\beta}) \tag{9}$$

the Clausius-Duhen inequality is automatically satisfied (Germain, 1973).

Mathematical models for shape memory are based on different choices for the functionals representing the free energy and the pseudo-potential of dissipation. We now briefly review some of these models.

Model with Polynomial Free-Energy

The first model discussed here is based on Devonshire theory for temperature-induced first order phase transition combined with hysteresis, and has been proposed by Falk (1982). This is an one-dimensional model which does not consider dissipation. In Devonshire theory, the free energy depends on the temperature and on the one-dimensional strain ε, i.e.

$$\psi = \psi\,(\varepsilon, T) \tag{10}$$

and no internal variable is considered.

The functional form of the free energy is chosen such that at high temperatures it has only one minimum at vanishing strain, representing the equilibrium of the parent phase. At low temperatures, martensite is stable, and the free energy must have minima at nonvanishing strains. At intermediate temperatures the free energy must have equilibrium points corresponding to both phases. These restrictions are satisfied by the polynomial expression

$$\rho\psi\,(\varepsilon, T) = \frac{1}{2}a\,(T - T_M)\,\varepsilon^2 - \frac{1}{4}b\varepsilon^4 + \frac{1}{6}e\varepsilon^6 \tag{11}$$

where a, b, and e are positive constants, while T_M is the temperature below which the parent phase becomes unstable. It is also convenient to define the temperature T_A, above which austenite is stable, and the free-energy has only one minimum at zero strain,

$$T_A = T_M + \frac{1}{4}\frac{b^2}{ae} \tag{12}$$

Using expression (12) to eliminate e, and recalling that without dissipation the stress is simply the derivative of the free energy with respect to strain, we obtain the constitutive law based on Devonshire theory:

$$\sigma = a(T - T_M)\varepsilon - b\varepsilon^3 + \frac{1}{4}\frac{b^2}{a(T_A - T_M)}\varepsilon^5 \tag{13}$$

Stress-strain curves based on the polynomial model are shown in Fig. 2, where the thick lines represent stable loading-unloading paths. The shape memory effect is illustrated in Fig. 2a and 2b, obtained for temperatures below T_A. The curve in Fig. 2c is representative of higher temperatures, and shows the pseudoelastic phenomenon described by the polynomial model.

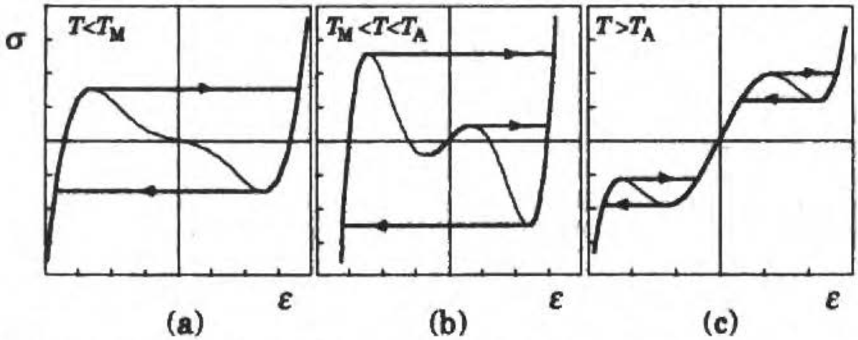

Fig. 2 Stress-Strain curves based on the polynomial model. Thick lines represent stable loading paths.

Model with Assumed Transformation Kinetics

Another theory that models the one-dimensional mechanics of martensitic phase transformations has been developed by Tanaka and co-workers (Tanaka and Nagaki, 1982; Tanaka, 1985; Sato et al., 1985; Tobushi and Tanaka, 1990). In addition to uniaxial strain and temperature, Tanaka's theory also considers a scalar internal variable that characterizes the extent of transformation. This variable, β_1, represents the volumetric fraction of martensite. The free energy has the form

$$\psi = \psi(\varepsilon, \beta_1, T) \tag{14}$$

The constitutive equation may be written in rate form as

$$\dot{\sigma} = E\dot{\varepsilon} - \alpha\dot{\beta}_1 - \Xi\dot{T} \tag{15}$$

where

$$E = \rho\frac{\partial^2\psi}{\partial\varepsilon^2}, \quad \alpha = \rho\frac{\partial^2\psi}{\partial\varepsilon\partial\beta_1}, \quad \text{and } \Xi = \rho\frac{\partial^2\psi}{\partial\varepsilon\partial T} \tag{16}$$

In Eq. (15), E is the elastic modulus and Ξ a thermoelastic coefficient, while α is associated with volume changes in the transformation (Sato et al., 1985). In general, these coefficients depend on the state variables ε, T, and β_1, but in the articles by Tanaka (1985), Sato et al. (1985), and Tobushi and Tanaka (1990), they are assumed to be constant and positive.

The other assumption in Tanaka's theory, is that the fraction of martensite is determined only through the current values of stress and temperature (Sato et al., 1985), i.e.

$$\beta_1 = B(\sigma, T) \tag{17}$$

The hypothesis is based on the difusionless nature of martensitic transformations (Tanaka, 1985). Sato et al. (1985) assume an exponential form for the functional on the right-hand-side of (17). The transformation from austenite to martensite is then described by

$$\beta_1 = 1 - \exp\left[-a_M (T_M - T) - b_M \sigma\right] \tag{18}$$

where T_M is the temperature where martensite starts to form under stress-free state, while a_M and b_M are positive constants (Sato et al., 1985). Eq. (18) holds for

$$\sigma \geq \left(\frac{a_M}{b_M}\right)(T - T_M) \tag{19}$$

The reverse transformation is described by another exponential function (Sato et al., 1985)

$$\beta_1 = \exp\left[-a_A (T - T_A) + b_A \sigma\right] \tag{20}$$

where a_A and b_A are positive constants while T_A is the temperature where austenite starts to form under zero stress. The kinetics of the reverse transformation (20) holds for

$$\sigma \leq \left(\frac{a_A}{b_A}\right)(T - T_A) \tag{21}$$

The dependency of martensite fraction on temperature under stress-free state, is schematically shown in Fig. 3a. The plot in Fig. 3b illustrates the kinetics of the stress induced transformation under constant temperature.

Tanaka's theory is capable of modeling the pseudoelastic behavior as well as the shape memory effect, and has been used in a number of applications (Sato et al., 1985; Tobushi and Tanaka, 1990). Rogers et al. (1991) and Liang and Rogers (1990) have employed a modification of this theory to develop a mathematical model for shape memory alloy hybrid composites used in structural acoustics control. In their model, instead of the exponential law presented above, the kinetics of transformation is described by a cosine function (Liang and Rogers, 1990). Results of Roger's model are in close agreement with experimental data (Rogers et al., 1989; Rogers, 1990).

It should be pointed out, however, that Tanaka's model, at least in the form presented above or in the references cited here, does only apply to tensile behavior. This is not explicitly stated by Sato et al. (1985). Furthermore, the stress-strain plot in compression presented in that article, Fig. 5 in (Sato et al., 1985), can not be obtained by applying only the set of equations introduced by its authors and repeated above. We believe that in order to correctly describe the shape memory alloy response under compressive loads, one has to introduce another internal variable, β_2, representing the volumetric fraction of a second variant of martensite. Of course, the following restriction must then be satisfied:

$$\beta_1 + \beta_2 \leq 1 \tag{22}$$

It is well known that shape memory alloys usually develop various kinds of martensite (Jackson et al., 1972; Delaey et al., 1974; Warlimont et al., 1974), and that in the same alloy, each variant grows favorably under one type of stress state (Schetky, 1979). Here, the second variant, β_2, should grow at the expense of β_1 under compressive loads and vice-versa. This and restriction (22), have to be taken into account in the assumptions concerning the transformation kinetics of the martensite variants.

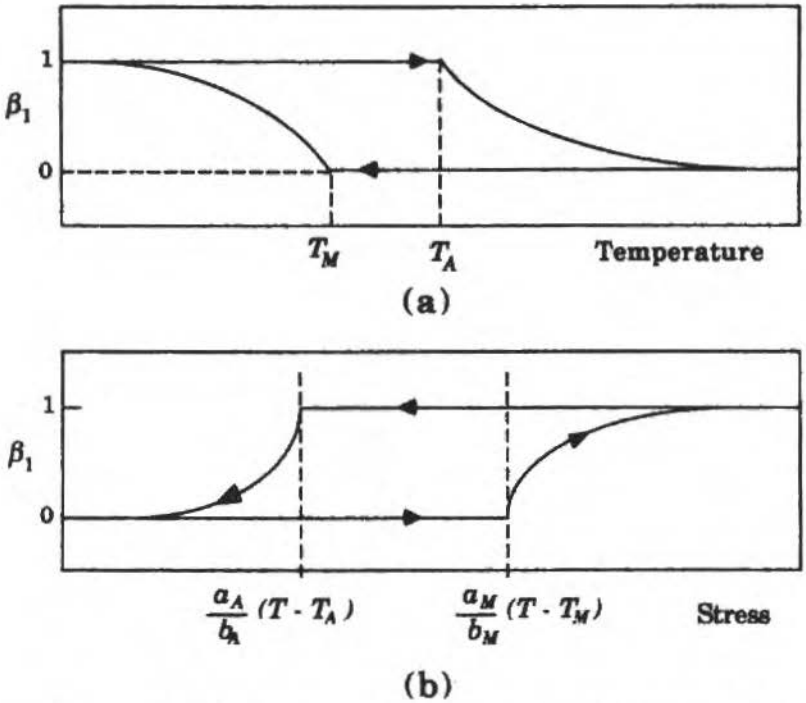

Fig. 3 Variation of martensite fraction with temperature at the stress-free state (a), and with stress under constant temperature (b).

Model with Internal Restrictions

The third type of phenomenological theory considered here has been developed by Fremond (1987). The shape memory and pseudoelastic effects are described with the aid of three internal variables, β_1, β_2, and β_3, respectively representing the volumetric fractions of two variants of martensite and of the austenitic parent phase. In this three-dimensional model, the three different phases may coexist, and the internal variables have to satisfy the following constraints:

$$0 \leq \beta_i \leq 1 \, (i = 1, 2, 3) \text{ and } \beta_1 + \beta_2 + \beta_3 = 1 \tag{23}$$

The free-energy of the mixture is then defined as

$$\rho\psi(\varepsilon, \beta_i, T) = \rho \sum_{i=1}^{3} \beta_i \psi_i(\varepsilon, T) + \bar{I}(\beta_i \tag{24}$$

where $\psi_i(\varepsilon, T)$ is the free-energy of the individual phases and $\bar{I}(\beta_i)$ is the indicator function (Rockafellar, 1970) of the convex set

$$C = \{ (\beta_1, \beta_2, \beta_3) \,|\, 0 \leq \beta_i \leq 1;\ \beta_1 + \beta_2 + \beta_3 = 1 \} \tag{25}$$

and defined as

$$\bar{I}(\beta_i) = 0 \quad \text{if } \beta_i \in C$$

$$\bar{I}(\beta_i) \rightarrow \infty \quad \text{if } \beta_i \notin C \tag{26}$$

The functions describing the free-energy of the individual phases are chosen as

$$
\begin{aligned}
\rho\psi_1(\varepsilon, T) &= \frac{1}{2}\varepsilon : \quad C : \varepsilon - \alpha(T)\,\mathrm{tr}(\varepsilon) \\
\rho\psi_2(\varepsilon, T) &= \frac{1}{2}\varepsilon : \quad C : \varepsilon + \alpha(T)\,\mathrm{tr}(\varepsilon) \\
\rho\psi_3(\varepsilon, T) &= \frac{1}{2}\varepsilon : \quad C : \varepsilon - \frac{L}{T_M}(T-T_M)
\end{aligned}
\tag{27}
$$

where **C** is the elasticity tensor, $\alpha(T)$ is proportional to the coefficient of thermal expansion, and L is the latent heat of the martensite-austenite phase change. Observe that all phases are assumed to have the same mass density and elastic properties. Also notice that since this is a three-dimensinal theory, in the previous equations ε represents the tensor of infinitesimal strains.

Using the second of equations (23), one can eliminate β_3 from the expression for the free-energy of the mixture, obtaining

$$
\begin{aligned}
\rho\psi(\varepsilon, \beta_1, \beta_2, T) &= \rho\,\{\beta_1[\psi_1(\varepsilon, T) - \psi_3(\varepsilon, T)] \\
&+ \beta_2[\psi_2(\varepsilon, T) - \psi_3(\varepsilon, T)] + \psi_3(\varepsilon, T)\} + \bar{J}(\beta_1, \beta_2)
\end{aligned}
\tag{28}
$$

where $\bar{J}(\beta_1, \beta_2)$ is the indicator function of the triangle defined in the $\beta_1\beta_2$-plane as

$$\tau = \{(\beta_1, \beta_2) \,|\, 0 \le \beta_i \le 1;\ \beta_1 + \beta_2 \le 1\} \tag{29}$$

Now, from equations (4) and (5), considering that the pseudo-potential of dissipation does not depend on the strain rate, i.e., $\phi = \phi(\dot{\beta}_1, \dot{\beta}_2)$, one obtains

$$\sigma = C : \varepsilon + (\beta_2 - \beta_1)\,\alpha(T)\,I \tag{30}$$

and

$$
\begin{aligned}
\frac{\partial\phi}{\partial\dot{\beta}_1} &= \alpha(T)\,\mathrm{tr}(\varepsilon) - \frac{L}{T_M}(T - T_M) - \partial_1\bar{J} \\
\frac{\partial\phi}{\partial\dot{\beta}_2} &= -\alpha(T)\,\mathrm{tr}(\varepsilon) - \frac{L}{T_M}(T - T_M) - \partial_2\bar{J}
\end{aligned}
\tag{31}
$$

where I is the identity tensor, while $\partial_1\bar{J}$ (resp. $\partial_2\bar{J}$) represents the subdifferential (Rockafellar, 1970) of the indicator function $\bar{J}(\beta_1, \beta_2)$ with respect to β_1 (resp. β_2).

The concepts of indicator function and subdifferential, are employed by Fremond in order to guarantee that β_1 and β_2 will be, at all time, inside or on the surface of the triangular region defined by equation (29). The use of Lagrange multipliers offers an alternative approach, which is also more suitable for numerical calculations based on this theory. The constraints to be satisfied are

$$-\beta_1 \le 0,\ -\beta_2 \le 0,\ \text{and}\ \beta_1 + \beta_2 - 1 \le 0 \tag{32}$$

The indicator function may be written in the form

$$\bar{J} = -\lambda_1\beta_1 - \lambda_2\beta_2 + \lambda_3(\beta_1 + \beta_2 - 1) \tag{33}$$

from what follows

$$\frac{\partial\phi}{\partial\dot{\beta}_1} = \alpha(T)\,\mathrm{tr}(\varepsilon) - \frac{L}{T_M}(T - T_M) + \lambda_1 - \lambda_3$$

$$\frac{\partial\phi}{\partial\dot{\beta}_2} = -\alpha(T)\,\mathrm{tr}(\varepsilon) - \frac{L}{T_M}(T - T_M) + \lambda_2 - \lambda_3 \tag{34}$$

where λ_1, λ_2, and λ_3 are the Lagrange multipliers.

We also have to introduce a set of Kuhn-Tucker conditions (Luenberger, 1973):

$$\beta_1\lambda_1 = 0,\ \ \beta_2\lambda_2 = 0,\ \text{ and }\ (\beta_1 + \beta_2 - 1)\,\lambda_3 = 0 \tag{35}$$

and

$$\lambda_1 \geq 0,\ \ \lambda_2 \geq 0,\ \text{ and }\ \lambda_3 \geq 0 \tag{36}$$

Equations (30), (32), and (34-36), form the mathematical structure of the model with internal restrictions introduced by Fremond. An algorithm for the solution of this set of equations has been proposed by the authors (Savi and Braga, 1993).

It is worthwhile to compare Fremond's theory with that developed by Tanaka and presented elsewhere in this paper. In order to do so, we reduce Fremond's model to one-dimension, replacing the tensor $\boldsymbol{\varepsilon}$ and its trace by the uniaxial strain ε. Also, we use the component σ instead of the stress tensor $\boldsymbol{\sigma}$, while the elasticity tensor **C** is replaced by the modulus E.

The most striking difference between the two models is that, while the theory developed by Fremond uses two kinds of martensite, Tanaka's considers only one. The first martensite in Fremond's model, β_1, is active only when the stress is positive (Fremond, 1987). Thus, keeping the comparison within tensile behavior at constant temperature, we observe that the constitutive equations (15) and (30) become very similar. In fact, the material parameter α has the same meaning in both models. Another point of contrast between these two theories, is the number of characteristic temperatures considered. Fremond assumes that both the martensitic and reverse transformations begin at $T=T_M$. Tanaka considers two different temperatures, T_M and T_A. The latter is associated with the start of the reverse transformation (martensite → austenite).

Despite these differences, it may be shown that both models predict identical response for successive tensile loading and unloading if we make the following assumptions: 1) the coefficients a_M, b_M, a_A, and b_A, become very large, approaching infinity in such a way that $a_A/b_A = a_M/b_M \rightarrow EL/\alpha T_M$; and 2) $T_A/T_M = 1 + (\alpha^2/EL)$. The first assumption means that the transformation occurs instantaneously when the stress reaches the transformation line. The second is made in order to adjust the stress threshold for the reverse transformation. Plots showing the loading unloading paths predicted by both theories under these assumptions are presented in Fig. 4.

Finally, a few comments on the shortcomings of Fremond's three-dimensional model are in order. Firstly, it should be pointed out that, since the difference between the volumetric fractions of martensite variants appears multiplied by the identity tensor in Eq. (30), the model can not describe thermoelastic martensitic transformations induced by pure shear stress states. Results of torsion tests presented by Jackson et al. (1972) indicate, however, that these transformations do occur in nickel-titanium alloys.

A second remark, concerns the form assumed by Fremond's three-dimensional model when the stress-state is one-dimensional. In this case, if all three phases are assumed to behave isotropically, the trace of the strain tensor will also include a term proportional to the difference $(\beta_2 - \beta_1)$. A more detailed analysis, out of the scope of the present contribution, will show that the resulting equations predict qualitatively different uniaxial stress-strain curves from those obtained experimentally, or by the other two one-dimensional models discussed in this article. This apparent shortcoming may be easily overcome by including another term in the expression of the free-energy.

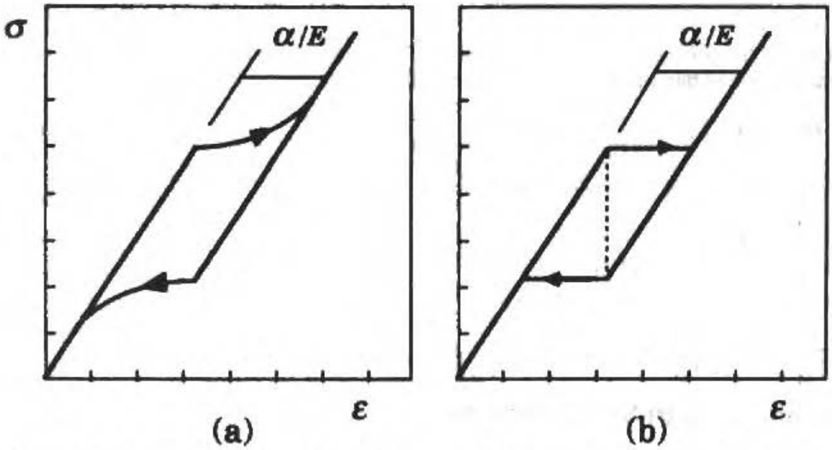

Fig. 4 Stress-strain curves at $T > T_A$: (a) predicted by Tanaka's model with exponential law; (b) obtained from both theories when assuming $a_A/b_A = a_M/b_M \rightarrow EL/\alpha T_M$ and $T_A/T_M = 1 + (\alpha^2/EL)$

An Helical Spring with Shape Memory

In order to model the response of an helical spring made from a shape memory alloy, one could apply any of the constitutive theories discussed in the preceding section. In fact, all three provide fairly good qualitative description of the one-dimensional shape memory and pseudoelastic effects. Here, we have chosen the polynomial free-energy function of Devonshire's theory. This choice yields the simplest equation for the nonlinear restoring force.

We assume that the longitudinal external force is resisted by the torsional shear stresses developed on the circular cross section of the helical shaped wire (Shigley, 1972; Tobushi and Sato, 1990). The relationship between the longitudinal force, F, and the shear stress distribution, σ, is expressed as

$$F = \frac{4\pi}{D} \int_0^{d/2} \sigma r^2 dr \tag{37}$$

where r is the radial coordinate along the cross-section, while D and d represent, respectively, the diameters of the spring and of the wire cross-section (Fig. 5).

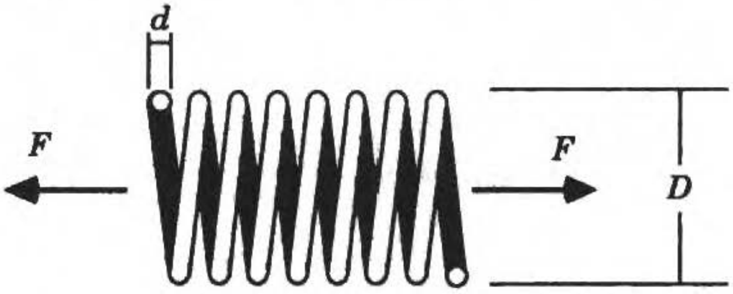

Fig. 5 Helical spring

We also assume that the shear strain, ε, is distributed linearly along the wire cross-section. If N is the number of coils and X the deflection, it can be shown (Shigley, 1972) that

$$\varepsilon = \frac{2r}{\pi D^2 N} X \tag{38}$$

Now, using the polynomial model, and assuming that Eq. (13) is valid for the pure shear stress-strain behavior, we obtain the following nondimensional equation for the nonlinear restoring force:

$$f = (\theta - 1)\, x - \lambda x^3 + \frac{\lambda^2}{4(\theta_C - 1)} x^5 \tag{39}$$

where f and x are the nondimensional force and displacement:

$$f = \frac{8D}{\pi a T_M d^3} F, \quad x = \frac{d}{\pi D^2 N} X \tag{40}$$

while the other parameters are defined as

$$\theta = \frac{T}{T_M}, \ \lambda = \frac{2b}{3aT_M}, \ \text{and} \ \theta_C = \frac{1}{9}\left(8\frac{T_A}{T_M} + 1\right) \tag{41}$$

The Oscillator with Shape Memory

We consider the one degree-of-freedom oscillator shown in Fig. 6. It consists of a mass m supported by a shape memory spring and a linear damper with coefficient c. The system is excited harmonically by the force Psinωt. The nonlinear equation governing the forced motions of the oscillator may be written in the nondimensional form

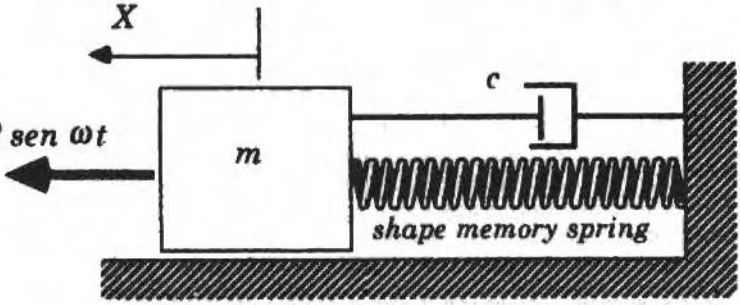

Fig 6. Oscillator with shape memory

$$\ddot{x} + \xi \dot{x} + (\theta - 1)\, x - \lambda x^3 + \frac{\lambda^2}{4(\theta_C - 1)} x^5 = \gamma \sin \Omega\tau \tag{42}$$

The dots represent derivatives with respect to the nondimensional time, τ, defined as

$$\tau = \omega_0 t, \ \text{where} \ \omega_0 = \sqrt{a T_M d^4 / 8 m D^3 N} \tag{43}$$

The other constants appearing in Eq. (42) are

$$\xi = c/m\omega_0, \ \gamma = \frac{8D}{\pi a T_M d^3} P, \ \text{and} \ \Omega = \omega/\omega_0 \tag{44}$$

If we define

$$y_1 = x \ \text{and} \ y_2 = \dot{x} \tag{45}$$

Eq. (42) can be written as a first-order system:

$$\begin{aligned} \dot{y}_1 &= y_2 \\ \dot{y}_2 &= -\xi y_2 - (\theta - 1)\, y_1 + \lambda y_1^3 - \frac{\lambda^2}{4(\theta_C - 1)} y_1^5 + \gamma \sin \Omega\tau \end{aligned} \tag{46}$$

Free Vibrations

Free vibrations of the shape memory oscillator are described by the autonomous system obtained by letting γ vanish in Eqs. (46). In this section, we discuss the system response when it is displaced from an equilibrium configuration.

The fixed points, or equilibrium configurations, depend on the temperature. Denoting by $(\bar{y}_1, \bar{y}_2)$ a point in the y_1y_2-plane (the phase space) that, for $\gamma=0$, make the right-hand sides of Eqs. (46) vanish, we find five possibilities:

$$\bar{y}_1 = 0 \text{ and } \bar{y}_2 = 0 \tag{47}$$

or

$$\bar{y}_1 = \pm\left(\frac{2(\theta_C-1)}{\lambda}\left(1 \pm \left(\frac{\theta_C-\theta}{\theta_C-1}\right)^{1/2}\right)\right)^{1/2} \text{ and } \bar{y}_2 = 0 \tag{48}$$

Of these five possibilities, only those which correspond to real numbers have physical meaning. Hence,

a) for $\theta \le 1$, the system has three fixed points;

b) for $1 < \theta < \theta_C$, the system has five fixed points;

c) for $\theta = \theta_C$, the system has three fixed points;

d) for $\theta > \theta_C$, the system has only one fixed point.

Stability of these equilibrium configurations are determined by the behavior of the linearized system in their neighborhood. By making the change of variables

$$\eta_j = y_j - \bar{y}_j \quad (j = 1, 2) \tag{49}$$

and considering η_j small, the autonomous ($\gamma=0$) linearized system assumes the form

$$\begin{aligned} \dot{\eta}_1 &= \eta_2 \\ \dot{\eta}_2 &= -\left((\theta-1) - 3\lambda\bar{y}_1^2 + \frac{5\lambda^2}{4(\theta_C-1)}\bar{y}_1^4\right)\eta_1 - \xi\eta_2 \end{aligned} \tag{50}$$

An analysis of the eigenvalues of this system reveals that, for $\theta \le 1$, the origin of the phase space, which corresponds to a state of rest, is a saddle point. The other two fixed points are centers when $\xi=0$ (undamped system) or stable spirals when $\xi > 0$. This is consistent with the low temperature behavior of the shape memory alloy, where two martensitic phases are stable.

When $1 < \theta < \theta_C$, the system has two saddle points in the phase space. These are

$$\bar{y}_1 = \pm\left(\frac{2(\theta_C-1)}{\lambda}\left(1 - \left(\frac{\theta_C-\theta}{\theta_C-1}\right)^{1/2}\right)\right)^{1/2} \text{ and } \bar{y}_2 = 0 \tag{51}$$

The remaining three fixed points are centers if the system has no dissipation. They are stable spirals otherwise. The existence of three stable fixed points is explained by the stability of both martensitic phases and the parent austenite in this temperature range.

When $\theta=\theta_C$, the origin is a center if $\xi=0$, or a stable spiral if the system is dissipative. The other two fixed points are saddles. Finally, for $\theta > \theta_C$, the origin, which now is the only stable fixed point in the phase plane, is either a center or a spiral, again depending whether the system is dissipative or not. For $\theta > \theta_C$, austenite is the only stable phase in the stress-free shape memory alloy.

Fig. 7 shows some phase plane trajectories illustrating the free vibration of the undamped shape memory oscillator at three different temperatures. These results have been obtained by numerical integration of Eqs. (46). The standard fourth-order Runge-Kutta algorithm has been used in these calculations. We have obtained good convergence with a step size $\Delta\tau=2\pi/180$. Since we are, at this

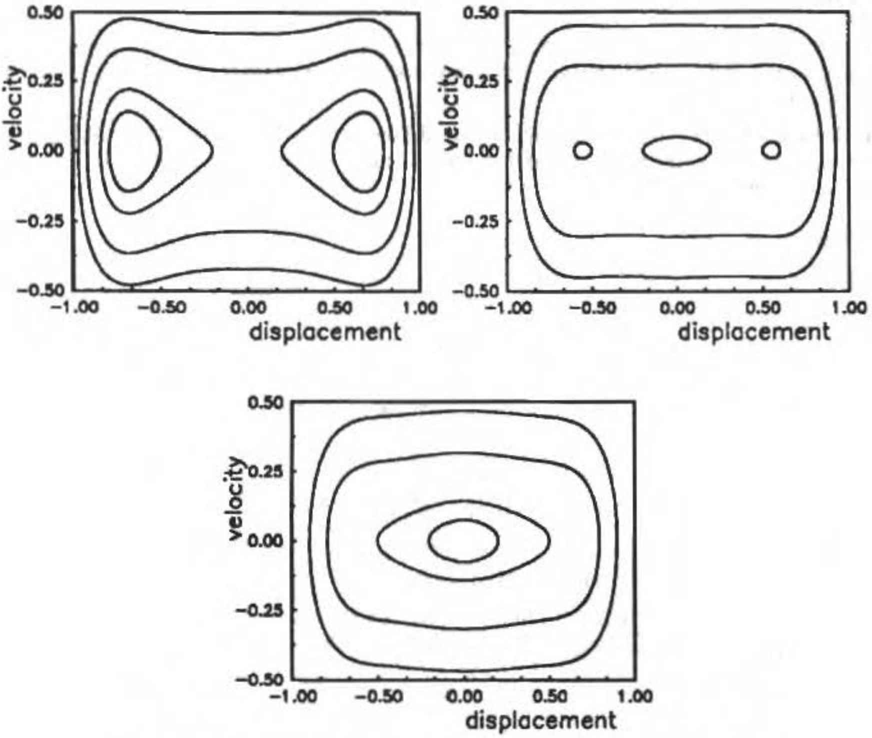

Fig. 7 Phase portraits of the unforced non dissipative system ($\xi = 0$).
(a) $\Theta < 1$; (b) $1 < \Theta < \Theta_c$; (c) $\Theta < \Theta_c$

point, more concerned with the qualitative response of the shape memory system, we have chosen $\lambda=1$ for the example calculations presented throughout this article. We have also assumed $\theta_C=1.10$, which is a typical value for nickel-titanium alloys (Tobushi and Tanaka, 1990).

Results showing the phase plane trajectories for the dissipative system ($\xi=0.2$) at constant temperature are presented in Fig. 8. We observe that when the system has more than one dynamical attractor, which is the case when $\theta < \theta_C$ (Figs. 8a and 8b), its final configuration is very sensitive to the initial condition. This is a common feature of nonlinear systems.

Fig. 9 shows the behavior of the autonomous system subjected to a temperature variation. This result has been obtained by assuming that the temperature of the system, initially θ_i, changes to θ_f in the following way:

$$\theta = \begin{cases} \theta_i & \text{if} \quad \tau \le \tau_i; \\ \theta_i + (\theta_f - \theta_i) \sin \dfrac{\pi(\tau - \tau_i)}{2(\tau_f - \tau_i)} & \text{if } \tau_i < \tau < \tau_f; \\ \theta_f & \text{if} \quad \tau \ge \tau_f; \end{cases} \tag{52}$$

The mass is displaced from its equilibrium position at the instant $\tau=0$. After an interval of time, τ_i, the temperature begins to change, up to the instant τ_f, when it reaches the final temperature level. In Fig. 9a, we have considered the undamped oscillator. The plot in Fig. 9b has been obtained for the dissipative system. The dashed line represents the transient behavior between τ_i and τ_f. As expected, the oscillator settles on a different attractor after the new temperature level is reached. This behavior is

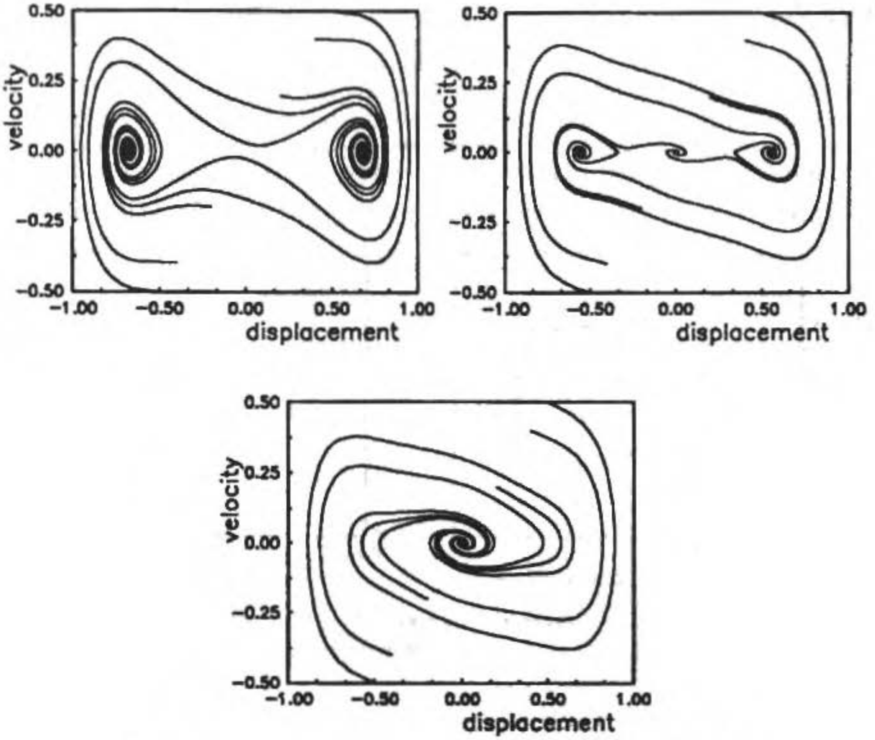

Fig. 8 Phase portraits of the unforced dissipative system ($\xi = 0.2$).
(a) $\Theta < 1$; (b) $1 < \Theta < \Theta_c$; (c) $\Theta < \Theta_c$

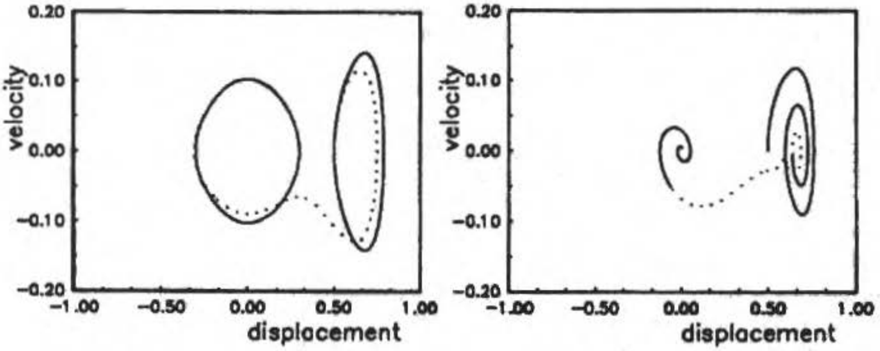

Fig. 9 Unforced system subjected to a temperature variation. $\theta_i = 0.95$; $\theta_f = 1.16$
(a) Non dissipative system ($\xi = 0$). (b) Dissipative system ($\xi = 0.2$).

of special interest, since it illustrates the capability of altering the dynamics of the shape memory system by changing its temperature. We shall return to this point when discussing the forced response of the oscillator.

Chaotic Vibrations of the Shape Memory Oscillator

The behavior of the forced system is far more complex. In this section, we discuss the response of the shape memory oscillator to periodic excitations. In particular, we are concerned with the prospect of chaotic behavior. The system is governed by Eqs. (46), where γ and Ω are the nondimensional parameters representing, respectively, the amplitude and frequency of the sinusoidal forcing function. For the numerical examples presented in this section, we have taken $\Omega=1$ and let γ vary.

Initially, we observe the response when the forcing amplitude is small. Fig. 10 shows results of the numerical integration when $\xi=0$, $\theta=0.95$ and $\gamma=10^{-3}$. Along with the phase plane trajectory in Fig. 10a, we also show a Poincaré section of the orbit, which is obtained by sampling the state variables, displacement and velocity of the oscillator, at a rate equal to the forcing period. This procedure may be better understood if we view the forced oscillator as an autonomous system with a three-dimensional phase space. Time, in fact the quantity $\Omega\tau$, is taken here as the third explicit state variable. Also, since the forcing is periodic, one considers the state space as the Cartesian product of the Euclidian 2-space, the plane, with the circle (see, e.g., Guckenheimer and Holmes, 1983, pp. 25-27). The set of points on the Poincaré section are then the intersections of the orbit with a plane that cuts this cylindrical state space at $\Omega\tau=\varphi$, where φ is a constant between 0 and 2π. Discussions on this geometrical view of dynamical systems may be found, for instance, in (Abraham and Shaw, 1982; Wiggins, 1988; Wiggins, 1990).

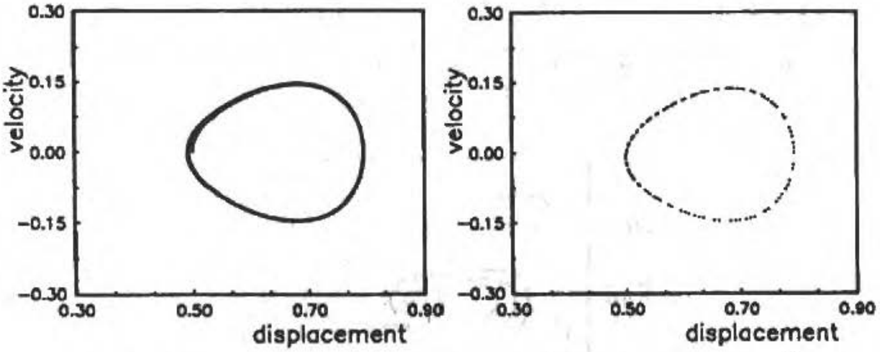

Fig. 10 Quasi-periodic response of the system. $\xi = 0;\ \theta = 0.95;\ \gamma = 10^{-3}$
(a) Phase plane trajectory; (b) Poincaré section of the orbit

The phase plane trajectory shown in Fig. 10a, indicates that the system oscillates around one of the equilibrium configurations associated with this temperature and initial conditions. The Poincaré section in Fig. 10b, reveals that the motion is in fact quasi-periodic. A periodic orbit is shown in Fig. 11. Now, we have taken $\theta=0.95$, $\xi=0.2$, and $\gamma=0.05$. In this case, the Poincaré section is simply a point in the phase plane.

As the forcing parameter γ increases, the system dynamics becomes reacher. Fig. 12 shows the time history of the oscillation amplitude when $\theta=0.95$ and $\gamma=5$. The plot in Fig. 12a has been obtained for $\xi=0$, while in Fig. 12b we have taken $\xi=0.1$. In both cases, the system response shows no visible periodicity. The Poincaré section for the undamped system, displayed in Fig. 13a, now consists of a cloud of points that fills the phase plane with no noticeable structure. This lack of structure is common in nondissipative chaos.

Although the time history of the dissipative system is very similar to that of the undamped oscillator (Figs. 12a and 12b), its Poincaré section, shown in Fig. 13b, appears as a set of points arranged in a highly organized fashion. Poincaré sections illustrating the forced response of the damped oscillator at different temperatures are shown in Fig. 14. All plots show the same fractal-like structure. In fact, such structured collections of points correspond to Cantor Sets (see, e.g., Guckeinheimer and Holmes, 1983; Thompson and Stewart, 1986; Moon, 1987; Wiggins, 1988;

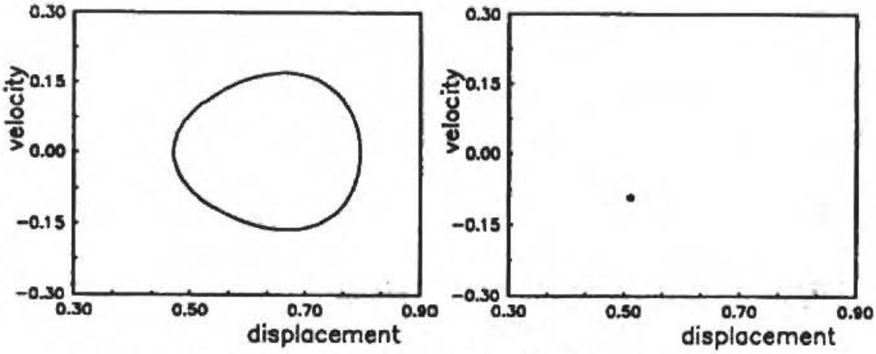

Fig. 11 Periodic response of the system. $\xi = 0.2$; $\theta = 0.95$; $\gamma = 0.05$
(a) Phase plane trajectory; (b) Poincaré section of the orbit

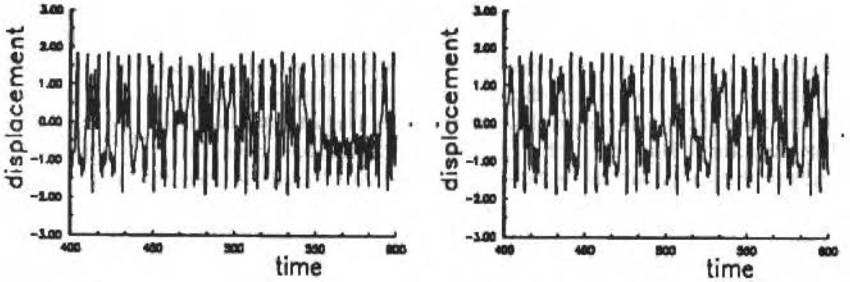

Fig. 12 Time history of a chaotic response. $\xi = 0$; $\theta = 0.69$; $\gamma = 5$
(a) Non dissipative system ($\xi = 0$); (b) Dissipative system ($\xi = 0.1$)

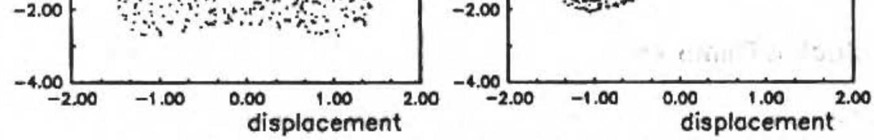

Fig. 13 Poincaré section of a chaotic response. $\theta = 0.69$; $\gamma = 5$
(a) Non dissipative system ($\xi = 0$); (b) Dissipative system ($\xi = 0.1$)

Wiggins, 1990), and are indication of the folding and stretching experienced by the chaotic orbits of the forced, damped oscillator. These collections of points are called strange attractors (Moon, 1987), and are usually found in dissipative chaos.

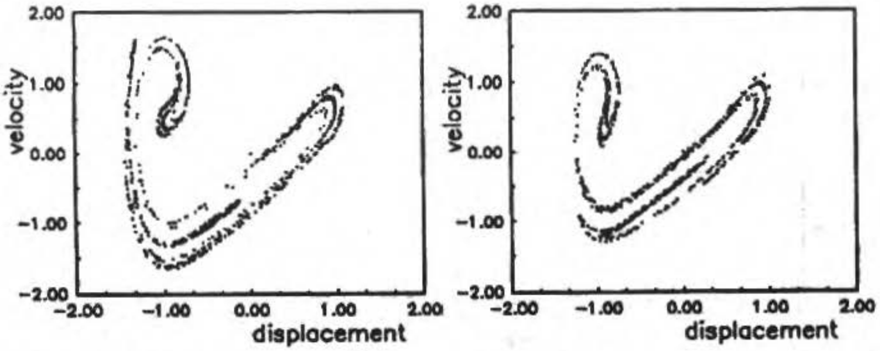

Fig. 14 Poincaré section of a chaotic response in a dissipative system ($\xi = 0.2$) at different temperatures. (a) $1 < \theta < \theta_c$; $\gamma = 5$; (b) $\theta > \theta_c$; $\gamma = 4.5$

The fractal set on the Poincaré section is in fact a cross section of the three-dimensional attracting structure embedded in the cylindrical phase space. It is interesting to observe the evolution of orbits initiated at a circle of states (initial displacement and velocity) on the phase plane. After successive time intervals, we check the intersections of this set of orbits with the phase plane. This is shown in Fig. 15. If the attracting orbit is periodic, the circle of initial states is mapped to a point (Fig. 15a). When the response is chaotic, the original circle is continuously stretched and folded approaching a fractal-like structure (Fig. 15b). This picture, which is a common feature of chaotic motions, corresponds to the so-called Smale horse-shoe (Wiggins, 1988). Another view of the attracting structure is presented in Fig. 16, that shows Poincaré sections taken at different values of $\Omega\tau$.

A bifurcation diagram is presented in Fig. 17, demonstrating the influence of the driving amplitude on the system dynamics. It is interesting to notice the presence of periodic windows, and the occurrence of a cascade of period doubling bifurcations leading to chaos in one of these windows (enlarged region in the upper right corner of the figure). The pattern in Fig. 17 is typical of a number of nonlinear dynamical system that exhibit chaotic behavior (Grebogi et al., 1983).

Finally, Fig. 18 shows a transition from chaotic to periodic response due to a variation in the system temperature. This plot, again illustrates the capability of altering the dynamics of the shape memory oscillator with the temperature. This feature has motivated the use of shape memory alloys as actuators for active vibration control of structures responding in the linear range (Rogers, 1990; Rogers et al., 1991; Venkatesh et al., 1992). It should be pointed out, however, that in these applications the actuators have been employed under conditions where the SMA stress-strain behavior could be linearized.

Concluding Remarks

In this paper, we have focused on the qualitative behavior of a simple dynamical system with shape memory. Three different theories that model the phase transformations associated with pseudoelasticity and the shape memory effect have been reviewed. All three theories provide satisfactory qualitative one-dimensional description of these effects. Only one of these models, however, can be applied to three-dimensional stress states.

The constitutive theory that assumes a polynomial expression for the free-energy functional has been used to model an helical spring with shape memory. This choice yields the simplest analytical form for the nonlinear restoring force. The dynamics of an one degree-of-freedom oscillator containing such a spring has been studied numerically.

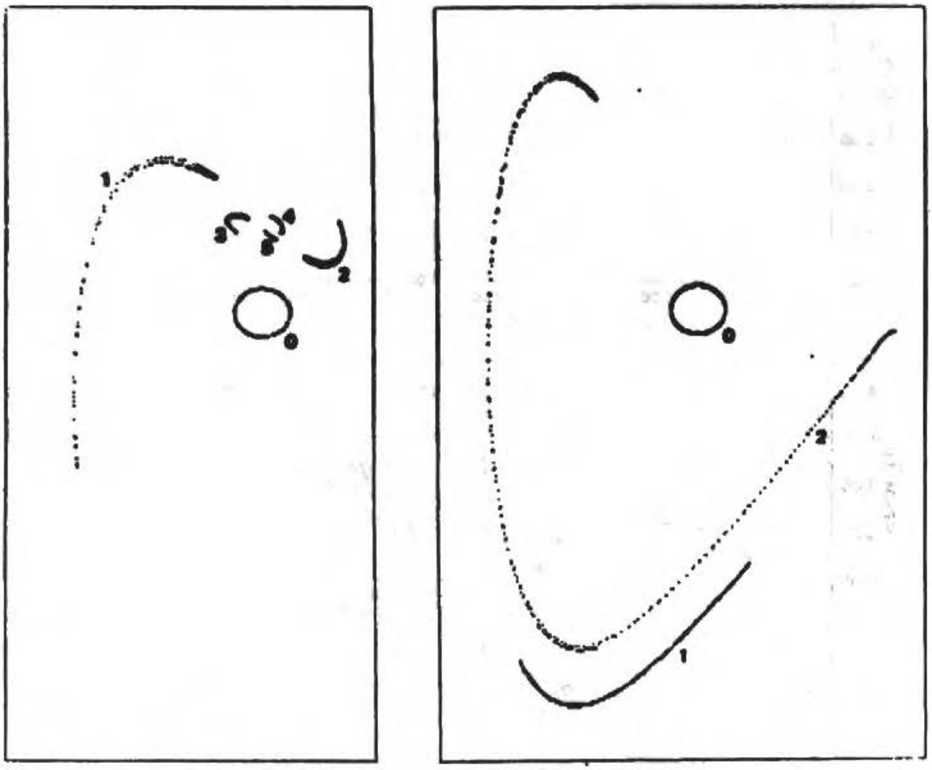

Fig. 15 Evolution of a ball of initial conditions in the phase space (a) Periodic motion; (b) Chaotic motion

Results of the numerical simulations indicate that this mechanical oscillator may exhibit chaotic response under certain conditions. Despite the limitations of the analytical model used here, and the lack of experimental data, the authors believe that similar behavior may be expected in other systems with shape memory. This conclusion suggests that the possibility of chaotic response should be considered when designing shape memory actuators for vibration and structural acoustic control.

Acknowledgements

The authors would like to thank Prof. H. Costa Mattos fo his insightful comments on the constitutive modeling of shape memory. During the course of this work, M. A. Savi has been supported by a grant from CNPq. Support from the Brazilian Ministry of Science and Technology to PUC-Rio is also gratefully acknowledged.

References

Abraham, R. H. and Shaw, C. D., 1982, Dynamics - The Geometry of Behavior, Parts 1-3, Aerial Press, Santa Cruz, California.

Achenbach, M. and Müller, I., 1982, "A Model for Shape Memory", J. de Physique, Colloque C4, Suppl. 12, Tome 43, pp. 163-167.

Buekler, W. J., Gilfrich, J. V. and Wiley, R. C., 1963, "Effect of Low-Temperature Phase Changes on The Mechanical Properties of Alloys Near Composition TiNi, "J. Appl. Phys., Vol. 34, pp. 1475-1477.

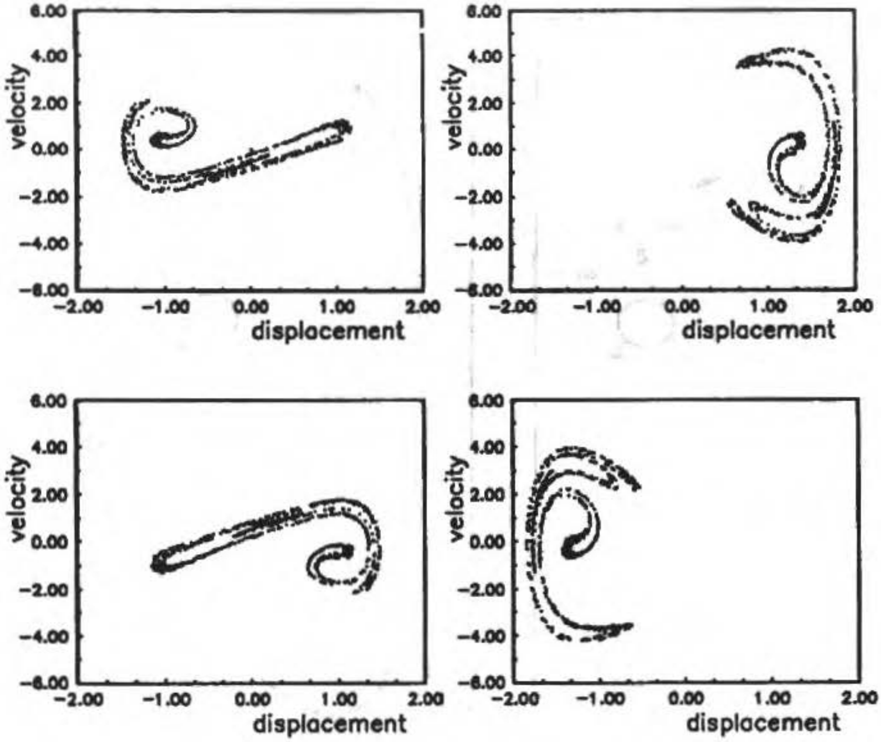

Fig. 16 Evolution of the chaotic attractor for different positions of the Poincaré section.
$\theta = 0.69$; $\xi = 5$ (a) $\varphi = 0$; (b) $\varphi = \pi/2$; (c) $\varphi = \pi$; (d) $\varphi = 3\pi/2$

Delaey, L., Krishnan, R.V., Tas, H. and Warlimont, H., 1974, "Thermoelasticity, Pseudoelasticity and The Memory Effects Associated with Martensitic Transformations, Part 1: Structural and Microstructural Changes Associated with the Transformations", J. Mat. Sci., Vol. 9, pp. 1521-1535.

Falk, F., 1982, "Landau Theory and Martensitic Phase Transitions", J. de Physique, Colloque C4, Suppl. 12, Tome 43, pp. 3-15.

Fremond, M., 1987, "Matériaux à Mémoire de Forme", C. R. Acad. Sc. Paris, Tome 304, s.II, No. 7, pp. 239-244.

Germain, P., 1973, Mécanique des Millieux Continus, Dunod, Paris.

Grebogi, C., Ott, E. and Yorke, J. A., 1983, "Crises, Sudden Changes in Chaotic Attractors, and Transient Chaos", Physica 7D, pp. 181-200.

Guckenheimer, J. and Holmes, P., 1983, Nonlinear Oscillations, Dynamical Systems, and Bifurcations of Vector Fields, Springer-Verlag, New York.

Jackson, C. M., Wagner, H. J. and Wasilewski, R. J., 1972, 55-Nitinol - The Alloy with a Memory: Its Physical Metallurgy, Properties, and Applications, NASA-SP-5110.

Liang, C. and Rogers, C. A., 1990, "A One-Dimensional Thermomechanical Constitutive Relation of Shape Memory Materials", Proceedings of the 31st Structure, Structural Dynamics and Materials Conference, paper AIAA-90-1027, Long Beach, CA, AIAA, pp. 2234-2241.

Luenberger, D. G., 1973, Introduction to Linear and Nonlinear Programming, Addison-Wesley, Reading, New Jersey.

Moon, F. C., 1987, Chaotic Vibrations, Wiley-Interscience, New York.

Rockafellar, R. T., 1970, Convex Analysis, Princeton Press, New Jersey.

Rogers, C. A., 1990, "Active Vibration and Structural Acoustic Control of Shape Memory Alloy Hybrid Composites: Experiemental Results", J. Acoust. Soc. of Am., Vol. 88, pp. 2803-2811.

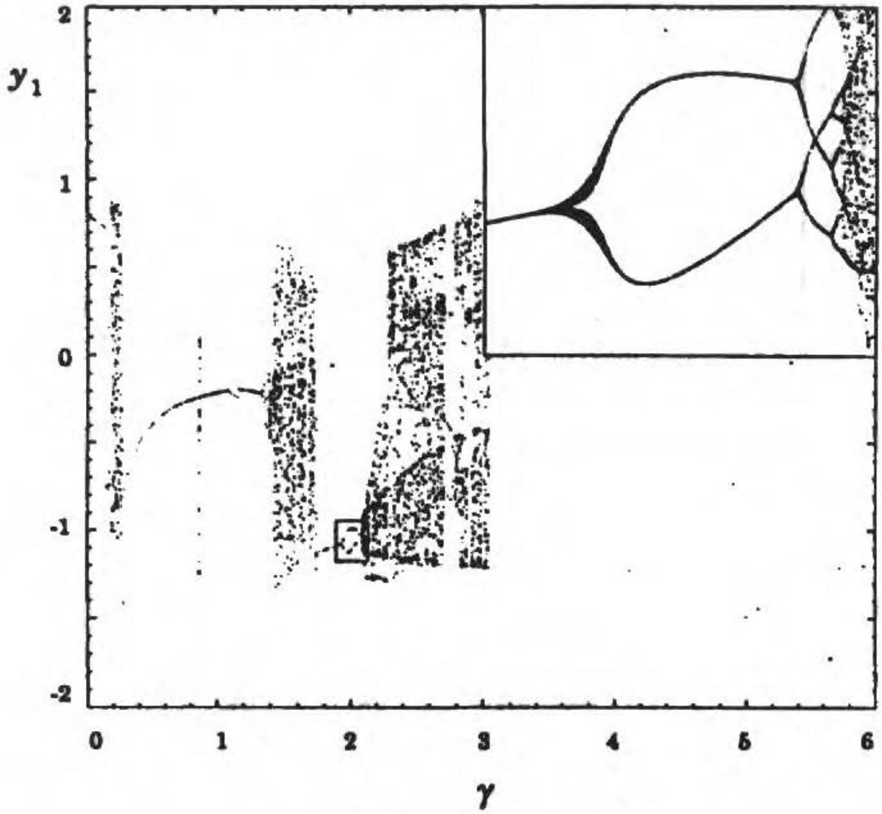

Fig. 17 Bifurcation diagram ($\xi = 0.2$, $\Omega = 1$

Rogers, C. A., Liang, C., and Jia, J., 1989, "Behavior of Shape Memory Alloys Reinforced Composite Plates, Part 1: Model, Formulation and Control Concepts", Proceeding of the 30th Structure, Structural Dynamics and Materials Conference, paper AIAA-89-1389, Mobile, AL, AIAA, pp. 2011-2017.

Rogers, C. A., Liang, C. and Fuller, C. R., 1991, "Modeling of Shape Memory Alloy Hybrid Composites for Structural Acoustic Control", J. Acoust. Soc. of Am., Vol. 89, pp. 210-220.

Sato, Y., Tanaka, K. and Kobayashi, S., 1985, "Pseudoelasticity and Shape Memory Effect Associated with Stress-Induced Martensitic Transformation: A Thermomechanical Approach", Trans. Japan Soc. Aero. Space Sci., Vol. 28, No. 81, pp. 150-160.

Savi, M. A. and Braga, A. M. B., 1993, "Chaotic Response of a Shape Memory Oscillator with Internal Constraints", accepted for publication in: Proceeding of the 12th. Brazilian Congress of Mechanical Engineering.

Schetky, L. M., 1979, "Shape Memory Alloys", Sci. Am., Vol. 241(5), pp. 68-76.

Shigley, J. E., 1972, Mechanical Engineering Design, 2nd. ed., McGraw-Hill Kogagusha, Tokyo.

Tanaka, K., 1985, "A Thermomechanical Sketch of Shape Memory Effect: One-Dimensional Tensile Behavior", Res. Mech., Vol. 18, p. 251.

Tanaka, K. and Nagaki, S., "A Thermomechanical Description of Materials with Internal Variables in the Process of Phase Transitions", Ing. Arch., Vol. 51, pp. 287-299.

Thompson, J. M. T. and Stewart, H. B., 1986, Nonlinear Dynamics and Chaos, John Willey and Sons, Chichester, England.

Tobushi, H. and TANAKA, K., 1990, "Deformation of a Shape Memory Alloy Helical Spring", JSME Int. J., Ser. I, Vol. 34(1), pp. 83-89.

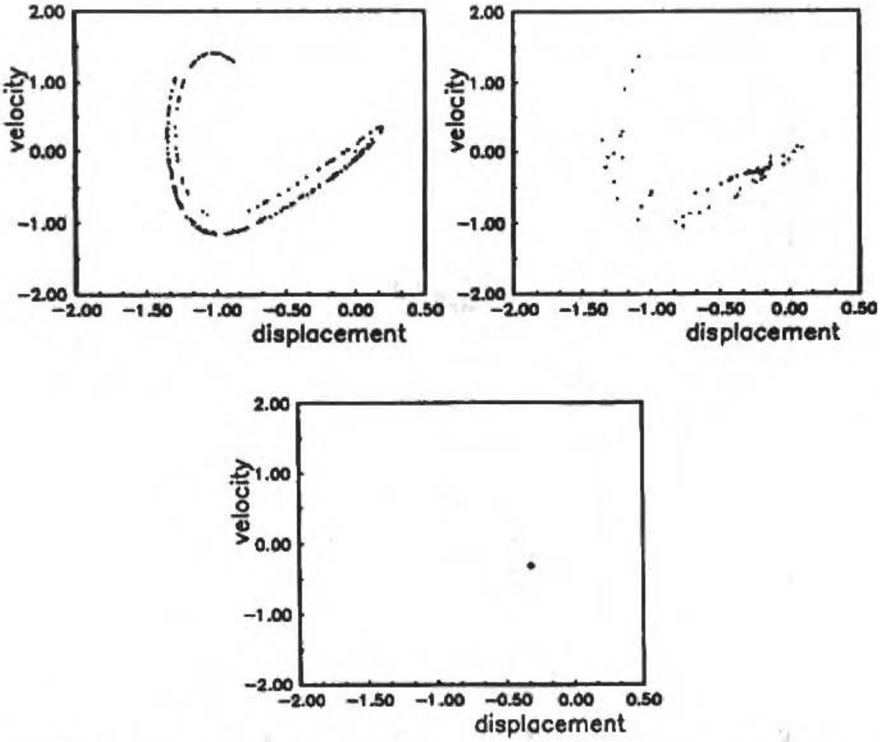

Fig. 18 Transition from chaotic to periodic response due to a variation in the system temperature $\theta_i = 0.69$; $\theta_f = 2.08$; $\xi = 0.5$; **(a) Chaotic response at constant temperature (b) Transient response; (c) Periodic response at the new temperature**

Venkatesh, A., Hilborn, J., Bidaux, J. E. and Gotthard, R., 1992, "Active Vibration Control of Flexible Linkage Mechanism Using Shape Memory Alloy Fiber Reinforced Composites", Proceedings of the 1st European Conference on Smart Structures and Materials, Glasgow, Scotland, IOP Publishing, pp. 185-188.

Warlimont, H., Delaey, L., Krishnan, R. V. and Tas, H., 1974, "Thermoelasticity, Pseudoelasticity and The Memory Effects Associated with Martensitic Transformations, Part 3: Thermodynamics and Kinetics", J. Mat. Sci., Vol. 9, pp. 1545-1555.

Wiggins, S., 1988, Global Bifurcations and Chaos, Springer-Verlag, New York.

Wiggins, S., 1990, Introduction to Applied Nonlinear Dynamical Systems and Chaos, Springer-Verlag, New York.

RBCM - J. of the Braz. Soc. Mechanical Sciences
Vol. XV - nº 1 - 1993 - pp. 21-30

ISSN 0100-7386
Printed in Brazil

An Inverse Problem for the Three Dimensional Vector Helmholtz Equation for a Perfectly Conducting Obstacle with Incomplete Data

Luciano Misici

Dipartimento di Matematica e Fisica
Università di Camerino - 62032 Camerino - Italy

Francesco Zirilli

Dipartimento di Matematica "G. Castelnuovo"
Università di Roma "La Sapienta" - 00185 Roma - Italy

Abstract

Let $D \subset R^3$ be a simply connected bounded domain with smooth boundary ∂D. We assume that ∂D is a perfectly conducting surface. In this paper we present a numerical method to reconstruct ∂D from the knowledge of the far field patterns generated by D when hit by time harmonic linearly polarized electromagnetic waves coming from several incoming directions.

Keywords: Inverse problem - Electromagnetic Theory - Obstacle Reconstructing.

Introduction

Let R^3 be the three dimensional real euclidean space, $\underline{x} = (x, y, z)^T \in R^3$ be a generic vector, where the superscript T means transpose, $(\cdot,\cdot)$ will denote the euclidean scalar product and $\|\cdot\|$ the euclidian norm. In the following we will use also complex vectors abusing occasionally of the notations.

Let $D \subset R^3$ be a bounded simply connected domain with smooth boundary ∂D that contains the origin. Let $\underline{E}^i(\underline{x})$ be the electric field associated to a linearly polarized time harmonic incoming wave propagating in a homogeneous isotropic medium, that is:

$$\underline{E}^i(\underline{x}) = \underline{w}_{\underline{\alpha}} e^{ik(\underline{x},\underline{\alpha})} \tag{1}$$

where $\underline{w}_{\underline{\alpha}}, \underline{\alpha} \in R^3$ with $\|\underline{\alpha}\| = 1$ are given and $k > 0$ is the wave number, moreover we assume that:

$$\operatorname{div}\underline{E}^i(\underline{x}) = ik(\underline{w}_{\underline{\alpha}}, \underline{\alpha}) e^{ik(\underline{x},\underline{\alpha})} = 0 \tag{2}$$

that is $\underline{w}_{\underline{\alpha}} \perp \underline{\alpha}$ so that $\underline{E}^i(\underline{x})$ is a divergence free vector field. We note that $\underline{w}_{\underline{\alpha}}$ is the polarization vector and $\underline{\alpha}$ is the direction of propagation of $\underline{E}^i(\underline{x})$.

Let $\underline{E}^s(\underline{x})$ be the electric field scattered by the obstacle D when hit by the incoming wave $\underline{E}^i(\underline{x})$, we denote with:

$$\underline{E}(\underline{x}) = \underline{E}^i(\underline{x}) + \underline{E}^s(\underline{x}) \tag{3}$$

the total electric field. It is easy to see (Colton and Kress, 1983, Chapter 4) that the time harmonic Maxwell's equations in an homogeneous isotropic medium that does not contain electric charges reduce to the vector Helmholtz equation for divergence free vector fields, so that the scattered field $\underline{E}^s(\underline{x})$ satisfies:

$$\Delta\underline{E}^s(\underline{x}) + k^2\underline{E}^s(\underline{x}) = 0 \text{ in } R^3 \setminus D \tag{4}$$

Manuscript received October 1992. Associate Technical Editor: Agenor de Toledo Fleury

$$\operatorname{div}\underline{E}^{s}(\underline{x}) = 0 \text{ in } R^{3} \setminus D \tag{5}$$

where $\Delta = \left(\frac{\partial^2}{\partial x^2} + \frac{\partial^2}{\partial y^2} + \frac{\partial^2}{\partial z^2}\right) I$ and I is the identity matrix acting on R^3.

The partial differential equations (4), (5) are equipped with boundary conditions, that is :

$$\underline{E}(\underline{x}) \times \underline{\nu}(\underline{x}) = 0 \;, \underline{x} \in \partial D \tag{6}$$

where $\underline{\nu}(\underline{x})$ is the exterior unit normal to D and × denotes the vector product, and

$$\operatorname{curl}\underline{E}^{s}(\underline{x}) \times \hat{\underline{x}} - ik\underline{E}^{s}(\underline{x}) = o\left(\frac{1}{\|\underline{x}\|}\right), \quad \|\underline{x}\| \to \infty \tag{7}$$

where $\hat{\underline{x}} = \frac{\underline{x}}{\|\underline{x}\|}, \; \underline{x} \neq 0$.

We note that (6) expresses the fact that D is a perfectly conducting obstacle and (7) is the Silver-Müller radiation condition at infinity. It can be shown (Colton and Kress, 1983) that $\underline{E}^s(\underline{x})$, solution of the boundary value problem (4), (5), (6), (7), has the following expansion:

$$\underline{E}^{s}(\underline{x}) = \frac{e^{ik\|\underline{x}\|}}{\|\underline{x}\|} \underline{E}_0\left(\hat{\underline{x}}, k, \underline{\alpha}, \underline{w}_{\underline{\alpha}}\right) + O\left(\frac{1}{\|\underline{x}\|^2}\right), \quad \|\underline{x}\| \to \infty \tag{8}$$

where $\underline{E}_0(\hat{x}, k, \underline{\alpha}, \underline{w}_{\underline{\alpha}})$ is the electric far field pattern generated by the obstacle D when hit by the incoming wave (1).

Let $B = \{\underline{x} \in R^3 \mid \|\underline{x}\| < 1\}$ be the unit aphere, and ∂B be its boundary, let:

$$\Omega_1 = \{\underline{\alpha}_i \in \partial B \mid i = 1, 2, \ldots, n_1\} \tag{9}$$

$$\Omega_2 = \{\underline{w}_{ij} \in \partial B \mid i = 1, 2, \ldots, n_1; j = 1, 2, \ldots, n_2\} \tag{10}$$

$$\Omega_3 = \{\hat{\underline{x}}_i \in \partial B \mid i = 1, 2, \ldots, n_3\} \tag{11}$$

be three given sets.

We restrict our attention to non resonant values of k, that is values such that $-k^2$ is not an eigenvalue for the vector Laplace operator in the interior of D restricted to divergence free vector fields with the boundary condition (6).

In this paper we present a numerical method to solve the following inverse problem:

Problem 1: From the knowledge of the nature of the obstacle (i.e. the fact that the obstacle is perfectly conducting) and of $\underline{E}_0(\hat{\underline{x}}_j, k, \underline{\alpha}_i, \underline{w}_{ij})$ for $\underline{\alpha}_i \in \Omega_1, \underline{w}_{ij} \in \Omega_2, \hat{\underline{x}}_j \in \Omega_3$ we want to recover the shape of the obstacle ∂D.

We note that Ω_1 is the set of the directions of the incoming waves, Ω_2 the set of the corresponding polarization vectors, that is we consider the plane waves coming in the direction α_i, polarized in the directions w_{ij}, $i=1,2,\ldots,n_1$; $j=1,2,\ldots,n_2$ and Ω_3 the set of the directions where the corresponding far fields are measured.

We call the available far field data incomplete since the far fields $\underline{E}_0$ are supposed to be known only in the directions $\hat{\underline{x}}_j \in \Omega_3$. In a previous paper (Maponi, Misici and Zirilli, 1991) we have considered the case when the coefficients of the expansion of $\underline{E}_0$ in vector spherical harmonics are used as data so that $\underline{E}_0$ is supposed to be known on ∂B.

The numerical method discussed here generalizes the one introduced in (Maponi, Misici and Zirilli, 1991) and is based on the so called "Herglotz function technique" introduced in Colton and Monk (1987) in the contest of the inverse acoustic scattering problem and further developed by the authors in Maponi, Misici and Zirilli (1991); Aluffi-Pentini et al. (1989, 1991), and Misici and Zirilli (1991). Numerically this method appears to be particularly effective in the resonance region that is when:

$$kL = 1 \tag{12}$$

where k is the wave number of the incoming wave and L is a characteristic length of the obstacle.

In the next section we recall the equation that are exploited to solve numerically the inverse Problem 1; after that we present the numerical method and finally some numerical experience. We remark that some numerical experience with very noisy data is shown.

Some mathematical relations

We recall some mathematical relations derived in (Maponi, Misici and Zirilli, 1991) that are used to solve numerically the inverse problem considered in the previous section. For $\underline{x},\underline{y} \in R^3$ let

$$\Phi(k\|\underline{x}-\underline{y}\|) = \frac{e^{ik\|\underline{x}-\underline{y}\|}}{4\pi\|\underline{x}-\underline{y}\|} \tag{13}$$

be the Green's function of the (scalar) Helmholtz operator with the Sommerfeld radiation condition at infinity. Let $\underline{g}(\hat{\underline{x}})$ be a square integrable vector valued complex function defined on the surface of the unit sphere ∂B, such that:

$$(\hat{\underline{x}}, \underline{g}(\hat{\underline{x}})) = 0, \quad \forall \hat{\underline{x}} \in \partial B \tag{14}$$

and let

$$\underline{E}_1(\underline{y}) = \int_{\partial B} \underline{g}(\hat{\underline{x}})\, e^{ik(\hat{\underline{x}},\underline{y})}\, d\lambda(\hat{\underline{x}}) \tag{15}$$

where $d\lambda(\hat{\underline{x}})$ is the surface measure on ∂B. It is easy to see that $\underline{E}_1(\underline{y})$ is a divergence free vector field that satisfies the vector Helmholtz equation for any $\underline{y} \in R^3$. Let $\underline{v} \in R^3$ be a given vector, we define the vector function

$$\underline{M}(\underline{y}) = -4\pi \left\{ \underline{v}\,\overline{\Phi(k\|\underline{x}-\underline{y}\|)} + \frac{1}{k^2}\nabla_{\underline{x}}\,(\underline{v}, \nabla_{\underline{x}}\,\overline{\Phi(k\|\underline{x}-\underline{y}\|)}) \right\}\Bigg|_{\underline{x}=0} \tag{16}$$

where $\nabla_{\underline{x}}$ is the gradient operator with respect to $\underline{x}$, and $\overline{\Phi}$ is the complex conjugate of Φ. We remind that $0 \in D$.

Definition 1: The domain D is said to be a generalized Herglotz domain if the unique solution of the boundary value problem:

$$(\Delta + k^2)\underline{E}_1(\underline{y}) = 0 \text{ in } D \tag{17}$$

$$\mathrm{div}\underline{E}_1(\underline{y}) = 0 \text{ in } D \tag{18}$$

$$\underline{\nu}\times\underline{E}_1(\underline{y}) = \underline{\nu}\times\underline{M}(\underline{y}) \text{ on } \partial D \tag{19}$$

is given by (15) for a suitable choice $\underline{g}_H(\hat{\underline{x}})$ of $\underline{g}(\hat{\underline{x}})$. The function $\underline{g}_H(\hat{\underline{x}})$ that corresponds to the solution of (17), (18), (19) is said to be the generalized Herglotz kernel associated to the domain D.

We note that the Herglotz kernel depends on $\underline{\nu}$ and that the class of the generalized Herglotz domains is not empty since an explicit computation shows that the sphere of center the origin is a generalized Herglotz domain.

It has been shown (Maponi, Misici and Zirilli, 1991) that:

$$\int_{\partial B}\left(\overline{\underline{g}(\hat{\underline{x}})}, \underline{E}_0\left(\hat{\underline{x}}, k, \underline{\alpha}, \underline{w}_{\underline{\alpha}}\right)\right)d\lambda(\hat{\underline{x}}) = (\underline{w}_{\underline{\alpha}}, \underline{\nu}), \quad \forall\underline{\alpha}\in\partial B, \underline{w}_{\underline{\alpha}}\in R^3 \tag{20}$$

The inverse Problem 1 proposed will be solved in three steps:

(i) from the knowledge of the far fields $\underline{E}_0(\hat{\underline{x}}_j, k, \underline{\alpha}_i, \underline{w}_{ij})$, $\underline{\alpha}_i\in\Omega_1$, $\underline{w}_{ij}\in\Omega_2$, $\hat{\underline{x}}_j\in\Omega_3$, using (20), determine an approximation of the generalized Herglotz kernel $\underline{g}_H(\hat{\underline{x}})$ of the domain D.

(ii) from $\underline{g}_H(\hat{\underline{x}})$, obtained in (i), and (15) determine $\underline{E}_1(\underline{y})$.

(iii) from $\underline{E}_1(\underline{y})$, obtained in (ii) and (19) determine ∂D.

The numerical method

Let (r,θ,ϕ) be the spherical coordinates, we have:

$$\hat{\underline{x}}(\theta,\phi) = (\sin\theta\cos\phi, \sin\theta\sin\phi, \cos\theta) \tag{21}$$

$$\underline{a}_\theta(\theta,\phi) = (\cos\theta\cos\phi, \cos\theta\sin\phi, -\sin\theta) \tag{22}$$

$$\underline{a}_\phi(\theta,\phi) = (-\sin\phi, \cos\phi, 0) \tag{23}$$

It is easy to see that for each θ and ϕ $(\hat{\underline{x}}, \underline{a}_\theta, \underline{a}_\phi)$ is an orthonormal basis of R^3.

Let

$$U_{l,m}(\hat{\underline{x}}) = \gamma_{l,m}P_l^m(\cos\theta)\cos(m\phi), \quad l = 0, 1, \ldots;\ m = 0, 1, \ldots, l \tag{24}$$

$$V_{l,m}(\hat{\underline{x}}) = \gamma_{l,m}P_l^m(\cos\theta)\sin(m\phi), \quad l = 1, 2, \ldots;\ m = 1, 2, \ldots, l \tag{25}$$

be the spherical harmonics, that is P_l^m are the Legendre functions and $\gamma_{l,m}$ are the normalization factors in $L^2(\partial B, d\lambda(\hat{\underline{x}}))$.

We define the spherical vector harmonics (Morse and Feshbach, 1953, p. 1898):

$$\underline{B}_{l,m}^{0,0}(\hat{\underline{x}}) = \hat{\underline{x}}U_{l,m}(\hat{\underline{x}}), \quad l = 0, 1, \ldots;\ m = 0, 1, \ldots, l \tag{26}$$

$$\underline{B}_{l,m}^{1,0}(\hat{\underline{x}}) = \hat{\underline{x}}V_{l,m}(\hat{\underline{x}}), \quad l = 1, 2, \ldots;\ m = 1, 2, \ldots, l \tag{27}$$

$$\underline{B}_{l,m}^{0,1}(\hat{\underline{x}}) = (l(l+1))^{-\frac{1}{2}}\|\underline{x}\|\nabla U_{l,m}(\hat{\underline{x}}), \quad l = 1, 2, \ldots;\ m = 0, 1, \ldots, l \tag{28}$$

$$\underline{B}^{1,1}_{l,m}(\hat{\underline{x}}) = (l(l+1))^{-\frac{1}{2}} \|\underline{x}\| \nabla V_{l,m}(\hat{\underline{x}}), \quad l = 1, 2, \ldots; \ m = 1, 2, \ldots, l \qquad (29)$$

$$\underline{B}^{0,2}_{l,m}(\hat{\underline{x}}) = (l(l+1))^{-\frac{1}{2}} \operatorname{curl}(\underline{x} U_{l,m}(\hat{\underline{x}})), \quad l = 1, 2, \ldots; \ m = 0, 1, \ldots, l \qquad (30)$$

$$\underline{B}^{1,2}_{l,m}(\hat{\underline{x}}) = (l(l+1))^{-\frac{1}{2}} \operatorname{curl}(\underline{x} V_{l,m}(\hat{\underline{x}})), \quad l = 1, 2, \ldots; \ m = 1, 2, \ldots, l \qquad (31)$$

It is well known that the spherical vector harmonics are an orthonormal basis of $L^2(\partial B, C^3, d\lambda(\hat{\underline{x}}))$, that is the set of square integrable complex vector functions defined on ∂B.

Our computation proceeds in four steps:

Step 1: For each (i,j) compute the "Fourier coefficients" of $\underline{E}_0(\hat{\underline{x}}, k, \underline{\alpha}_i, \underline{w}_{i,j})$.

Given $L_{max} > 0$ we assume that the far field $\underline{E}_0(\hat{\underline{x}}, k, \underline{\alpha}_i, \underline{w}_{i,j})$ can be approximated by a truncated Fourier series, that is

$$\underline{E}_0(\hat{\underline{x}}) = \sum_{\tau=1,2} \sum_{s=0,1} \sum_{l=1}^{L_{max}} \sum_{m=s}^{l} f^{s,\tau}_{i,j,l,m} \underline{B}^{s,\tau}_{l,m}(\hat{\underline{x}}) \qquad (32)$$

so that we have

$$\sum_{\tau=1,2} \sum_{s=0,1} \sum_{l=1}^{L_{max}} \sum_{m=s}^{l} f^{s,\tau}_{i,j,l,m} \underline{B}^{s,\tau}_{l,m}(\hat{\underline{x}}_k) = \underline{E}_{0,ijk}; \quad k = 1, 2, \ldots, n_3 \qquad (33)$$

where with $\underline{E}_{0,ijk}$ we have indicated the measurement of $\underline{E}_0(\hat{\underline{x}}, k, \underline{\alpha}_i, \underline{w}_{i,j})$.

The equations (33) are a linear system of n_3 equations in the $2L_{max}(L_{max}+2)$ unknowns $\{f^{s,\tau}_{i,j,l,m}\}$. We assume that Ω_3 and L_{max} are chosen in such a way that the linear system (33) is determined.

Due to the ill-conditioning of the linear system (33) several regularizing techniques will be used when solving (33) in the next section. In the numerical experience choosing $n_2=1$ and $w_{i,1}$ appropriately we can drop the terms with $\tau=2$, $s=0$ and with $\tau=1$, $s=1$ in the sum on the left hand side of (33).

The Steps 2,3,4 of the numerical method described here are the same as the ones described in (Maponi, Misici and Zirilli, 1991) and will not be reported in detail.

Step 2: From the Fourier coefficients of $\underline{E}_0(\hat{\underline{x}}_j, k, \underline{\alpha}_i, \underline{w}_{ij})$, $i=1,2,\ldots,n_1$, $j=1,2,\ldots,n_2$ to the generalized Herglotz kernel $g_H(\hat{\underline{x}})$.

This Step is based on (20) and corresponds to the solution of a linear system.

Step 3: From the generalized Herglotz kernel $g_H(\hat{\underline{x}})$ to $\underline{E}_1(\underline{y})$.

This Step is based on (15) and is based on an analytic formula. No numerical integration is needed.

Step 4: From $\underline{E}_1(\underline{y})$ to the boundary of the obstacle ∂D.

This Step is based on (19).

The numerical experience

The surfaces ∂D considered are the following ones:

1 Oblate Ellipsoid $$\left(\frac{2}{3}x\right)^2 + \left(\frac{2}{3}y\right)^2 + z^2 = 1 \qquad (34)$$

2 Prolate Ellipsoid $$x^2 + y^2 + \left(\frac{2}{3}z\right)^2 = 1 \qquad (35)$$

3 Short Cylinder $$\left(\left(\frac{2}{3}x\right)^2+\left(\frac{2}{3}y\right)^2\right)^3+z^6=1 \qquad (36)$$

4 Long Cylinder $$(x^2+y^2)^3+\left(\frac{2}{3}z\right)^6=1 \qquad (37)$$

5 Vogel's Peanut $$r=\frac{2}{3}\left(\cos^2\theta+\frac{1}{4}\sin^2\theta\right)^{\frac{1}{2}} \qquad (38)$$

6 Horizontal Platelet $$r=1-\frac{1}{2}\cos 2\theta \qquad (39)$$

7 Reverse Platelet $$r=\frac{5}{4}+\frac{1}{4}\cos 4\theta \qquad (40)$$

8 Vertical Peanut $$r=1+\frac{1}{2}\cos 2\theta \qquad (41)$$

9 Pseudo Ellipsoid $$r=\frac{3}{5}\left(\frac{17}{4}+2\cos 3\theta\right)^{\frac{1}{2}} \qquad (42)$$

We note that the Short Cylinder and the Long Cylinder are used in Maponi, Misici and Zirilli (1991), Colton and Monk (1987), Aluffi-Pentini et al. (1991) and Misici and Zirilli (1991) with the exponent 10 instead of 6. That is the edges of the cylinders considered here are smoother than the ones of the cylinders considered in the previously quoted references. We note that for the obstacles considered $\partial D=\{(r,\theta,\phi)\mid r=f(\theta,\phi);0\le\theta\le\pi,0\le\phi<2\pi\}$ for a suitable choice of $f(\theta,\phi)$.

All these obstacles are cylindrically symmetric with respect to the z-axis and the surfaces 1, 2, 3, 4, 5, 6, 7, 8 are also symmetric with respect to the equator.

These symmetries are always exploited (see Aluffi-Pentini et al., 1991) in the reconstructions shown in Tables 1 and 2 to reduce the number of the coefficients to be determined in the expansions of the generalized Herglotz kernels and of the functions $f(\theta,\phi)$ that represent the unknown surfaces.

We note that for all the obstacles considered here we can choose the characteristics lenght L=1. The synthetic data $\underline{E}_{0,ijk}$ are obtained solving the boundary value problem (4), (5), (6), (7) using a T-matrix approach (Kristensson and Waterman, 1982). To these synthetic data we add a random noise term, so that the data used in the reconstructions are

$$(1+\varepsilon\zeta)\underline{E}_{0,ijk} \qquad (43)$$

where ε is a parameter and ζ is a random number uniformly distributed in [-1,1]. Finally the sets Ω_1, Ω_2, Ω_3 are chosen between the following ones:

$$A_1=\{\underline{\alpha}_i=\underline{\hat{x}}(\theta_i,0)\mid\theta_i=i\frac{\pi}{10},i=0,1,\dots,10\} \qquad (44)$$

$$P_1=\{w_{i1}=(\cos\theta_i,0,-\sin\theta_i)^T\theta_i=i\frac{\pi}{10},i=0,1,\dots,10\} \qquad (45)$$

$$B_1=\{\underline{\hat{x}}(\theta_i,\phi_j)\mid\theta_i=i\frac{\pi}{10},i=1,2,\dots,9,\phi_j=j\frac{2\pi}{9},j=0,1,\dots,8\}\cup\{\underline{\hat{x}}(0,0)\}\cup\{\underline{\hat{x}}(0,\pi)\} \qquad (46)$$

$$B_2=\{\underline{\hat{x}}(\theta_i,\phi_j)\mid\theta_i=i\frac{\pi}{10},i=1,2,\dots,9,\phi_j=j\frac{\pi}{48},j=0,1,\dots,8\}\cup\{\underline{\hat{x}}(0,0)\}\cup\{\underline{\hat{x}}(0,\pi)\} \qquad (47)$$

Moreover for j=0,1,...,36 let $\theta_j = \frac{\pi j}{36}$, $f(\theta_j, 0)$ be the exact values of the surfaces ∂D considered and $f_c(\theta_j,0)$ be the values reconstructed performing the numerical procedure described. The relative L^2 error at the points $\{(\theta_j,0) | j=0,1,...,36\}$ is given by:

$$E_{L^2} = \left[\frac{\sum_{j=0}^{36} (f(\theta_j, 0) - f_c(\theta_j, 0))^2}{\sum_{j=0}^{36} f^2(\theta_j, 0)} \right]^{\frac{1}{2}} \tag{48}$$

We use L^2 as a performance index for the reconstruction procedure. The results obtained are shown in Tables 1 and 2 and Figures 1, 2, 3 and 4.

Table 1 The numerical results
$L_{max}=7$, $\Omega_1=A_1$, $\Omega_2=P_1$, $\Omega_3=B_1$

Object	Reconstruction	k	ε	E_{L^2}
Oblate Ellipsoid	1	3	0.0	0.0047
Oblate Ellipsoid	2	3	0.05	0.0231
Prolate Ellipsoid	3	3	0.0	0.0323
Prolate Ellipsoid	4	3	0.05	0.0234
Short Cylinder	5	3	0.0	0.0216
Short Cylinder	6	3	0.05	0.0895
Long Cylinder	7	3	0.0	0.0449
Long Cylinder	8	3	0.05	failure
Vogel's Peanut	9	3	0.0	0.0067
Vogel's Peanut	10	3	0.05	0.0315
Horizontal Platelet	11	3	0.0	0.0956
Horizontal Platelet	12	3	0.05	failure
Reverse Platelet	13	4	0.0	0.0128
Reverse Platelet	14	4	0.05	0.0122
Vertical Peanut	15	4	0.0	0.0334
Vertical Peanut	16	4	0.05	failure
Pseudo Apollo	17	4	0.0	0.0814
Pseudo Apollo	18	4	0.05	0.0795

Table 2 Performance as function of ε
Object= Oblate Ellipsoid, $L_{max}=7$, $k=3$
$\Omega_1=A_1$, $\Omega_2=P_1$, $\Omega_3=B_2$

Reconstruction	ε	E_{L^2}
1	0.0	0.0713
2	0.01	0.0493
3	0.05	0.0375
4	0.10	0.0308
5	0.20	0.0321
6	0.30	0.0394
7	0.40	0.0493
8	0.60	0.0775
9	0.80	0.1178

Table 1 shows that when $\varepsilon=0.05$ a satisfactory reconstruction of a large class of "simple" surfaces is possible and Table 2 shows that when only "very simple" surfaces are considered satisfactory reconstructions are possible even from very noisy data.

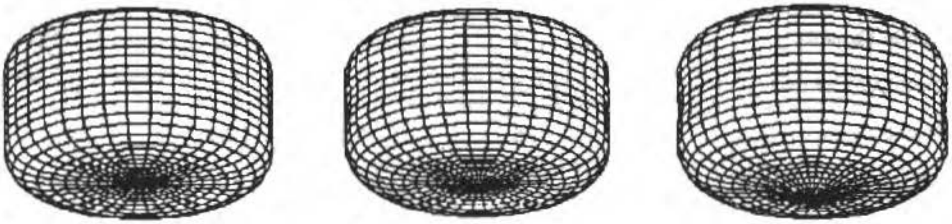

Original Reconstruction 5 of table 1 Reconstruction 6 of table 1

Fig. 4.1 Short Cylinder

Original Reconstruction 9 of table 1 Reconstruction 10 of table 1

Fig. 4.2 Vogel's Peanut

Original Reconstruction 17 of table 1 Reconstruction 18 of table 1

Fig. 4.3 Pseudo Apollo

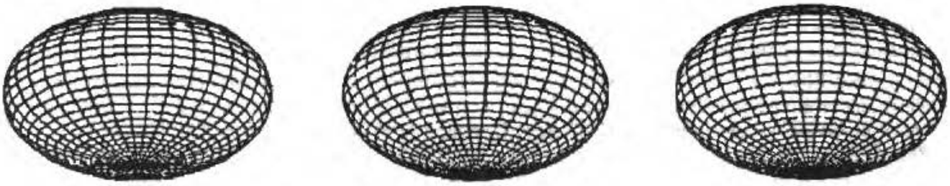

Original Reconstruction 2 of table 2 Reconstruction 6 of table 2

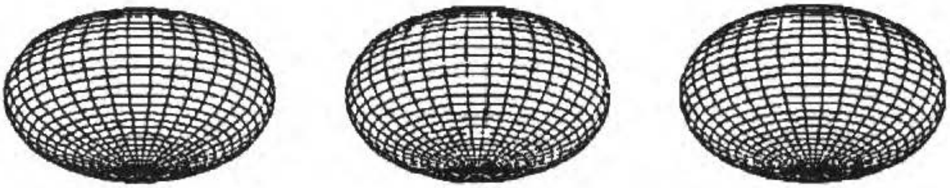

Reconstruction 4 of table 2 Reconstruction 5 of table 2 Reconstruction 6 of table 2

Reconstruction 7 of table 2 Reconstruction 8 of table 2 Reconstruction 9 of table 2

Fig. 4.4 Oblate Ellipsoid

Acknowledgements

The research reported in this paper has been made possible through the support and sponsorship of the Italian Government through the Ministero per l'Università e per la Ricerca Scientifica under contract MURST 40%, 1990.

References

Aluffi-Pentini, F.; Caglioti, E.; Misici, L. and Zirilli, F., 1989, "A parallel algorithm for a three dimensional inverse acoustic scattering problem" in "Parallel Computing: methods, algorithms and applications", D. J. Evans, C. Sutti Editors, IOP Publishing, Bristol, 193-200.

Aluffi-Pentini, F.; Caglioti, E.; Misici, L. and Zirilli, F., 1991, "A numerical method fo rthe three dimensional inverse acoustic scattering problem with incomplete data" in "Advances in numerical partial differential equations and optimization", S. Gomez, J. P. Hennart, R. A. Tapia Editors, SIAM Proceedings Series, Philadelphia, 273-283.

Colton, D. and Kress, R., 1983, "Integral equation methods in scattering theory", J. Wiley & Sons Publ., New York.

Colton, D and Monk, P. , 1987, "The numerical solution of the three dimensional inverse scattering problem for time harmonic acoustic waves", SIAM J. Sci. Stat. Comput. 8, 278-291.

Kristensson, G. and Waterman, P. C., 1982, "The T matrix for acoustic and electromagnetic scattering by circular disks", J. Acoust. Soc. Amer. 72, 1612-1625.

Maponi, P.; Misici, L. and Zirilli, F., 1991, "An inverse problem for the three dimensional vector Helmholtz equation for a perfectly conducting obstacle", Computers Math. Applic., Vol. 22, 4/5, 137-146.

Misici, L. and Zirilli, F., 1991, "An inverse problem for the three dimensional Helmholtz equation with Neumann or mixed boundary conditions: a numerical method" in "Mathematical and numerical aspects of wave propagation phenomena", G. Cohen, L. Halpern, P. Joly Editors, SIAM Proceeding Series, Philadelphia, 497-508.

Morse, P. M. and Feshbach, H. , 1953, "Methods of theoretical physics", Part II, Mc Graw Hill Book Company, New York.

RBCM - J. of the Braz. Soc. Mechanical Sciences
Vol. XV - nº 1 - 1993 - pp. 31-41

ISSN 0100-7386
Printed in Brazil

Vibration Tests of Liquid Storage Thin Cylindrical Vessels

Testes de Vibração de Cilindros Finos com Líquido

João Carlos Menezes
CTA - ITA - IEMP
12225 - São José dos Campos - SP

Jayantilal Mistry
University of Liverpool
Department of Mechanical Engineering
PO Box 147, Brownlow Hill
Liverpool L69 3BX, U. K.

Abstract

Theoretical investigations employing a Finite Element solution of the dynamic behavior of a cylindrical vessel filled with liquid have been published previously by the authors. This paper describes the experimental procedure utilised in the verification of the theoretical predictions of the coupled problem. Five steel specimens were prepared from thick tubes using a numerically controlled lathe. The base of the cylindrical specimens was attached to a large circular disk. Tests were carried out with the cylinders filled without any liquid in the first instance to determine and identify their natural frequencies. The cylinders were then filled to different heights with water and tested. The experimental procedure involved mounting the empty cylinder vertically on a shaker which was oscillated sinusoidally. The work describes a novel method of using only two piezoelectric accelerometers and placing them at two pre-determined angular locations, for the clear identification of the circumferential wave numbers of the normal modes.
Keywords: Fluid Structure Interation, Vibration Tests, Liquid Storage Vessels.

Sumário

Detalhes de uma investigação teórica que adota o método dos Elementos Finitos na solução do comportamento vibracional de um vaso cilíndrico contendo líquido foram publicados anteriormente pelos autores. Esse artigo descreve o procedimento experimental utilizado na comparação com os resultados teóricos do problema acoplado. Cinco corpos de prova foram confeccionados por um torno de controle numérico a partir de tubos de parede grossa. A base dos corpos de prova cilíndricos foram engastadas a um disco circular rígido. Primeiramente os vasos foram ensaiados na ausência do líquido com o objetivo de se determinar e identificar as frequências naturais da casca. Os cilindros foram então preenchidos com líquido em diversos níveis e testados novamente. Nos experimentos o cilindro foi montado verticalmente sobre a cabeça de um "shaker" sob excitação harmônica simples. Os números de onda circunferenciais correspondentes foram identificados com o uso de dois acelerômetros colados à parede do vaso em posições angulares pré-definidas. As amplitudes e diferenças de fase dos sinais permitiram a clara identificação dos modos circunferenciais.
Palavras chave: Testes de Vibração, Vasos Cilíndricos para Armazenagem de Água

Introduction

In a previous investigation (Menezes and Mistry, 1991 a, b, c), the transient motion of a cylindrical vessel containing incompressible and viscous fluid was simulated using axisymmetric two-noded shell finite elements and eight-noded isoparametric fluid finite elements. Galerkin's weighted residual procedure had been employed for the Navier-Stokes equations expressed in polar co-ordinates in order to derive the finite element equations of the fluid medium. For the wall of the cylinder, classical linear shell theory of Novozhilov had been employed. The transient coupled equations had been solved with the aid of the Newmark average acceleration procedure and in the case of the fluid equations, Euler's backward difference scheme was utilised. An acceptable assumption made regarding the fluid motion contained in a cylinder is that the lower zone of the fluid is relatively static and it may be regarded as a stationary mass and the upper zone represents a mass which moves in the sloshing mode. A similar concept is adopted in the numerical analysis to take advantage of this property. It involves a refined mesh for the layer of fluid just below the free surface. The main aim of this investigation was to estimate the vibration frequencies of the shell wall in the low range of the frequencies and in this range, one

Manuscript received March 1993. Associate Technical Editor: Agenor de Toledo Fleury

expects the "beam-type" modes to predominate. In order to induce these modes, initial disturbing force as a linear function of the distance from the base was imposed on the vessel.

The present work concerns the experimental verification of those theoretical predictions. Five steel specimens were prepared from thick tubes using a numerically controlled lathe. The inner surface was machined to fit a mandrel and then the outer surface was turned down to the required size. The base of the cylindrical specimens was attached to a large circular disk. The experimental procedure involved the mounting the empty cylinder vertically on a shaker which was oscillated sinusoidally. The resonance frequency corresponding to large amplitude vibrations was measured using a digital frequency meter. The number of circumferential waves of the mode of vibration at a natural frequency was identified using two accelerometers at pre-determined angular locations which clearly highlighted the mode shapes by the characteristic phase difference existing at the two measuring points. The cylinders were then filled to different heights with water and transient tests were performed using a spectrum analyser.

Experimental Procedure - Mode Identification Procedure

The empty shell analysis has the purpose of identifying the circumference and longitudinal waves of the modes. In order to identify the modes, the specimen has to be externally excited at the mode's own natural frequency.

A common method of excitation is to fix the base of the vessel on a shaking table, harmonically excited in the horizontal direction (Yamaki; Tani and Yamaji (1984) and Chiba et al. (1986)). Alternatively, the base can be kept static and an eletromagnetic shaker can be attached to one or two points of the wall (Yamaki, Tani and Yamaji (1984); Ross and Johns (1983); Ross, Johns and Johns (1987), and Ross and Johns (1986)).

The excitation in the present case is performed by a shaker in a vertical position connected to the base of the vessel. Fig. 1 shows a schematic diagram of the mode identification experimental procedure. Two accelerometers are radially positioned at two points along the circumferential direction at the top of the cylinder. These positions are well defined before the measurements start. The two signals from the accelerometers are amplified and sent to a phase meter and an oscilloscope. One of this amplified signals is also sent to a frequency meter. Through the shaker controller, the frequency is varied until one of the resonances is found which can be identified by the maximum amplitude observed on the oscilloscope. The amplitude of the excitation displacement may also be suitably adjusted on the controller. Amplitudes, phase and frequency are then read.

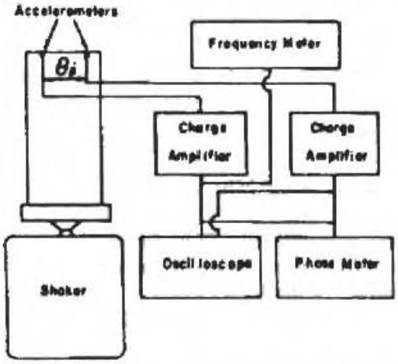

Fig. 1 Schematic diagram of experimental procedure.

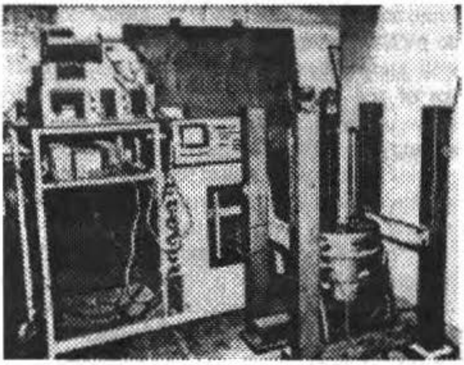

Fig. 2 Overall view of the mode identification test set up.

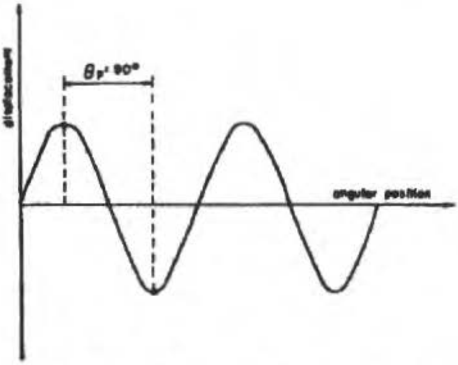

Fig. 3 Illust. of a phase and amplitude measurement with two accelerometers

A general view of the empty shell experimental instrumentation and a test cylinder is shown in Fig. 2. The concept of the measurements is that a certain circumferential mode will correspond to a certain angular position of the accelerometers where a certain phase is expected and in this condition, the amplitudes at both points have to be the same. This condition is illustrated in Fig. 3, which represents the expected response of the circumferential mode n=2, along the circumferential direction. In this case, for any two points separated by 90 along the circumferential direction, the expected readings of the two accelerometers signals is a 180 phase of equal amplitudes. Calling θ_p the angle which defines the accelerometers positions, for n=1 to n=5, the corresponding θ_p for a expected 180 phase are:

n=1	$\theta_p=180$
n=2	$\theta_p=90$
n=3	$\theta_p=60$
n=4	$\theta_p=45$
n=5	$\theta_p=36$

These conditions are illustrated in Fig. 4. Alternatively, one may want to measure a 0 phase to identify the mode, and in this case the corresponding θ_p should be taken as the double of the value given above. Therefore this option eliminates the possibility of identifying the n=1 mode.

Two couples of accelerometers were used in the tests: Endevco, Model 226C, sensitivities 2.8 and 2.84 pC/g and Bruel & Kjaer, Model 4333, sensitivities 17.0 and 18.2 pC/g.

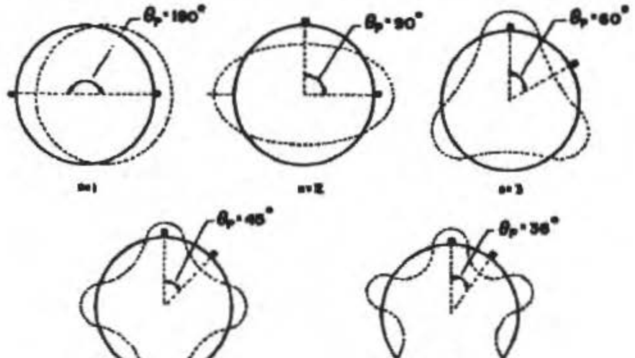

Fig. 4 Illustration of several circumferential modes and the corresponding accelerometer positions.

Its convenient to discuss what may happen when the accelerometers are ill-positioned for a certain mode. When searching for the circunferential mode n=2, as exemplified in Fig. 3, one expects for θ_p=90 a 180 phase and equal amplitudes. It is well known fact that one of the major problems associated with accelerometers is the interference of the mass of the accelerometer with the measurement (Ewins, 1985). In the tests done, it has been observed that the added mass of the accelerometer to the system has the effect of lowering the natural frequency at the mode being investigated. The decrease of the natural frequency, in this case, does not alter the interpretation of the results, since the actual frequency can be measured experimentally at lower positions of the vessel where the shell has a higher equivalent rigidness and is less sensitive to the presence of the accelerometer. On the other hand, sometimes, the presence of the accelerometer has a "beneficial" effect of stimulating the occurrence of the lobes at the point where they are positioned. In other words, if the system is sensitive enough to the mass of the accelerometer, the nodes will not occur at the accelerometer position. With this fact in mind, one may want to predict what happens when the accelerometers are ill-positioned for the mode being investigated.

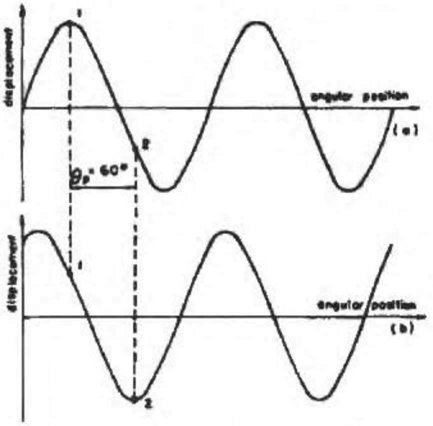

Fig. 5 An expected bahaviour of the mode when the accelerometers are ill-positioned.

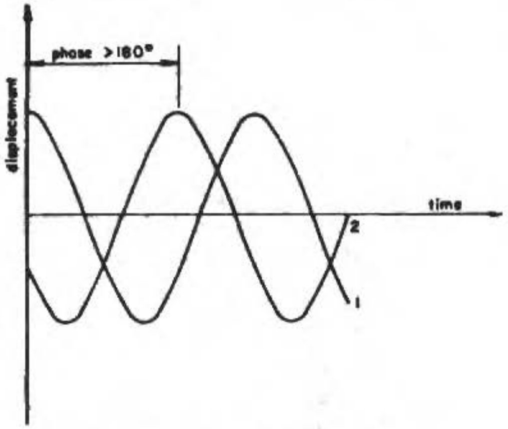

Fig. 6 Displacement versus time for ill-positioned accelerometers

Suppose that at a frequency which stimulates the circumferential mode n=2, two accelerometers, having the same mass, are positioned 60 apart. Suppose also that the system is sensitive to the mass of the accelerometer. In this condition there will be no preferential accelerometer position where the lobes should be formed. Either point 1 or point 2 on the wall, as illustrated in Fig. 5, have the same chance of being the point where the normal displacement will be maximum. Now, suppose that at a certain time illustrated by Fig. 5(a), point 1 at the wall has reached the maximum displacement. At this time, the maximum displacement at point 2 is yet to be reached. Fig. 5(b) illustrates the condiction when a certain time has passed and point has reached the maximum displacement and point 1 has now a smaller displacement than at the time illustrated by Fig. 5(a). If the two displacement measure by the two accelerometers are recorded along the time, starting from condition (a), and taking position 1 as a reference, the result will be that illustrated by Fig. 6. This figure illustrates a phase greater than 180 expected if the accelerometers were positioned with θp=90 . The same idea could be applied to a condition where the positions of the accelerometers were set by θ_p>90 for n=2. The expected phase, then, would be less than 180 .

Another possibility is that the system is not affected by the mass of the sensors which would be the case if the sensor is light enough or it is a non-contacting one. For ill-positioned sensors, taking as an example the case n=2 and θ_p=60 , one can expect one of the three cases described below:

1) The phase will be 180 but the amplitudes will be different in magnitude. In this case the sensors would be unsymmetrically positioned with respect to the node.

2) The phase will be 0 and the amplitudes will be either equal or different. It would happen if the two sensors are positioned in between nodes.

3) The phase will be 180 and the amplitudes will be the same in magnitude. Exceptionally, the sensors might be positioned symmetrically with respect to a node. In such case, since this result is expected for the mode n=3 and a well-positioned accelerometers (because $\theta_p=60$), the results should be rechecked with a new position of the second sensor. For example, if the second sensor were repositioned at $2\theta_p$ from the first, the expected reading is equal amplitudes and phase equal to 0 for n=3, which will not be the case if all other conditions were maintained.

The discussion above is based on attempts of the authors to use light accelerometers on thicker specimens. In such condition there is a possibility of obtaining equal results to different modes, which obviously is not compatible with the goals of the method.

Test of the Vessel Filled with Water

After each of the chosen modes and correlated frequencies were identidied, a test with the vessel filled with water was performed. The goal of this test was to register the alteration of modes with the increasing height of the water level. The height of the water in the vessel was increased in steps of 25 mm and frequencies were obtained from a transient excitation. A hammer was used to laterally impact the wall of the vessel and frequencies were measured by a spectrum analyser through an amplified signal of an accelerometer placed on the wall of the vessel. These tests were performed with the base of the cylinder placed on a rigid iron table. Changes of the frequency for each of these small increases in height are not appreciable, and therefore the correlated mode remains identified during the test until the vessel is fully filled with water.

A preliminary test was done in order to find out the best position of the accelerometer on the wall of the vessel. For the empty vessel with a nominal thickness h=1.2 mm, using a accelerometer with a charge sensitivity=17 pc/g, an amplification of 50 g/V, and a input range of 0.1 V on the spectrum analyser, four transient tests were carried out with the accelerometers positioned at heights 300, 200, 100 and 50 mm. For two frequency ranges of the spectrum analyser, 0-512 and 0-1024 Hz, the frequency of the wave numbers n=1 to n=5 were registered. Results reveal higher frequencies values for the 50mm height compared with the greater heights. Since the results show a smaller interference of the mass of the accelerometer and also because of the sufficient sensitivity of the accelerometer at this point, the height of 50 mm was adopted in all tests except for the thickest specimen. When testing the specimen with 1.4 mm nominal thickness, the accelerometer was positioned at the height of 150 mm and the input range of the spectrum analyser was set to 0.2 V. Lower heights in this case do not reveal good sensitivity of the signal obtained.

Specimens

The specimens were designed within limitations imposed by the shaker used. The frequency range of this shaker is 1.5 Hz to 3 KHz with a maximum force of 980 N. With such a force a specimen of about 30 to 40 kg can be suitably excited with an acceleration of about 2 or 3 g.

Although actual vessels are generally made of steel or metalic material, polyester (Chiba et al. (1986), Yamaki, Tani and Yamaji (1984), and Sudo et al. (1986)) or solid urethane plastic (Ross and Johns (1983), Ross, Johns and Johns (1987), Ross and Johns (1984), and Ross and MacKney (1983)) are used in the experiments. The reasons given for the use of polyester [4] are the following. First, thin-walled test cylinders with reasonably small initial imperfections can be obtained by using polyester film. Second, as the polyester film is semi-transparent, the behaviour of the contained liquid can be easily observed. The use of the solid urethane is justified by the ease of construction compared with machining for more complex shapes (Ross and MacKney, 1983).

A shematic drawing of the specimen is presented in Fig. 7. All parts of this system were made of steel. The cylindrical wall of the vessel is assembled and clamped to the base by means of 16 M5 x 15 long screws. The advantage of having the wall of the vessel clamped through screws to a thick base is that the same base can be reused with other walls. A base nut at the bottom of the base was designed to be joined to a base stud, which is connected to the head of the shaker. Taking the steel density as 7800 kg/m and the water density as 1000 kg/m, and supposing that the maximum thickness of the vessel wall is 2.6 mm, and the vessel is fully filled with water, the total mass of the system can be calculated as approximately 31 kg.

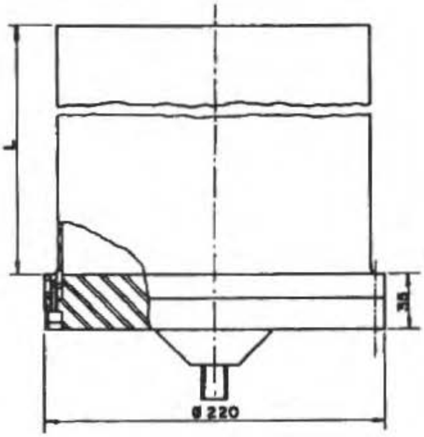

Fig. 7 Schematic drawing of the cylindrical vessel.

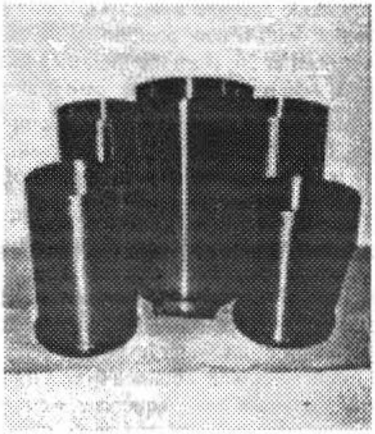

Fig. 8 General view of specimens.

The base of the cylindrical vessel was designed using a stiffness criterion. It was made rigid enough such that the lowest natural frequency is higher than approximately 3 KHz (for a completely free circular plate, Leissa (1969) presents an equation relating the eigenvalue and some parameters of the plate).

The internal diameter of the wall of the vessel was fixed at 198 mm, because it was machined from a standard mild steel pipe with an external diameter of 219.1 mm and an internal diameter of 194.1 mm) The wall thickness, though, can be changed by varying the outside diameter. A design limit of 2.6 mm was specified for the thickness and 400 mm for the wall height. A theoretical study was carried out to determine the frequencies of the empty cylindrical vessel with the limit dimensions given above. For n=1 to n=6 combined with the longitudinal beam mode, the highest frequency calculated was f=2215 Hz for n=6. The same investigation was carried out for the thickness 1.8, 1.3, 1.0 and 0.8 mm which revealed a consistent reduction of the frequencies values as the thickness was decreased.

The bolts that clamp the wall to the base were calculated as springs considering the bolt-wall as a one degree of freedom spring-mass vibration problem. The mass of the wall of the vessel for the limit dimension is 5.9 kg. The stiffness constant of a single bolt was calculated by K=EA/L where A is the cross section area and L the strained length. For a fine screw thread size 10 (Faires, 1956), the outside diameter is 4.83 mm and the minor diameter is 3.85 mm. Adopting the minor diameter for the calculation of the area and L=8mm, the frequency of the system for 16 bolts is f=4546Hz. For practical reasons M5 bolts were used. One should note that considering the occurrence of a tightening load in the bolt, one should also consider the spring constant of the connected parts which only increases the equivalent stiffness of the connection. A higher equivalent stiffness would consequently increase the frequency of the modeled system which is a safer behaviour for the purposes of the tests.

Five specimens were made and tested. To avoid appreciable variation of the thickness and external diameter, a mandrel had to be designed and used when the walls were machined externally. For this reason and also to avoid the construction of bases of different sizes, the inside diameter was kept constant and equal to 198 mm. Each of the specimens has a different nominal thickness and they were chosen as 0.6, 0.8, 1.0, 1.2 and 1.4 mm. Because these are the basic alteration from one specimen to the other, they are here referred to as specimens 0.6, 0.8, 1.0, 1.2 and 1.4. A general view of the specimens and the base is shown in Fig. 8.

A dimension survey was carried out on all five specimens. The thickness was measured at every 25 mm along the height and at eight equally spaced positions along the circumferential direction. A device made up of a dial indicator and a reference sphere supported by a rigid rod was used for these measurements. Using an inside micrometer, the internal diameter was measured at three equally spaced diametrical positions and at five heights for specimens 0.6 and 0.8 and at six heights for specimens 1.0, 1.2 and 1.4. A vernier height gage was used to measure the height of the wall at three different positions. The accuracy of all three measuring instruments used is 1/100 mm. In all cases, the total arithmethical averages were calculated and they are presented in Table 1.

Table 1. Average dimensions of specimens.

SPECIMENS	THICKNESS (mm)	INTERNAL DIAMETER (mm)	HEIGHT
0.6	0.65	197.98	280.16
0.8	0.82	197.88	325.46
1.0	0.99	197.88	398.42
1.2	1.16	197.96	397.95
1.4	1.37	197.88	398.44

Further Considerations about the Tests

Three sets of results are presented for some of the specimens tested and they may be characterised by the circumferential mode identification, longitudinal mode identification and the study of the effect of the liquid level on the frequency of the mode. In all the tests done, the investigation was limited to circumferential modes 1 to 5 combined with the longitudinal beam mode. In some cases the predicted frequency of mode 1 is well above the range where the other modes (2,3,4 and 5) occur and therefore is not considered.

Before the identification is carried out, an empty shell frequency survey is performed in the conditions specified before. This previous test facilitates the search of the frequencies.when the shaker is used. As described earlier, the mode identification requires the knowledge of amplitudes, frequency and phase provided by two accelerometers signals. The amplitude read on the oscilloscope can be altered through the amplifications on the charge amplifier and oscilloscope or adjusting the force amplitude on the shaker. For the purposes of this test, the relation between response displacement and excitation force is not useful and therefore the force amplitude of excitation is not measured. The vertical force imposed on the vessel is the sufficient force to obtain a clear signal on the oscilloscope. A calibration of the two signals is necessary before the tests starts. For the same amplification on both charge amplifiers, the accelerometers are positioned on the base of the vessel vibrating at a certain frequency and to obtain equal signals amplitudes on the oscilloscope screen, the sensitivity button of one of the charge amplifiers is adjusted.

In the identification test, at the top of the wall, one of the accelerometers (refered to as accelerometer 1) is positioned at a reference point 0 , and accelerometer 2 at a position θ_p anti clockwise viewed from the top. A signal from one accelerometer can be used as a reference, or as a input signal on the phase meter. This same signal can be connected to channel 1 or 2 of the oscilloscope.

Mode Identification Results

For specimen 0.6 and for several accelerometers position angles at different resonance frequencies, Table 2 present the amplitude ratios and the phases measured, followed by the identification of the mode. The amplitude ratio given by the amplitude Am1 on channel 1 of the oscilloscope, divided by the amplitude Am2 on channel 2 , is represented in the table by Am1/Am2.

Usually for each accelerometer position angle established, three frequencies are searched. It means that when a "suspect" frequency reveals good expected phase and amplitude ratio, two other frequencies in the vincinity are investigated to confirm the result. The third column of the tables contain the resonance frequencies measured by the frequency meter. The values of these frequencies are often lower than those measured by the transient tests and these differences are due to the smaller interference of the accelerometer mass at lower positions in the measurement carried out with the spectrum analyser.

The values of the phase measured are followed by the identifiers LE and LA which mean "lead" and "lag" of the input signal with respect to the reference signal. In the last column of the table the identification of the mode at the corresponding frequency is given by the wave number.

Some comments are necessary to facilitate the interpretation of the results given by Table 2. The expected amplitude ratio should be as closest to unity in all cases, and the phase as closest to 0 or 180 depending on the accelerometers position angle. Very often at a certain θ_p the results are obscured for various reasons. An illustration of this is given by θ_p=45 in Table 2. Due to the proximity of the accelerometers, in this case the circumferential mode 3 at frequency=353 Hz is distorted and reveals amplitude ratio and phase expected for n=4. The position angle is then changed to θ_p=90 where a closer agreement is found for the frequency=300 Hz. On the other hand, for the same reason, when using θ_p=120 to identify n=3 the frequency=305 Hz gives Am1/Am2=1.1 and phase 5.0 . The measurements are then repeated and reveal a better and consistent result for the frequency=344 Hz (353 Hz in the first measurement). In the table, (p) stands for "poor" result and (2) stands for "repeated measurements" either with the same position angle or with other angle that allows the identification of the desired mode.

Table 2. Identification of frequencies through normal displacement amplitudes and phase of specimen 0.6. (p) - poor result, (2) - repeated measurements, (*) - higher order longitudinal mode.

θ_p (degrees)	FREQUENCY MEASURED (Hz)	Am1/Am2	PHASE (degrees)	IDENTIF.
90	389	0.38	130.4 LE	-
90	524	1.0	175.0 LE	n=2
90	583	1.0	170.4 LE	n=2
90	725	0.70	17.8 LA	-
180	389	1.1	183.6 LE	-
180	524	1.0	2.9 LA	n=2*
180	583	0.98	1.8 LE	n=2
120	305	1.1	5.0 LE	-
120	353	1.0	2.0 LE	n=3
120	387	0.74	169.5 LE	-
120 (2)	304	1.3	0.0	-
120 (2)	344	1.0	2.4 LE	n=3
120 (2)	392	0.87	170.7 LE	-
45 (p)	306	0.97	180.0 LE	n=4
45 (p)	535	1.0	184.0 LE	-
90	300	0.92	3.7 LE	n=4
90	351	1.2	201.7 LE	-
90	390	1.1	119.5 LE	-
72	356	1.2	3.0 LE	-
72	387	0.99	1.3 LE	n=3
72	537	0.95	179.0 LE	n=5

Another interesting result is given by the measurements for θ_p=90 in Table 2. For two frequencies, 524 Hz and 583 Hz, the results are very similar and close to the expected. When the measurements are repeated for θ_p=180 , a consistency is observed for both frequencies. A further investigation shows that a higher longitudinal mode occurs in combination with the second circumferential mode at 524 Hz.

Water Height Versus Frequencies and Longitudinal Displacements Measurements

In order to confirm the occurrence of the beam mode in combination with the several circumferential modes identified, the results of the longitudinal displacements measurements for specimen 0.8 are shown in Fig. 9. These results are presented in terms of normalised values W and Y defined by W=Wb/Wt and Z=Zb/L, where W=normal displacement ratio Z=distance from the base ratio, L=longitudinal length of specimen, Zb=longitudinal distance from the base ratio, L=longitudinal length of specimen, Zb=longitudinal distance from the base, Wt=normal displacement measured at the top of the specimen, Wb=normal displacement measured at the position Zb.

Measurements were performed at every 25 mm starting from the top. Using a accelerometer the excitation force at the investigated frequency was adjusted to give a wave signal which fills completely the oscilloscope screen for the displacement Wt. The results shown in Fig. 9 confirm the expected longitudinal vibration mode.

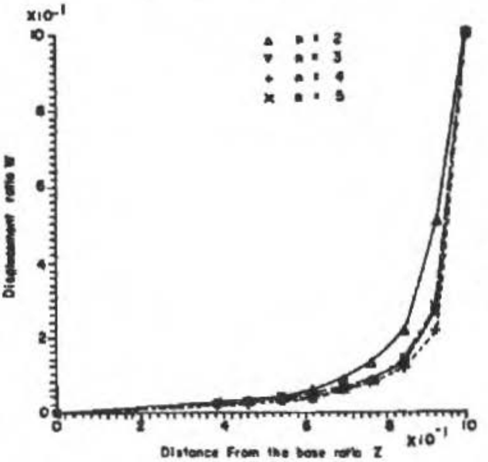

Fig. 9 Displacement versus distance from the base for specimen 0.8 and circumferential modes 2, 3, 4 and 5.

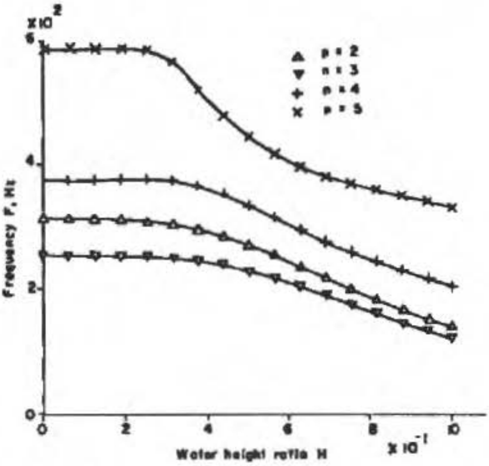

Fig. 10 Natural frequencies of several circumferentail modes versus water height for specimen 1.0.

Natural frequencies were plotted against H which is defined by H=Z/L where H=water height ratio, Z=height of water level in specimen. Fig. 10 shows these results for specimens 1.0. A general observed behavior for all investigated circumferential modes, is that there is a certain height of water level up to which the frequency remains indifferent. Further increases of water height from this point produces a decrease in frequency. For the studied geometries, the circumferential wave number 5 occur at higher frequencies than wave numbers 2, 3 and 4. There seems to be no preferential circumferential wave number related with the lowest frequency although n=2, 3 and 4 dispute this position. For specimen 0.6, the lowest frequency occurs for n=3 and for specimens 1.0 and 1.2 the lowest frequencies are related with n=2.

An interesting evolution is observed for specimens 1.0, 1.2 and 1.4. These specimens have practically the same longitudinal lenght and are differentiated only by the thickness. As the thickness increases from specimen 1.0 to 1.4, wave numbers 2 and 3 tend to swap positions. For specimen 1.0, n=2 has the lowest frequency. For specimen 1.2 the frequency of n=2 tend to increase and get closer to n=3 and finally for specimen 1.4, the measured experimental frequencies are practically coincident for n=2 and n=3.

Discussion and Conclusions

The vibrational tests in this work had the objective of verifying the theorical model presented previously (Menezes and Mistry, 1991 a, b, c). Theoretical natural frequencies were compared to the experimental values in 11 different conditions with an average ratio (theoretical frequency/experimental frequency) ft/f=0.951 and a maximum deviation of 20% (Menezes and Mistry, 1991 b, c). These comparisons represent the main confirmation of the effectiveness of the theoretical model employed.

Altinisik, Karadeniz and Servern (1981), reported two series of experimental tests: one on thin cylinders containing water, and the other on an idealised arch dam and reservoir. Comparison between experimental and calculated frequencies resulted in 25-35% superiority of the theoretical frequencies for the ferrocement cylindrical dam. Two of the reasons given to explain the differences were as follows: 1) It is difficult to produce built-in boundary conditions in the model, 2) The determination of the true effective thickness of the model is not easy for such a thin section and small errors have major consequences.

The theoretical model employed to compare with the experimental tests disregards geometrical imperfections of the thickness variation and departure from circularity. Both of these are known to lead to significant errors in buckling predictions of thin axisymmetrical shell structures (Kollar and Dulacska, 1984). The buckling and natural frequencies of these structures are in fact representation of their elastic stability. It is not surprising that results should show a certain degree of sensitivity.

The dimensions survey of the specimens reveals certain differences between the specified dimensions and the ones actually obtained after manufacture. Internal diameters were obtained within variable measured tolerances from a maximum of 1.55 mm for specimen 1.0 to a minimum of 0.45 mm for specimen 1.2. However, the maximum difference between the average measured diameter and the nominal diameter was 0.12 mm. This represents an error of only 0.061%, taking the nominal internal diameter as a reference. Greater deviations occurred for specimen 0.6 which resulted whith a average measured thickiness of 0-65 mm. The tolerance measured for this same specimen was the smallest and equal to 0.07 mm. The greatest difference between the maximum and minimum measured thicknesses was 0.27 mm for specimen 1.2. It is apparent that the longer specimens are liable to greater differences between the maximum and minimum thicknesses measured due to the greater possibility of deflections and machine tool wear during the construction process.

The vertical excitation of the specimens constitutes a procedure which has the main advantage of avoiding the construction or possession of an horizontal shaking table. This alternative is no doubt, a very economical one. On the other hand, it also has proved efficient in the sense that all circumferential modes can be clearly excited.

A procedure of identification of vibrational shape modes using accelerometers was introduced in the experiments. One can conclude that the major advantage of this technique is the simplicity of the equipment used and the exemption of auxiliary support devices. In the test of specimens made of steel, or any other rigid material, the main difficulty is the excitation of the displacements large enough to display a measurable vibrational mode profile. The use of plastic materials and large excitation forces is probably the easiest way of overcoming this problem. Experimental investigation of more rigid structures would undoubtedly require an extremely accurate construction and supports for the sensors precise enough to make the variation of the displacement perceptible. As discussed before, mass of the accelerometer works as a stimulus of the anti-nodes, but perhaps due to intrinsic construction imperfections, circumferential mode configurations may in general cases remain constant along the circumferential direction, and therefore non-contacting sensor might be applicable. This is said because for a perfect circumferential geometry, the circumferential nodes or anti-nodes are likely to occur at any point and at any time. The logic of the use of non-contacting sensors would be that for two predictable positions, the measured amplitudes should be the same.

References

Altinisik, D., Karadeniz, H. and Servern, R.T., 1981, "Thoeretical and Experimental Studies on Dynamic Structure-Fluid Coupling", Proc. Instn. Civ. Engrs., Vol. 71, Part 2, pp. 675-704.

Chiba, M., Tani, J., Hashimoto, H. and Subo, S., 1986, "Dynamic Stability of Liquid-Filled Cylindrical Shells under Horizontal Excitation, Part I: Experiment", J. of Sound and Vibration, Vol. 104, Nº 2, pp. 301-319.

Ewins, D. J., 1985, "Modal Testing: Theory and Practice", Research Studies Press Ltd., Letchworth, Herts, England.

Faires, V. M., 1955, "Design of Machine Elements", The MacMillian Company, N.Y.

Kollar, L. and Dulacska, E., 1984, "Buckling of Shells for Engineers", John Wiley & Sons, 1984.

Leissa, A. W., 1969, "Vibration of Plates", NASA SP-160, National Aeronautics and Space Administration, Washington, DC, 1969.

Menezes, J. C. and Mistry, J., 1991 a, "Time Domain Numerical Solution of Shell-Fluid Coupled Equations", XI ABCM Mechanical Engineering Conference - São Paulo, SP, Brazil.

Menezes, J. C. and Mistry, J., 1991 b, "Dynamic Characteristics of Circular Cylindrical Shells Containig Fluid", XI ABCM Mechanical Engineering Conference - São Paulo, SP, Brazil.

Menezes, J. C. and Mistry, J., 1991 c, "Vibration of Thin Cylindrical Vessels Containig Fluid", RBCM - J. of Braz. Soc. Mech. Sc., Vol. XIII, Nº 1, pp. 73-88.

Ross, C. T. F. and Johns, T., 1983, "Vibration of Submerged Hemi-Ellipsoidal Domes", J. Sound and Vib., Vol. 91, Nº 3, pp. 363-373.

Ross, C. T. F. and Mackney M.D.A., 1983, "Deformation and Stability Studies of Thin-Walled Domes Under Uniform External Pressure", J. Strain Analysis, Vol. 18, No. 3, pp 167-172.

Ross, C. T. F. and Johns, T., 1986, "Vibration of Hemi-Ellipsoidal Axisymetric Domes Submerged in Water", Proc. Inst. Mech. Engrs., Vol. 200, Nº C6, pp. 389-398.

Ross, C. T. F., Johns, E. and Johns, T., 1987, "Vibration of Thin-Walled Domes Under External Water Pressure", J. Sound and Vib., Vol. 114, Nº 3, pp. 453-463.

Sudo, S., Hashimoto, H., Tani, J. and Chiba, M., 1986, "Dynamic Behavior of a Liquid in a Cylindrical Container", Bulletin of JSME, Vol. 29, Nº 254.

Yamaki, N., Tani, J. and Yamaji, T., 1984, "Free Vibration of a Clamped Circular Cylindrical Shell Partially Filled with Liquid", Journal of Sound and Vibration, Vol. 94, Nº 4, pp. 531-550.

RBCM - J. of the Braz. Soc. Mechanical Sciences
Vol. XV - nº 1 - 1993 - pp. 42-53

ISSN 0100-7386
Printed in Brazil

Modal Parameters Identification Techniques for Supporting Structure in Rotating Machinery Vibrations

Franco Giuseppe Dedini
UNICAMP - Departamento de Projeto Mecânico
Caixa Postal 6051 - CEP 13081-970 Campinas SP

Federico Cheli
Politecnico di Milano- Dipartimento di Meccanica
Sezione Meccanica dei Sistemi - 3º piano
CAP 20133 Milano Italia

Abstract

The frequency response of a rotating machine can be significantly affected by the dynamic behaviour of the supporting structure. This paper presents an experimental verification of two identification methods based on the comparison between the experimental frequency response measured at the journal bearings and the theoretical values obtained through a mathematical model of the system. In this case, an inaccurate evaluation of the bearings stiffness and damping coefficients can significantly affect the theoretical frequency response of the rotor. So, the oil film forces at the bearings were measured and compared with those obtained using the equivalent stiffness and damping coefficients analytically evaluated and the experimental displacement data at the bearings.

Keywords: Identification, Foundation, Bearings, Oil film, Frequency response

Introduction

The frequency response of a rotating machine can be significantly affected by the dynamic behaviour of the supporting structure. In order to study the interactions between rotating machinery and supporting structures several mathematical techniques based on the evaluation of the foundation mechanical impedance matrix can be used (Diana et al., 1985) and (Diana et al., 1988). Each term of the mechanical impedance matrix can be described as a function of the foundation modal parameters as well as of the machine rotational speed. However, only in a few cases the experimental frequency response of the foundation structure alone, due to a known exciting force, can be measured. Therefore, usual modal analysis techniques are often unusable for these investigations. As rotor and support vibration data can be easily collected by computerized monitoring systems during run-ups and run-downs, a methodology for evaluating the foundation modal parameters by minimizing some objective functions based on the rotating machine frequency response has been developed. This approach for identifying the foundation parameters as well as some mathematical models were illustrated by the authors in a previous paper (Diana et al., 1988).

These techniques require the comparison between the experimental frequency responses measured at journal bearings and the theoretical ones obtained with a mathematical model in which the dynamic behaviour of the rotor, the bearings and the foundation structure is investigated (Diana, 1986).

In order to prove the capability of the foundation modal parameters identification techniques a case study was investigated. The dynamic behaviour of a motor driven rotor supported on two lubricated bearings, whose housing were assembled to a flexible foundation structure, was analysed (Lalanne et al., 1990).

As an inaccurate evaluation of the bearings stiffness and viscous damping terms can significantly affect the theoretical frequency response of the rotor, the oil-film forces at the journal bearings were measured in the horizontal and vertical directions. Experimental oil-film forces data were compared with those obtained using the bearing dynamic parameters and experimental vibration data of the rotor (Weber et al., 1992).

Manuscript received March 1993. Associate Technical Editor: Agenor de Toledo Fleury

The frequency response of the foundation structure alone was measured and a usual modal analysis of the system was carried out. Then, the foundation modal parameters identification techniques herein described were applied using rotor and supports vibration data measured during run-ups. A comparison between analytical and experimental frequency response of the rotor is shown.

Frequency Response of the Rotor

Let us consider the structure composed of the shaft and the bearings. The motion equations can be expressed in the form:

$$[M]\ddot{\underline{X}} + [R]\dot{\underline{X}} + [K]\underline{X} = \underline{F} \tag{1}$$

where $\underline{X}$ is a vector that contains the rotor displacement $\underline{X}_r$ and the support displacement $\underline{X}_c$. The vector $\underline{F}$ contains the forces $\underline{F}_r$ acting to the rotor and oil-film forces $\underline{F}_c$ acting at the connecting points between rotor and foundation. Equation (1) then becomes:

$$\begin{aligned}
&[M_{rr}]\ddot{\underline{X}}_r + [R_{rr}]\dot{\underline{X}}_r + [R_{rc}]\dot{\underline{X}}_c + [K_{rr}]\underline{X}_r + [K_{rc}]\underline{X}_c = \underline{F}_r \\
&[R_{cr}]\dot{\underline{X}}_r + [R_{cc}]\dot{\underline{X}}_c + [K_{cr}]\underline{X}_r + [K_{cc}]\underline{X}_c = \underline{F}_c
\end{aligned} \tag{2}$$

The oil-film forces can be written in terms of relative vibrations $\underline{X}_{rc}$ between rotor and support as:

$$\underline{F}_c = [R_o]\dot{\underline{X}}_{rc} + [K_o]\underline{X}_{rc} \tag{3}$$

where the matrices $[K_o]$ and $[R_o]$ contain the stiffness and viscous damping terms of the bearings calculated by a linear approach (Pinkus and Sternlicht, 1961; Orcutt and Arwas, 1966).

The foundation structure frequency response can be described in terms of modal coordinates $\underline{q}$ which are related to the support displacement $\underline{X}_c$ by the following expression:

$$\underline{X}_c = [A]\underline{q} \tag{4}$$

The columns of the matrix [A] are composed of the components of the foundation normal modes $\underline{\Phi}_i$. The motions equations of the supporting structure can be written in the form:

$$[m]\ddot{\underline{q}} + [r]\dot{\underline{q}} + [k]\underline{q} = -[A]^T\underline{F}_c \tag{5}$$

The matrices [m], [r] and [k] contain the foundation modal parameter $\underline{p}$, that are the generalized mass m_i, the damping factor r_i and the generalized stiffness k_i. Let us consider the independent variables $\underline{Z}$:

$$\underline{Z}^T = \{\underline{X}_r^T, \underline{q}^T\} \tag{6}$$

Equation (1) can be written:

$$[M^*]\ddot{\underline{Z}} + [R^*]\dot{\underline{Z}} + [K^*]\underline{Z} = \underline{F}^* \tag{7}$$

where:

$$[M^*] = \begin{bmatrix} [M_{rr}] & [0] \\ [0] & [m] \end{bmatrix}$$

$$[R^*] = \begin{bmatrix} [R_{rr}] & [R_{rc}]\,[A] \\ [A]^T[R_{cr}] & [r] + [A]^T[R_{cc}]\,[A] \end{bmatrix}$$

$$[K^*] = \begin{bmatrix} [K_{rr}] & [K_{rc}]\,[A] \\ [A]^T[K_{cr}] & [k] + [A]^T[K_{cc}]\,[A] \end{bmatrix}$$

$$\underline{F}^{*\,T} = \{\underline{F}^T,0\} \tag{8}$$

In the case of harmonic forces $\underline{F}_r$ acting to the rotor we obtain:

$$\underline{F}_r = \underline{F}_{ro}e^{i\Omega t} \quad \underline{q} = \underline{q}_o e^{i\Omega t} \quad \underline{X}_r = \underline{X}_{ro}e^{i\Omega t} \tag{9}$$

Therefore eq. (7) becomes:

$$[H_{rr}]\underline{X}_{ro} + [H_{rc}]\underline{q}_o = \underline{F}_{ro}$$

$$[H_{cr}]\underline{X}_{ro} + ([H_{cc}] + [G(\Omega,\underline{p})])\underline{q}_o = 0 \tag{10}$$

where:

$$[H_{rr}] = -\Omega^2[M_{rr}] + i\Omega[R_{rr}] + [K_{rr}]$$

$$[H_{rc}] = i\Omega[R_{rc}]\,[A] + [K_{rc}]\,[A]$$

$$[H_{cr}] = i\Omega[A]^T[R_{cr}] + [A]^T[K_{cr}]$$

$$[H_{cc}] = i\Omega[A]^T[R_{cc}]\,[A] + [A]^T[K_{cc}]\,[A] \tag{11}$$

The matrix $[G(\Omega,\underline{p})]$ depends on both the machine rotational speed Ω and on the foundation modal parameters $\underline{p}$ (Diana et al., 1988). The mechanical impedance matrix [B] of the foundation structure can be expressed as:

$$[B(\Omega,p)]\underline{X}_{co} = -\underline{F}_{co} \tag{12}$$

If the number of normal modes $\underline{\Phi}$ is equal to the number of degrees of freedom $\underline{X}_c$, [A] is a square matrix and the matrix [B] can be written in the form:

$$[B(\Omega,\underline{p})] = [A]^{-T}[G(\Omega,\underline{p})]\,[A]^{-1} \tag{13}$$

The foundation modal parameters can be calculated using parameter identification techniques, if rotor and supports frequency responses have been measured, or using modal analysis algorithms, if the experimental transfer functions of the supporting structure alone are available. Substituting the matrices [m], [r] and [k] in the matrices $[\underline{M}]$, $[\underline{R}\}$ and $[\underline{K}]$, eq. (7) can be solved. Therefore, the theoretical frequency response of both the rotor and the supports can be calculated, in the time domain, for any system of external forces acting to the rotor. Moreover, using the foundation modal parameters, the matrix [G] can be calculated for any rotational speed of interest. Therefore, solving eq. (10) in the frequency domain, the response of the rotor due to harmonic forces can be calculated.

Modal Parameter Identification Techniques

The unknown terms of eq. (10) are the supporting structure modal parameters $\underline{p}$ contained in the matrices [m], [r] and [k]. They can be calculated using numerical methods that minimize some objective functions on both experimental and theoretical rotor and supports vibration data.

Method I

Let us indicate with $\underline{F}^u_{co}$ the forces transmitted from the rotor-bearings system to the foundation at the connecting points. Considering eqs. (10) and (4), the forces $\underline{F}^u_{co}$ can be written in the following form:

$$\underline{F}^u_{co}(\Omega, \underline{F}_{ro}, \underline{X}_{co}) = \underline{F}^l_{co}(\Omega, \underline{p}, \underline{X}_{co}) \tag{14}$$

Let us indicate with $\underline{F}^l_{co}$ the forces transmitted from the foundation to the rotor-bearings system. These forces can be written as:

$$\begin{aligned} \underline{F}^u_{co} &= (-[H_{cr}(\Omega)]\,[H_{rr}(\Omega)]^{-1}[H_{rc}(\Omega)]\,[A]^{-1})\,\underline{X}_{co} + \\ &+ ([H_{cr}(\Omega)]\,[H_{rr}(\Omega)]^{-1})\,\underline{F}_{ro} + ([H_{cc}(\Omega)]\,[A]^{-1})\,\underline{X}_{co} \end{aligned} \tag{15}$$

Moreover, the forces $\underline{F}^u_{co}$ and $\underline{F}^l_{co}$ must satisfy the following relationship:

$$\underline{F}^l_{co} = -([G(\Omega, \underline{p})]\,[A]^{-1})\,\underline{X}_{co} \tag{16}$$

The forces $\underline{F}^u_{co}$ can be calculated using the experimental vibrations $\underline{X}_{co}$ of the supports due to the external forces $\underline{F}^o_{ro}$ acting on the rotor. Therefore, it is possible to calculate $\underline{F}^u_{co}(\Omega, \underline{F}^o_{ro}, \underline{X}^o_{co})$ and $\underline{F}^l_{co}(\Omega, \underline{p}, \underline{X}^o_{co})$, as function of the unknown quantities $\underline{p}$, using an iterative method. The objective function that must be minimized is:

$$f_1 = \sum_{\Omega}\sum_{k} (F^u_{cok}(\Omega, \underline{F}_{ro}, \underline{X}^o_{co}) - F^l_{cok}(\Omega, \underline{p}, \underline{X}^o_{co}))^2 \tag{17}$$

where F^u_{cok} and F^l_{cok} are the forces calculated at the k-th support of the shaft at the machine rotational speed Ω. It is important to underline that as the matrix [A] must be inverted, the number of normal modes of the supporting structure must be equal to the number of degrees of freedom associated to the connecting nodes of the model.

Method II

The oil-film forces, that is, the forces $\underline{F}_c$ at the connecting nodes, can be calculated substituting the experimental vibration data $\underline{X}_{ro}$ into eq. (3). In the case of an harmonic excitation we have:

$$\underline{F}_{co} = (i\Omega[R_o] + [K_o])\,\underline{X}^o_{rco} \tag{18}$$

The motion of the foundation structure can be expressed in terms of the modal coordinates $\underline{q}$ in the following form:

$$(-\Omega^2[m] + i\Omega[r] + [k])\,\underline{q}_o = -[A]^T(i\Omega[R_o] + [K_o])\,\underline{X}^o_{rco} \tag{19}$$

A first estimate of $\underline{p}$ is assigned. Using eq. (19), the modal co-ordinates $\underline{q}_o$ are calculated; then, substituting $\underline{q}_o$ into eq. (4) the support displacement $\underline{X}_{co}$ are evaluated. The objective function is the difference between the experimental displacement $\underline{X}^o_{cok}(\Omega)$ and the theoretical ones $\underline{X}^o_{cok}(\Omega, \underline{X}^o_{rco}, \underline{p})$, both evaluated at the k-th connecting point:

$$f_{11} = \sum_{\Omega}\sum_{k} \left(X^{o}_{cok}(\Omega) - X^{o}_{cok}(\Omega, \underline{p}, \underline{X}^{o}_{rco})\right)^{2} \qquad (20)$$

This method has no restriction about the number of foundation normal modes to take into account and does not require the knowledge of the external forces $\underline{F}_{ro}$ applied to the rotor.

Experimental Set-up

The experimental set-up is composed of a motor driven rotor, supported by two lubricated journal bearings which are linked to a rigid base plate. On the rigid base plate there are vertical and horizontal uncoupled force transducers fixed at the connecting points between the base plate and the bearing housing in order to measure the oil film forces. The whole system can be connected to four springs or rigid spacers (Fig. 1).

The relative displacement between the rotor and the bearings were measured by a couple of proximity probes located at each bearing in vertical and horizontal directions. Furthermore, a couple of proximity probes were placed at the middle span of the rotor. The absolute vibrations at each support were measured by a couple of accelerometers placed in vertical and horizontal directions. the rotational speed was evaluated by a proximity probe. The sketch of the rotor and the probe positions is shown in Fig. 2.

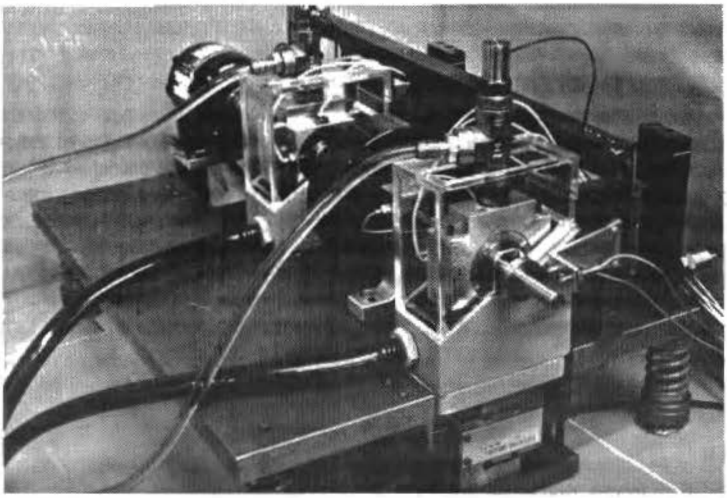

Fig. 1 Experimental set-up

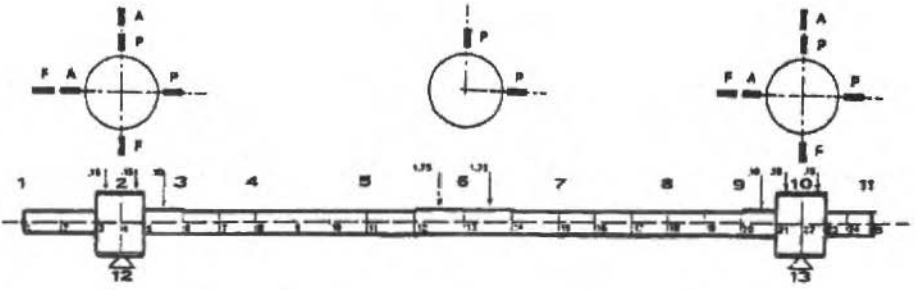

Fig. 2 Finite element model of the rotor and probes location
(P: proximity probes, A: accelerometers, F: force transducers).

Experimental Results

At first, the rotor foundation plate was supported from rigid spacers. A start-up was carried out and the rotor was brought up to 3600 r/min. The Bode plot of the absolute vibrations of the rotor; synchronous with the rotational speed (1X), measured at bearing 2 in the horizontal and vertical directions, are shown in Figs. 3 and 4. This configuration of the foundation structure proved to be rigid over the whole speed range from 150 r/min to 3600 r/min. After replacing the spacers by springs, the rotor was started again. The 1X absolute vibrations of the rotor measured at bearing 2 in the horizontal and vertical directions are shown in Figs. 3 and 4 respectively. The comparison between the frequency response curves shown in Figs. 3 and 4 exhibits the dynamic effects due to the flexible foundation structure on the rotor vibrational behaviour.

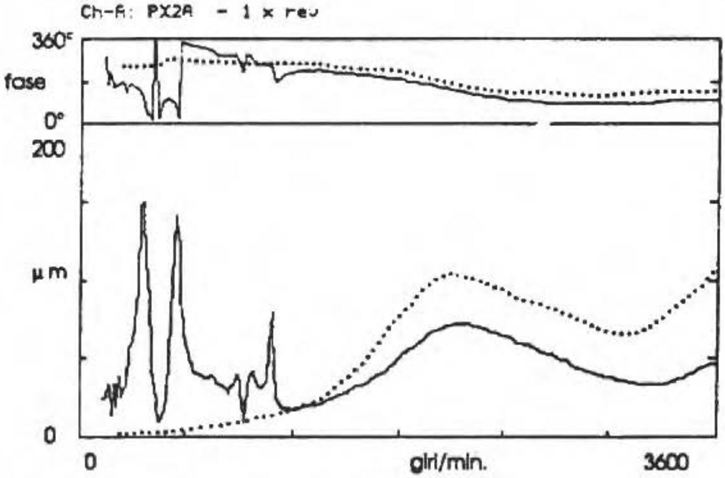

Fig. 3 Experimental absolute vibrations (1X) of the rotor at bearing 2 in the horizontal direction. Rigid foundation (dotted line), flexible foundation (solid line)

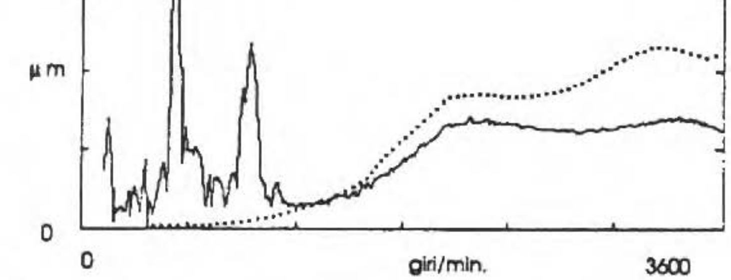

Fig. 4 Experimental absolute vibrations (1X) of the rotor at bearing 2 in the vertical direction. Rigid foundation (dotted line), flexible foundation (solid line).

In order to evaluate the stiffness and the viscous damping coefficients of the oil-film, fluid-film forces in the horizontal and vertical directions were evaluated substituting the experimental 1X vibration data, collected during a rotor start-up, into eq. (3). In Fig. 5, the Bode plot of the 1X harmonic component of the fluid-film vertical force calculated at bearing 2 is shown. In the same figure, the amplitude and phase curves of the 1X force vector measured at bearing 2 in the vertical direction is reported. In Fig. 6, the theoretical and experimental rotor displacement locus inside bearing 2 is shown. The comparison between theoretical results and experimental data prove the effectiveness of the bearing mathematical model for evaluating the fluid-film forces.

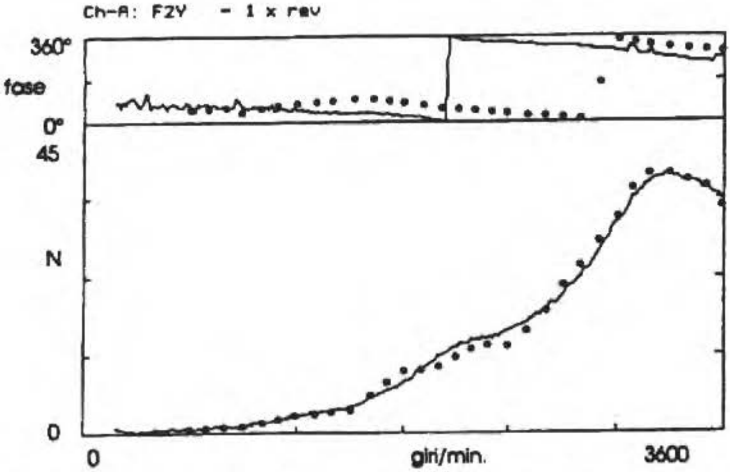

Fig. 5 Synchronous component of the oil-film force in the vertical direction at bearing 2. Experimental data (solid line), theoretical data (dotted line).

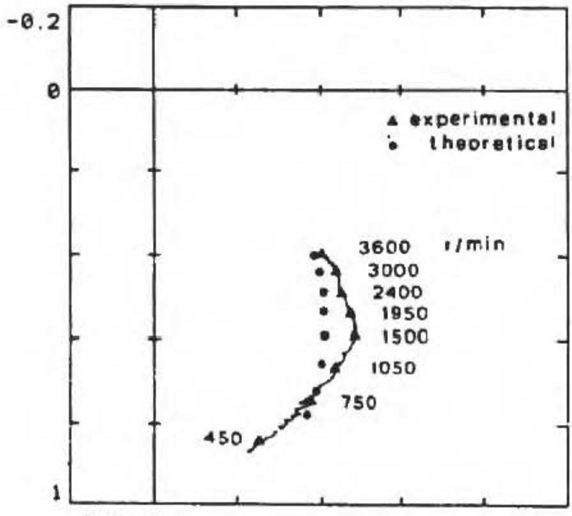

Fig. 6 Theoretical and experimental rotor displacement locus inside bearing 2.

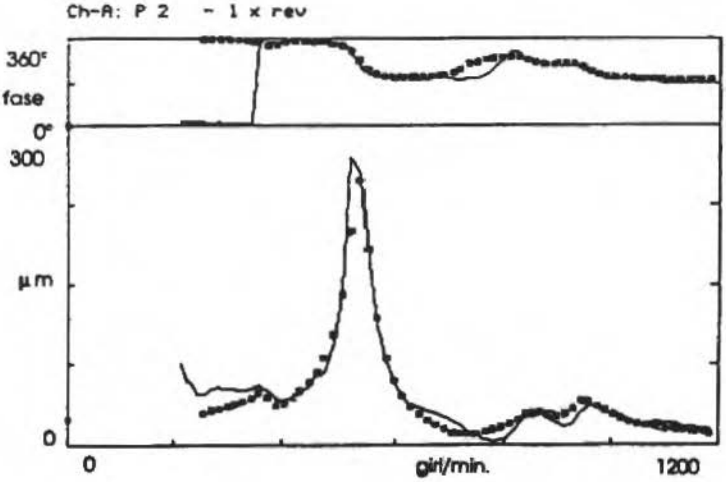

Fig. 7 Bode plot of the analytical and experimental transfer function evaluated at bearing 2 in vertical direction.

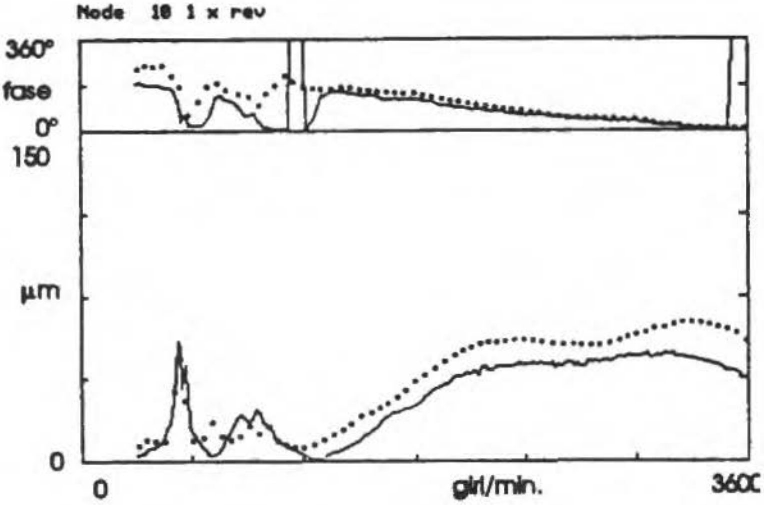

Fig. 8 Theoretical and experimental (dotted line) 1X vibrations measured at bearing 2 in vertical direction. Modal parameters evaluated with modal analysis techniques applied to experimental transfer functions.

Subsequently, a modal analysis of the rotor supporting structure was carried out. A harmonic force was applied at bearing 1 in the vertical direction. The foundation transfer functions at sixteen measurement locations, which included the rotor supports, were colleted over a frequency range from 2 Hz to 60 Hz. The modal parameters are summarized in Table 1. In order to evaluate the accuracy of the mode parameters evaluation, analytical transfer functions were generated using a synthesis operation. In Fig. 7 the Bode plot of the analytical and experimental transfer functions evaluated at bearing 2 in the vertical direction are shown.

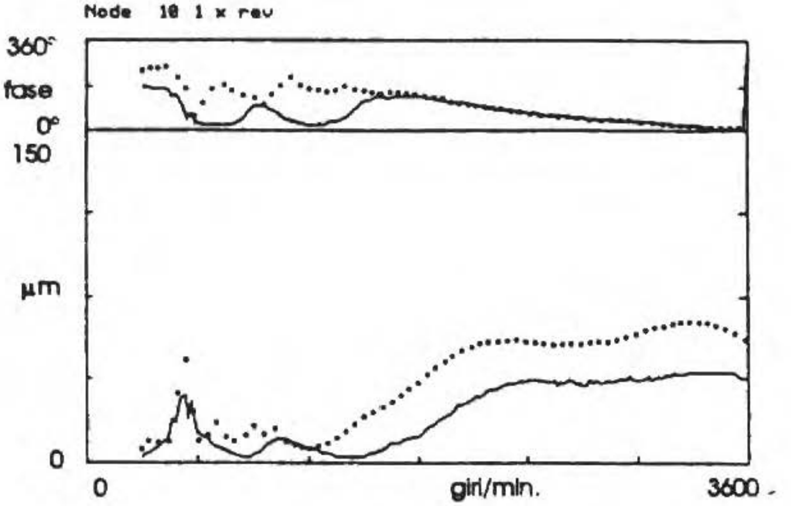

Fig. 9 Theoretical (solid line) and experimental (dotted line) 1X vibrations measured at bearing 2 in the vertical direction. Modal parameters evaluated with the identification method I.

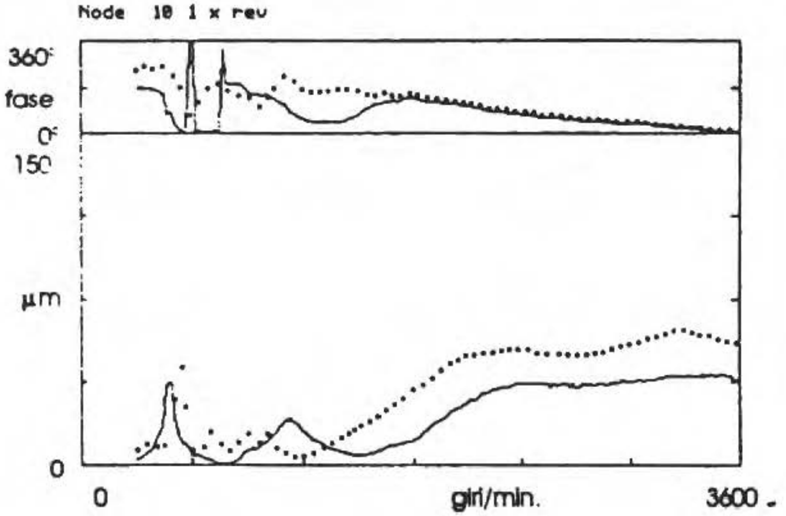

Fig. 10 Theoretical (solid line) and experimental (dotted line) 1X vibrations measured at bearing 2 in the vertical direction. Modal parameters evaluated with the identification method II.

The 1X frequency response of the rotor due to an imbalance mass applied to the disk fixed to the rotor was calculated. These vibration data were used to evaluate the foundation modal parameters by the above mentioned identification methods. The results of these analyses are summarized in Table 2 and 3. As the method I requires that the number of normal modes of the supporting structure to be equal to the number of degrees of freedom associated with the connecting nodes of the model, only four natural frequencies were identified.

Table 1 Rotor foundation structure modal parameters

Modal Parameters	Mode Number				
	1	2	3	4	5
Natural Frequency (Hz)	6.3	9.0	12.8	14.2	15.7
Damping Ratio	0.051	0.034	0.053	0.061	0.034
Generalized Mass	1.743	1.245	1.663	2.286	1.472
Generalized Stiffness	2688	3981	10756	18197	14324

Table 2 Rotor foundation structure modal parameters - method I

Modal Parameters	Mode Number			
	1	2	3	4
Natural Frequency (Hz)	6.5	8.9	16.0	17.0
Damping Ratio	0.137	0.078	0.133	0.089
Generalized Mass	2.334	3.117	3.170	4.365
Generalized Stiffness	3906	9797	35349	50068

Table 3 Rotor foundation structure modal parameters - method II

Modal Parameters	Mode Number				
	1	2	3	4	5
Natural Frequency (Hz)	7.8	9.0	14.3	15.8	19.0
Damping Ratio	0.194	0.040	0.163	0.026	0.061
Generalized Mass	4.989	4.994	4.950	4.069	9.140
Generalized Stiffness	12108	12485	39934	40203	130084

Then, the foundation modal parameters were used to calculate the rotor frequency response. At first, the modal parameters reported in Table 1, evaluated with an usual modal analysis, carried out on foundation basis transfer functions, were considered. In Fig. 8, the comparison between theoretical and experimental 1X vibrations measured at bearing 2 in the vertical direction is shown. The comparison between the experimental 1X vibrations measured at bearing 2, in the vertical direction, and the theoretical one obtained using the modal parameters identified with methods I and II is shown in Fig. 9 and 10, respectively. Finally, a finite element model of the foundation structure was developed. The comparison between the experimental 1X vibrations measured at bearing 2, in the vertical direction, and the theoretical one obtained using these modal parameters is shown in Fig. 11.

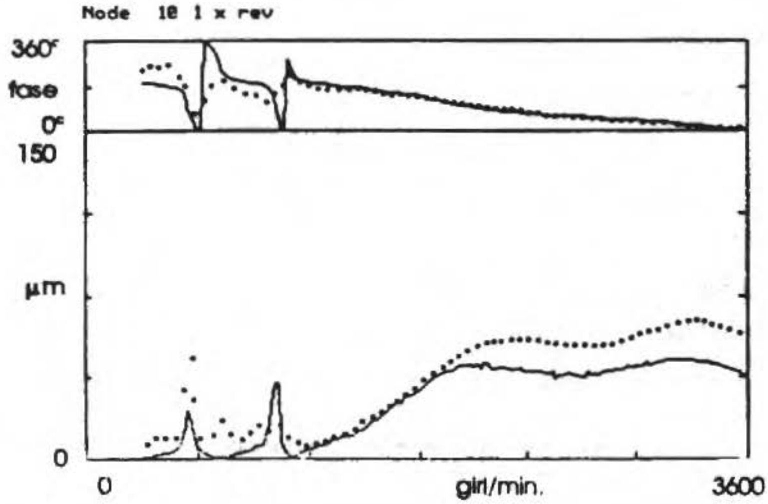

Fig. 11 Theoretical (solid line) and experimental (dotted line) 1X vibrations measured at bearing 2 in the vertical direction. Modal parameters evaluated with modal analysis techniques applied to analytical transfer functions.

Conclusions

The theoretical frequency responses obtained by using the modal parameters identified with the different techniques fit the experimental vibration data with sufficient accuracy.

The parameter identification methods described in this paper proved to be able to evaluate the modal parameters of rotating machinery foundations, using rotor and supports vibration data. These techniques can be very useful when only the frequency response of the foundation structure is not available. The capability of the methods is influenced by the accuracy of the initial estimate of the foundation normal modes.

Nomenclature

[A] = modal matrix

$[B(\Omega,\underline{p})]$ = mechanical impedance matrix of the foundation

$\underline{F}_c$ = forces transmitted between rotor and foundation at the connecting points

$\underline{F}_r$ = external forces applied on the rotor

[k] = modal stiffness matrix of the foundation

[K] = stiffness matrix of the system

[K*] = stiffness matrix of the system in hybrid coordinates

[m] = modal mass matrix of the foundation

[M] = mass matrix of the system

[M*] = mass matrix of the system in hybrid coordinates

p = vector of the modal parameters of mass, stiffness and damping

q = modal coordinates

[r] = modal damping matrix of the foundation

[R] = damping matrix of the system

[R*] = damping matrix of the system in hybrid coordinates

$\underline{X}_c$ = coordinates of the foundation at the connecting points with the rotor

$\underline{X}_r$ = coordinates of the rotor

$\underline{X}_{rc}$ = relative coordinates at the connecting points with the rotor and the foundation

$\underline{Z}$ = vector of the hybrid coordinates

Ω = excitation frequency

Method II does not need the knowledge of the external forces applied to the rotor and that the number of normal modes be equal to the number of degrees of freedom associated with the connecting points.

Acknowledgements

Support of M.P.I. (M.U.R.S.T.), C.N.R. (Consiglio Nazionale delle Ricerche) and CAPES (Brazil) is gratefully acknowledged.

References

Diana, G.; Cheli, F.; Curami, A.; Vania, A., 1985, "On the modal analysis to define mechanical impedance of a foundation". ASME, Cincinnati.

Diana, G., 1986, P.A.L.L.A.: "A package to analyse the dynamic behaviour of a rotor-supporting structure system". CISM Rotordynamics Conf., Udine, Italy.

Diana, G.; Cheli, F.; Vania, A., 1988, "A method to identify the foundation modal parameters through measurements of the rotor vibrations". IMechE Vibration in Rotating Machinery International Conference, Edinburgh.

Lalanne, M. and Ferraris, G., 1990, "Rotordynamics - Prediction in Engineering", John Wiley & Sons. England.

Orcutt, F.K.; Arwas, E.B., 1966, "The steady-state and dynamic characteristics of a full circular bearing and a partial arc bearing in the laminar and turbulent flow regimes". ASME Paper 66- LubS 4, Lubrification Symposium, New Orleans.

Pinkus, O.; Sternlicht, B., 1961, "Theory of hydrodynamic lubrication". Mc Graw-Hill Book Co.

Weber, D.; Cardinali, R. and Nordmann, R., 1992, "A Contribution to the dynamic simulation of nonlinear rotating machines with fluid dynamicaal coupling elements". Rotordynamics '92, pp. 389-397, Venice, Italy.

RBCM - J. of the Braz. Soc. Mechanical Sciences
Vol. XV - nº 1 - 1993 - pp. 54-64

ISSN 0100-7386
Printed in Brazil

High Temperature Lifetime Prediction in Metallic Materials Subjected to Cyclic Loadings

Pedro Manuel Calas Lopes Pacheco
Depto. de Engenharia Mecânica
Centro Federal de Ensino Tecnológico/RJ
Av. Maracanã, 229 - Maracanã
20453-900, Rio de Janeiro, RJ

Federico Pablo Hubscher
Heraldo da Costa Mattos
Depto. de Engenharia Mecânica
Pontifícia Universidade Católica do Rio de Janeiro
Rua Marquês de São Vicente, 225 - Gávea
22453-900, Rio de Janeiro, RJ

Abstract

The present paper is concerned with the high temperature lifetime prediction in metallic materials. It is proposed an elasto-viscoplastic constitutive model, developed within the framework of Continuous Damage Mechanics, that takes into account the coupling between the creep and low-cycle fatigue mechanism. The basic features of this model are shown by simulating a stainless steel bar subjected to cyclic loadings at different temperatures. The applicability and the usefulness of the theory are verified by means of examples concerning the lifetime prediction of a stainless steel pipe at 600ºC under complex pressure loadings.

Keywords: High Temperature Lifetime Prediction, Continuous Damage Mechanics, Creep, Fatigue, Mettalic Materials

Introduction

Prediction of lifetimes under complex loadings and environment constitutes an important but difficult step of the design of metallic components working at high temperature since it is necessary to take into account the viscoplastic behaviour as well as crack initiation under creep and fatigue condition.

Low cycle fatigue, or plastic oligocyclic fatigue, is considered when the plastic strain involved is big enough to be measured. This corresponds to stresses higher than the yield stress and, in general, to less than 10000 cycles to failure. In metals the fatigue damage is mainly in the form of micro-cracks which are transgranular.

Creep damage occurs in metals mainly during tertiary creep at temperatures above 1/3 of the absolute melting temperature. In this case, viscoplasticity induces important time dependent phenomena. Monotonic or cyclic loadings first induce the accumulation of dislocations at the points between crystals leading to microcavities and then intergranular micro-cracks and micro-voids on grain boundaries or at the junction of several cristals. These micro-cavities may grow as a function of time even if the stress remains constant.

The prediction of the failure of a mechanical component is generally made through parametric equations, relating lifetime to some stabilized cyclic quantities such as elastic or inelastic strain ranges. As a complementary approuch, the continous damage concept adopted in this work (Kachanov, 1986; Lemaitre and Caboche, 1990; Lemaitre and Dufailly, 1987; Lemaitre, 1984; Lemaitre, 1987; Hubscher, 1992) leads to the development of a macroscopic description of the sucessive physical phenomena giving rise to the crack initiation. In the theory, a damage internal variable describing the progressive deterioration of the material before the macroscopic crack initiation is introduced. A particular definition of this damage variable gives a macroscopic measured which constitutes a guideline to the development of differential damage equations. Classically the damage variable (called D) increases during the life from zero for a virgin state to one at failure.

Manuscript received October 1992. Associate Technical Editor: Agenor de Toledo Fleury

The main purpose of this paper is to use the Continuous Damage Mechanics to analyse the cumulative damage in elevated temperature steam pipes. The interest in the area of remaining life prediction arises from the need to avoid costly outages, safety considerations and the necessity to extend the component operation life beyond the original design life.

Some examples show the possibilities of this approach: Initially the low cycle fatigue of stainless steel bars subjected to cyclic loadings at 20ºC and 600ºC is analyzed. The predicted lifes are compared to those obtained by considering the εN method, based on the Coffin-Manson law (Hubscher, 1992). Then, the creep damage analysis of the bars at 600ºC is performed. Finally, the theory is employed to estimate the life of elevated temperature steam pipes, considered as thin walled pressure vessels. Steam pipes are typically used under high temperature operating conditions. Because of the combination of a variable pressure loading and high temperature exposure, they are likely to be subjected to creep-fatigue damage.

Constitutive Model

The set of elasto-viscoplastic constitutive equations used in this work describes the mechanical behavior of metallic materials submitted to non-monotonic loadings. These equations are an extention of the damage models proposed by Lemaitre and Chaboche (Lemaitre and Caboche, 1990; Lemaitre and Dufailly, 1987; Lemaitre, 1984; Lemaitre, 1987). Such kind of constitutive theory has a strong thermodynamic basis and a carefull presentation can be found in Hubscher, (1992); Pacheco, (1992) and Costa Mattos, (1988). In this paper, we will only summarize the main features and restrict the study to isothermal transformations.

In order to model the complex behavior of metallic materials at high temperatures, besides the stress σ, the total strain ε and the anelastic strain ε^a, we will introduce a macroscopic internal variable $D\ (0 \leq D < 1)$, called Damage. The variable D is a macroscopic quantity which can be interpreted as a local measure of the degradation (damage) of the material induced by the anelastic deformation. If D=0, the material is virgin and when $D \rightarrow 1$ the material loses locally its mechanical strenght. In general, for the sake of security, the rupture is supposed to take place when the variable D reaches a critical value D_{cr} such that $0 < D_{cr} < 1$. For further details about the physical interpretation of D see Lemaitre and Dufailly (1987).

The following set of constitutive equations is proposed:

$$\sigma_{ij} = (1-D)\,C_{ijkl}\,(\varepsilon_{kl} - \varepsilon^a_{kl}) \tag{1.1}$$

$$\dot{\varepsilon}^a_{ij} = \frac{3}{2(1-D)} \left\langle \frac{F}{(1-D)\,k} \right\rangle^n \frac{(S_{ij} - X_{ij})}{J(S-X)} \tag{1.2}$$

$$\dot{p} = \left(\frac{2}{3}\,(\dot{\varepsilon}^a_{ij})^2\right)^{1/2} \tag{1.3}$$

$$\dot{X}_{ij} = \frac{2}{3} a\dot{\varepsilon}^a_{ij} - \varphi X_{ij}\dot{p} \tag{1.4}$$

$$\dot{R} = bd\ \exp(-dp)\,\dot{p} \tag{1.5}$$

$$\dot{D} = \dot{D}_f + \dot{D}_c\ ;\ \dot{D}_f = W^e S_f \dot{p}\ ;\ \dot{D}_c = (W^e S_c)^{r/2} \tag{1.6}$$

where a, b, d, k, n, φ, r, S_c and S_f are material constants; σ_{ij} are the components of the stress tensor σ; C_{ijkl} are the components of the classical symmetric fourth-order tensor of elasticity C (in the next sections we will consider isotropic elastic materials which have only two independent components in the elastic tensor); p, X_{ij} and R are auxiliary variables; D_f is the fatigue damage and D_c is the creep damage. The main differences between this constitutive model and the elasto-viscoplastic equations presented in Lemaitre and Caboche (1990) are the evolution law (1.6) and the definition of the yield function F which has the following form:

$$F = J(S - X) - R - (1 - D)R_0 \tag{2}$$

where $J(S - X) = \left[\frac{3}{2}(S_{ij} - X_{ij})^{1/2}\right]^{1/2}$. $S_{ij} = \sigma_{ij} - (1/3)\sigma_{kk}$ are the components of the deviatoric stress. R_0 is a material constant.

If $F \leq 0$ then $\dot{\varepsilon}^a_{ij} = 0$, $\dot{p} = 0$, $\dot{X}_{ij} = 0$, $\dot{R} = 0$ and $\dot{D}_f = 0$, consequently, the only dissipative mechanism will be the creep damage.

When $R=0$ and $X_{ij}=0$, the condition $F < 0$ is nothing else than the classical Von-Mises criterion:

$$J(S) - R_0 < 0 \tag{3}$$

It can be verified that the elastic domain presented in the equation (3) (the set of the stresses σ^* such that $F(\sigma^*, R=0, X_{ij}=0, D=0)<0$) defines a sphere of radius $\sqrt{(2/3)}\,R_0$ in the space of the principal components of the deviatoric stress S. Experimentally, it is verified that the anelastic deformation induces an evolution of the elastic domain - a translation (known as kinematic hardening) and a dilatation or contraction (known as isotropic hardening).

Using the equations (1), it can be shown that if $R=0$ and $X_{ij}=0$ at time $t=0$, the evolution of the elastic domain (the set of the stresses σ^* such that $F(\sigma^*, R(t), X_{ij}(t), D(t))< 0$) will be characterized by a dilatation or contraction (due to the term $R(t) + (1-D)R_0$) and by a translation (due to $X(t)$) of the initial elastic domain (defined by the Von-Mises criterion)

Equations (1.2) and (1.4) implie that $tr(\varepsilon^a)=0$. This means that the anelastic deformation do not change the volume of the body. The equations (1) describe adequately the mechanical phenomena of damage, elasticity, plasticity, creep and relaxation observed in many metallic materials at high temperatures. Experimental procedures to measure the variable D can be found in Lemaitre and Dufailly (1987).

A consistent constitutive theory based on the concept of internal variables must not admit processes where the second law of thermodynamics is not satisfied. It can be shown (Costa Mattos, 1988) that the equations (1) will always verify the second law restriction independently of the geometry of the body, of the external loadings and of the boundary conditions.

Simulation of Cyclic Uniaxial Tests

The analysis of uniaxial problems is interesting since it allows the comprehension of the basic features of the theory. In a tensile test, the stress component in the axial direction is $\sigma_{xx}=(T/A)$, where T is the axial force and A is the cross-section area. All other components are equal to zero.

The Fig. 2 shows the curve σ_{xx} versus ε^a_{xx} computed for a 316 L stainless steel bar under traction-compression ($\max\sigma_{xx}=-\min\sigma_{xx}$, see Fig. 1). The stress range is $\Delta\sigma_{xx} = 660$MPa ($\Delta\sigma_{xx} = \max\sigma_{xx} - \min\sigma_{xx}$). The material parameters are: $E=196000$ MPa, $R_0=133$ MPa, $k=151$ MPa $\sec^{(1/n)}$, $n=24$, $a=162000$ MPa, $b=60$ MPa, $d=8$, $\varphi=2800$, $S_f=2.5$ MPa^{-1}, $S_c=0$. It is important to remark that the parameter S_c is equal to zero, hence, there will only be fatigue damage in this case. The parameters E, S_0, k, n, a, b, d, φ are given in Lemaitre and Caboche (1990) and the parameter S_f was obtained from fatigue tests. The curve in Fig. 2 was obtained by solving numerically (using a fourth order predictor-corrector technique) the system of ordinary equations formed by the constitutive equations (1) and the following initial conditions: $\varepsilon^a_{ij}(t=0) = 0$; $p(t=0) = 0$; $X_{ij}(t=0) = 0$; $R(t=0) = 0$; $D(t=0) = 0$. All the results presented in the next sections are obtained considering the same set of initial conditions and the same kind of numerical techique. Its obvious that, due to the particular form of the stress tensor in the uniaxial case, it is possible to do many simplifications in the system of equations (1). In this case it can be shown (Pacheco, 1992; Costa Mattos, 1988) that the anelastic strain ε^a is such that $-(\varepsilon^a_{xx})/2 = \varepsilon^a_{zz} = \varepsilon^a_{zz}$ and that the kinematic hardening variable X is such that $-X_{xx}/2 = X_{yy} = X_{zz}$ (all other components are equal to zero).

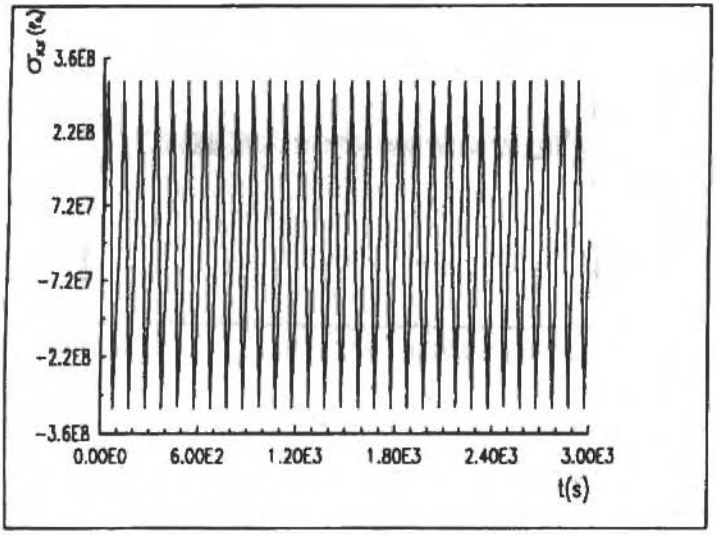

Fig. 1 σ_{xx} **versus t curve**

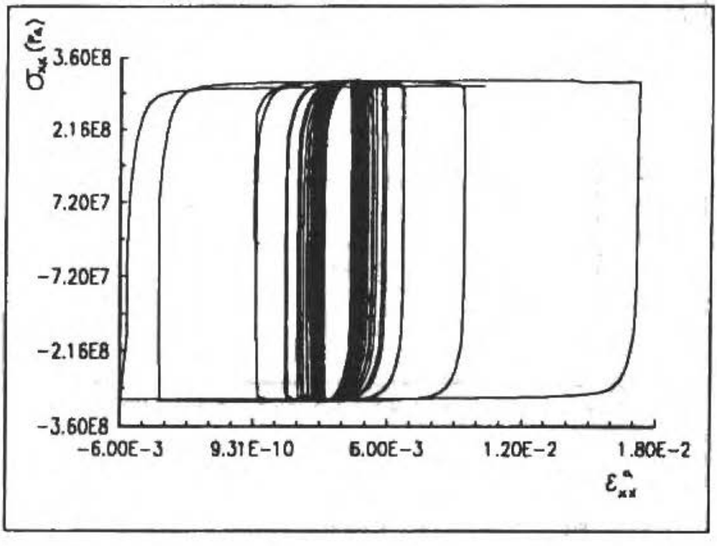

Fig. 2 σ_{xx} **versus** ε^a_x **curve. 316 L stainless steel at 20°C**

The evolution of ε^a_{xx} is shown in Fig. 3. The anelastic strain range ($\Delta\varepsilon^a_{xx} = \max\varepsilon^a_{xx} - \min\varepsilon^a_{xx}$) per cycle initialy decreases to a minimum value and then it increases until the rupture. In this kind of material, the critical value D_{cr}=0.2 is taken as the limit to the macroscopic crack initiation.

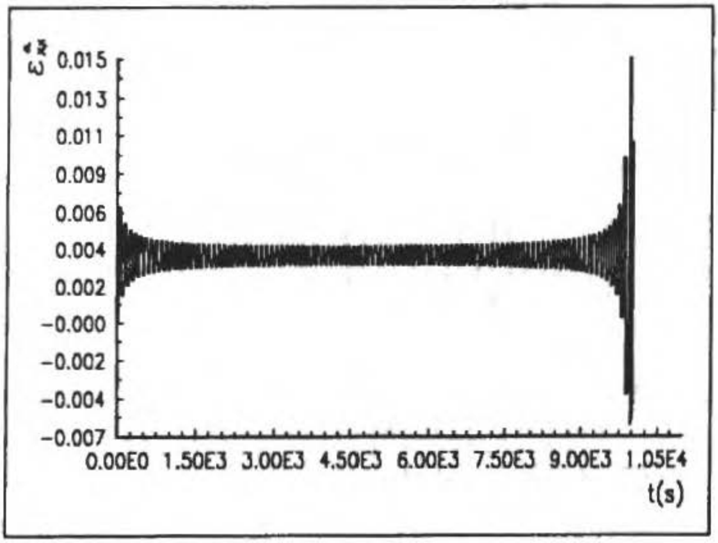

Fig. 3 ε^a_{xx} **versus t curve. max**σ_{xx}**=-min**σ_{xx}**=330 MPa**

The evolution of the damage variable D is presented in Fig. 4.

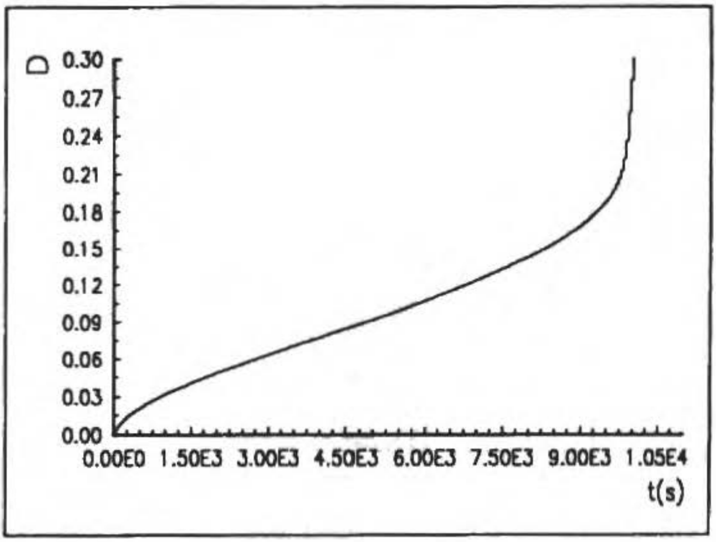

Fig. 4 D versus t curve. maxσ_{xx}**=-min**σ_{xx}**=330 MPa**

It can be verified that there is a change in the behavior of the curve D versus t after the cycle N_f when it is assumed the initiation of a macrocrack. After the cycle N_f, the damage increment ΔD and the cumulated anelastic strain increment Δp per cycle increase very quickly. This change in the response of the material can be easily seen in the curve σ_{xx} versus D in Fig. 5.

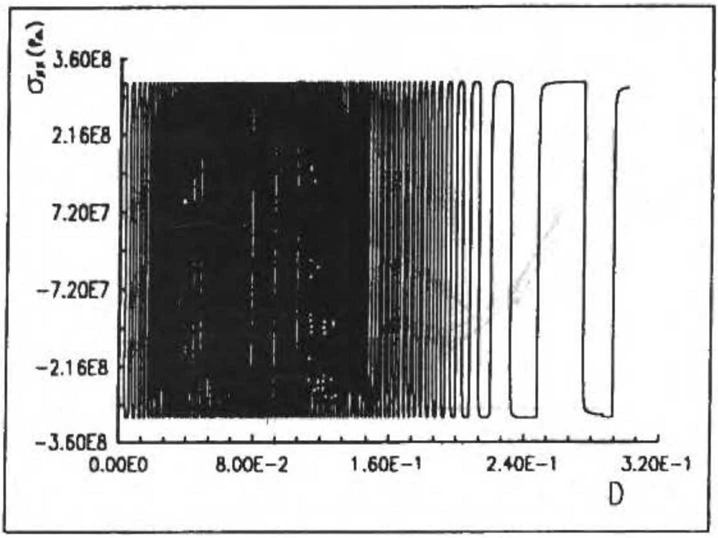

Fig. 5 σ_{xx} **versus D curve.** $\max\sigma_{xx}=-\min\sigma_{xx}=330$ **MPa**

The predicted lifes for this stainless steel bar under traction-compression using the εN method and the proposed theory considering two values for D_{cr} are presented in Fig. 6. In the εN method, the number of cycles N_f is computed from the following formula:

$$\frac{\Delta\sigma_{xx}}{E} + \left(\frac{\Delta\sigma_{xx}}{k_c}\right)^{Mc} = \frac{c_2}{E}(N_f)^{-1/\gamma_2} + c_1 (N_f)^{-1/\gamma_1} \tag{4}$$

where c_1, c_2, k_c, M_c, γ_1, and γ_2 are material constants. For this stainless steel at 20ºC we have (Lemaitre and Caboche, 1990): $c_1=0.34$, $c_2=3280$ MPa, $\gamma_1=2.07$, $\gamma_2=5.70$, $k_c=811$ MPa, $M_c=10.5$.

At the temperature of 600ºC, the material constants for this stainless steel are: E=131000 MPa, $R_0=6$ MPa, k= 150 MPa $\sec^{(1/n)}$, n=12, a=24800 MPa, b=80 MPa, d=10, φ=300, $S_f=2.5$ MPa^{-1}, $S_c=112.9$ $(\text{MPa hour})^{-1}$, r=6.5.

It is important to remark that the parameter S_c is different from zero. Hence, in this case, there will also be a creep damage. The parameters E, R_0, k, n, a, b, d, φ, are given in Lemaitre and Caboche (1990), the parameter S_f was obtained from fatigue tests, S_c and r=6.5 were obtained from creep tests. In Fig. 7 it is shown the number of cycles N_c necessary to reach a damage value $D_{cr}=0.5$ (taken as a critical value) for different values of $\Delta\sigma_{xx}$. It can be verified that there is a very small evolution of D_c and, hence, the damage is mainly due to fatigue.

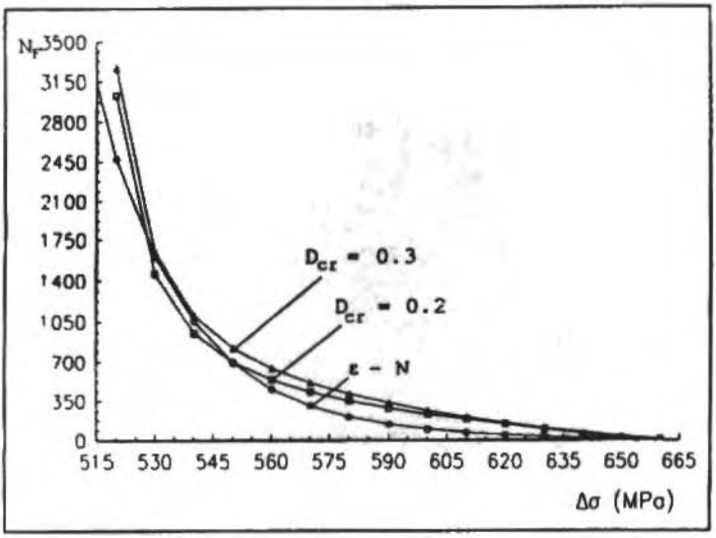

Fig. 6 N_f versus $\Delta\sigma_{xx}$ curves - curve 1: εN method prediction
curve 2: Continuous damage model prediction, D_{cr}=0.2
curve 3: Continuous damage model prediction, D_{cr}=0.3

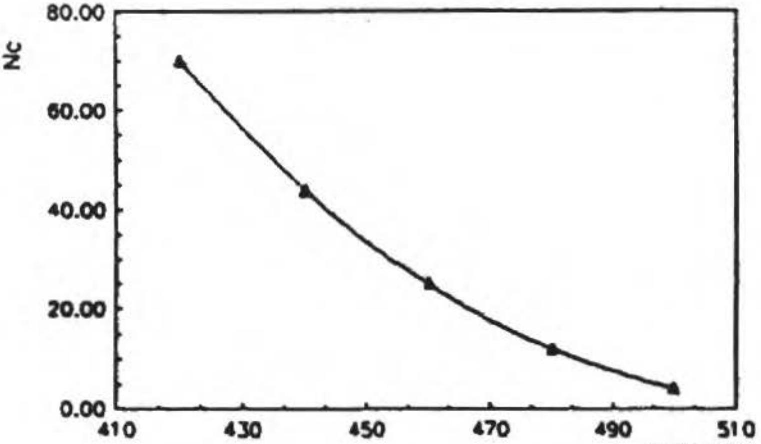

Fig. 7 N_c versus $\Delta\sigma_{xx}$ curve

Simulation of Creep Tests

The system of equations and the initial conditions used to model a creep test is similar to those used to model cyclic uniaxial tests of the stainless steel at 600ºC. The only difference is that in this case the stress component σ_{xx} is a constant value. The times t_c necessary to reach a critical damage D=0.5 for different stress values are: t_c=535 years when σ_{xx}=80 MPa; t_c=125 years when σ_{xx}=100 MPa; t_c=38 years when σ_{xx}=120 MPa. It can be verified that there is a very small evolution of D_f and, hence, the damage is mainly due to the creep mechanism. The evolution of ε_{xx}^{a} for an initial stress σ_{xx}=80MPa is shown in Fig. 8. The proposed model allows an adequate modelling of the primary, secondary and tertiary creep observed in metals and alloys.

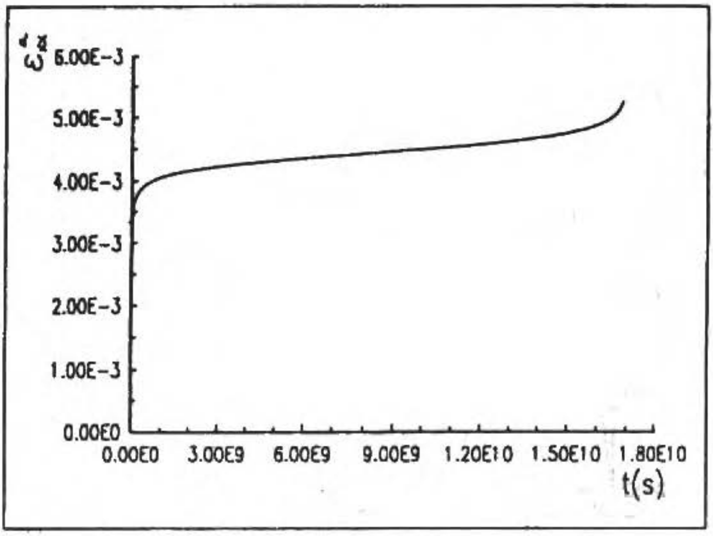

Fig. 8 Evolution of ε_{xx}^{a} in a creep test

The evolution of the damage variable in the same test is given in Fig. 9.

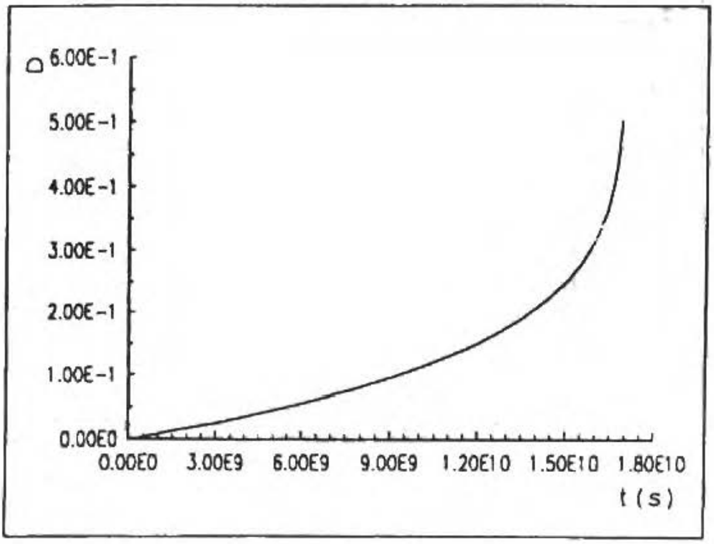

Fig. 9 Evolution of D in a creep test

Steam Pipe Under Variable Pressure

Denoting P the internal pressure, r the inner radius and e the wall thickness and considering that (10e) < r, the stresses in a steam pipe subjected to a pressure loading can be approximated by: $\sigma_{\theta\theta}=(Pr)/(e)$, $\sigma_{zz}=0$, $\sigma_{rr}=0$, all other components are equal to zero.

We will consider a temperature of 600°C, with the following pressure history

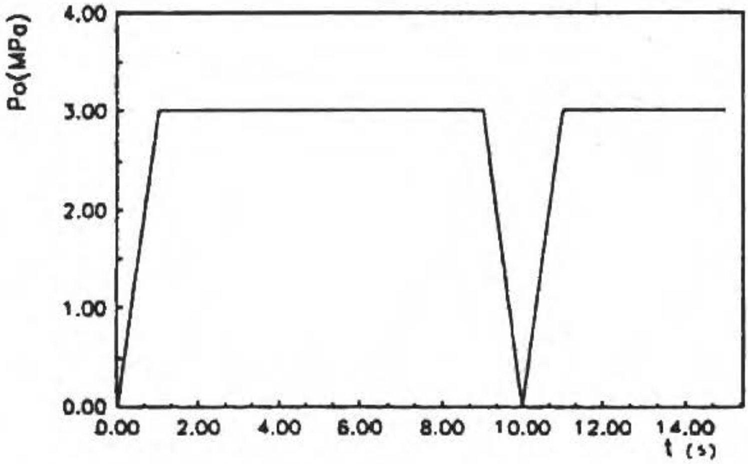

Fig. 10 Pressure loading

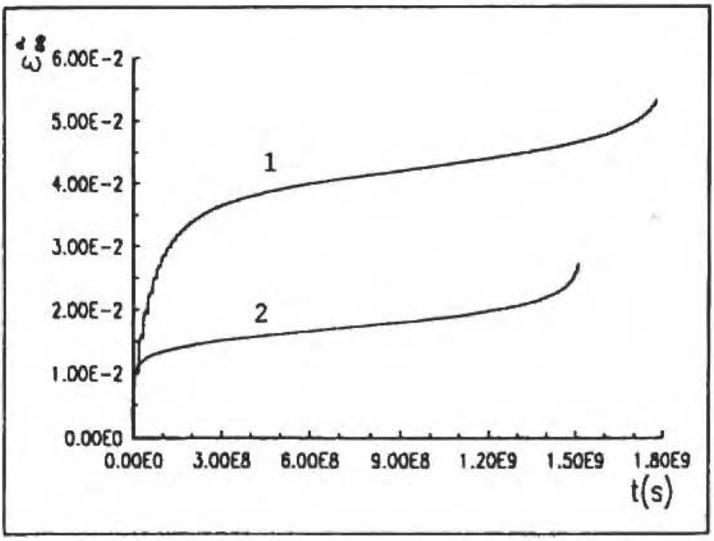

Fig. 11 $\varepsilon^{a}_{\theta\theta}$ versus t curve - curve 1: cyclic pressure - curve 2: constant pressure

The times t_c necessary to reach a critical damage D=0.5 for different maximum pressures P_0 are: t_c=824 years when P_0=2 MPa; t_c=56.4 years when P_0=3 MPa. In this case there is a small evolution of the fatigue damage, nevertheless, the cyclic loading shown in Fig. 10 leads to a mechanical response which is very different from the response obtained if a constant pressure P_0=3 MPa is considered (t_c=48 years). Due to the ratcheting phenomenon, the anelastic deformations are bigger in the case of cyclic loading than in the case of constant loading (see the evolution of the anelastic strain $\varepsilon^a_{\theta\theta}$ for both cases in Fig. 11).

On the other hand, the damage rate in the constant pressure case is bigger than in the variable pressure case, as it can be seen in Fig. 12.

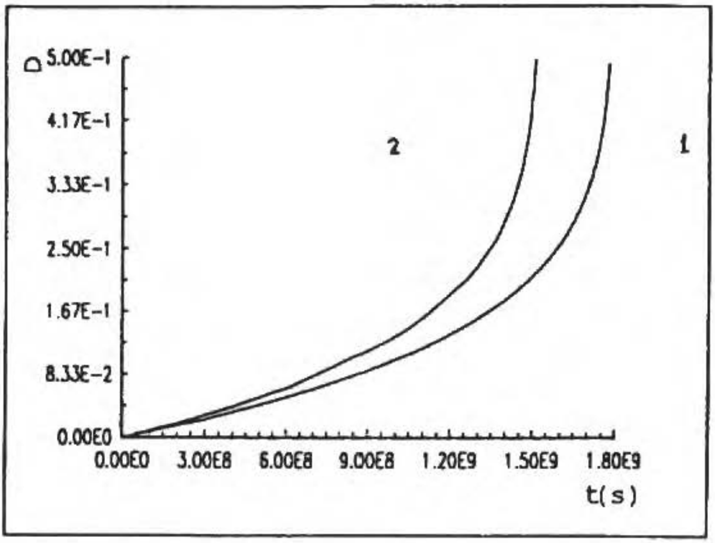

Fig. 12: D versus t curve - curve 1: cyclic pressure - curve 2: constant pressure

Conclusion

The classical methods for lifetime prediction, although very effective in many practical situations, are generally restricted to some simple geometries and cannot be generalized sistematically. The continuum damage models are more complex and difficult to apply in simple problems, nevertheless, they are valid for any kind of geometry, for any kind of loading and have a very strong thermodynamical basis. The model proposed in this paper to predict the creep/low-cycle fatigue damage of steam pipes allows the simulation of the elasto-viscoplastic behavior and can be used even if complex loading histories are considered. This work is a first attempt to develop a general methodology for the prediction of the remaining life of mechanical components operating at elevated temperatures. This is fundamental to extend the operation life beyond the original design life. A more complete version of the constitutive equations (1), including variable temperature effects, can be found in Pacheco (1992).

References

Costa Mattos, H., 1988, "Uma Contribuição à Formulação Termodinâmica da Elasto plasticidade e da Elasto viscoplasticidade", D. Sc. thesis, Eng. Mech. Department, PUC-RIO.

Hubscher, F., 1992, "Um Modelo de Dano Contínuo para a Análise da Fadiga de Baixo Ciclo de Barras Elasto-Viscoplásticas", M. Sc. Thesis, Eng. Mech. Department, PUC-RIO, 1992.

Kachanov, L. M., 1986, "Introduction to Continuum Damage Mechanics", Martinus Nijhoff, Dordricht.

Lemaitre, J., 1984, "How to use Damage Mechanics", Nuclear Engineering and Design, vol. 80, pp. 233-245.

Lemaitre, J., 1987, "Formulation Unifiée des Lois d' Évolution d' Endommagement". C. R. Acad. Sc. Paris, t. 305, Série II, p. 1125-1130, 1987.

Lemaitre, J. and Caboche, J. L., 1990, "Mechanics of Solid Materials", Cambridge University Press.

Lemaitre, J. and Dufailly, J., 1987, "Damage Measurements", Engineering Fracture Mechanics, vol. 28, pp. 643-661.

Pacheco, P. M. C., 1992, "Análise do Acoplamento Termomecânico em Materiais Elasto-Viscoplásticos", Internal Report, Eng. Mech. Department, PUC-RIO.

RBCM - J. of the Braz. Soc. Mechanical Sciences
Vol. XV - nº 1 - 1993 - pp. 65-78

ISSN 0100-7386
Printed in Brazil

Um Estudo Bibliográfico sobre o Problema de Transferências de Órbitas

A Survey on the Orbit Transfer Problem

Antonio Fernando Bertachini de Almeida Prado
Atair Rios-Neto
Instituto Nacional de Pesquisas Espaciais - INPE
Caixa Postal 515
12201-970 - São José dos Campos - S.P. - Brasil

Abstract

This paper presents the results obtained from a search in the literature about the problem of minimum fuel consumption spacecraft orbit transfer. The problem and several of its models are presented to allow a non-expert reader to understand them. More than one hundred papers are discussed allowing the reader to have a first idea about their contents before a more detailed study. The majority of these papers are available in Brazilian libraries.
Keywords: Orbit Transfer, Spacecraft Maneuvers, Satellite Orbit Control.

Resumo

Este trabalho tem por objetivo apresentar os resultados obtidos de um estudo da bibliografia existente sobre o problema de transferências de órbitas de um veículo espacial com consumo mínimo de combustível. O problema e as principais linhas de modelagem são definidos, de modo a permitir ao leitor não especialista no assunto um primeiro contato com o problema, bem como a fácil localização de mais de uma centena de artigos, a maioria disponíveis em bibliotecas brasileiras. Os artigos são citados de acordo com as definições apresentadas, permitindo ao leitor um conhecimento prévio do conteúdo dos mesmos, antes de estudá-los em detalhes.
Palavras-chave: Transferência de Órbita, Manobras de Veículos Espaciais, Controle de Órbita de Satélites.

Introdução

O problema de transferir um veículo espacial (dotado de propulsores) de uma órbita para outra tem crescido de importância nos últimos anos. Aplicações podem ser encontradas em diversas atividades espaciais, tais como na colocação de um satélite em órbita geoestacionária, no deslocamento de uma estação espacial, na manutenção de órbita de um satélite, no envio de sonda interplanetária, etc. Localmente, em termos de Brasil, uma importante aplicação desse tópico é a transferência inicial (para a sua órbita final) e a manutenção dessa órbita, que serão requeridas pelo primeiro satélite brasileiro de sensoriamento remoto, que faz parte da MECB (Missão Espacial Completa Brasileira). A MECB é inicialmente composta por um conjunto de quatro satélites: os dois primeiros de coleta de dados e os dois últimos de sensoriamento remoto, e foi criada com o objetivo de dotar o Brasil de capacidade de produzir e lançar seus próprios satélites. Os dois últimos satélites, de sensoriamento remoto, são os que requerem esse tipo de manobra.

Neste trabalho é apresentada a definição formal do problema e as principais linhas de modelagem. Mais de uma centena de referências são estudadas e apresentadas. O objetivo é proporcionar ao leitor com conhecimentos básicos de mecânica celeste e teoria de controle ótimo um rápido entendimento do problema, bem como servir como um "guia" para referências que estudem esse problema em maiores detalhes. O problema será sempre discutido em termos de transferência com mínimo consumo de combustível, embora outras variantes do problema existam na literatura, tais como: tempo mínimo para transferência, velocidade final mínima, encontro com outro veículo espacial, problema de Lambert (Battin e Vaughan, 1984), etc.

Esse artigo é baseado na dissertação de mestrado intitulada "Análise, Seleção e Implementação de Procedimentos que Visem Manobras Ótimas de Satélites Artificiais" (Prado, 1989), que foi desenvolvida e apresentada no Instituto Nacional de Pesquisas Espaciais (INPE). Maiores detalhes e testes numéricos podem ser encontrados nessa referência.

Manuscript received September 1992. Associate Technical Editor: Agenor de Toledo Fleury

Definição do Problema

Em termos conceituais, a transferência de um satélite com consumo mínimo de combustível consiste (Marec, 1979) em se alterar o estado (posição, velocidade e massa) de um veículo espacial das condições $\underline{r}_0$, $\underline{v}_0$ e m_0 no instante t_0, para $\underline{r}_f$, $\underline{v}_f$ e m_f no instante t_f ($t_f \geq t_0$) com o menor gasto de combustível (m_0-m_f) possível. A transferência pode ser completamente vinculada (no caso de "rendezvous", como aparece, por exemplo, em Wolfsberger, Weib e Rangnitt (1983) e Yablon'ko (1982)) ou parcialmente livre (tempo livre, velocidade final livre, etc.). No caso mais geral, deve-se fazer a escolha da direção, sentido e magnitude do empuxo (o controle disponível) a ser aplicado, respeitando-se os limites dos equipamentos disponíveis.

Em linguagem matemática, utilizando o ferramental de Controle Ótimo, tem-se a seguinte formulação:

Deseja-se minimizar globalmente:

m_f (massa final do satélite)

Com relação a:

$\underline{u}(.)$, o controle procurado, pertencente a um domínio U

Sujeito a:

Equações dinâmicas do movimento;
Vínculos devidos às órbitas inicial e final;
Outros vínculos desejados (regiões proibidas à propulsão, valores máximos e/ou mínimos das variáveis de controle, etc.).

Dados:

Todos os parâmetros necessários (gravitacionais, características do satélite, etc.).

Opções para Modelagem da Dinâmica, do Atuador e do Método de Otimização

A literatura sobre o assunto apresenta diversas modelagens na abordagem desse problema. Essas diferenças em modelagens podem ser divididas em três partes: diferenças quanto aos vínculos dinâmicos (equações de movimento), diferenças quanto ao controle aplicado (modo de atuação dos propulsores) e diferenças quanto ao método de otimização.

a) Diferenças quanto aos Vínculos Dinâmicos (Equações de Movimento)

Quanto as diferenças nas equações de movimento, a literatura pode ser dividida em 4 categorias básicas:

i) Modelagem simples de dois corpos. É assumida a presença de um astro massivo (como a Terra, a Lua, etc.) e de um veículo espacial de massa desprezível viajando nos arredores desse astro. Nenhuma

Nomenclatura

c = velocidade característica
C_n = constantes
D = direção do multiplicador de Lagrange
f = equação de movimento
F = força do propulsor
g = campo gravitacional
G = tensor gradiente de gravidade
H = hamiltoniana
m = massa
N = constante
O = órbita
p = multiplicador de Lagrange
r = posição
s = "range angle"

t = tempo
T = período orbital
u = controle
U = domínio do controle
$\mathcal{U}$ = função definida pela equação (7)
v,V = velocidade
W = velocidade de ejeção de gases
α = ângulo de "pitch"
α' = constante
β = ângulo de "yaw"
β' = constante
Γ = aceleração do propulsor
Δ = variação
μ = constante gravitacional

Sub-escritos

$\underline{\quad}$ = vetor
$\overline{c}$ = valor relativo a velocidade característica
f = valor final
i = valor intermediário
MAX = valor máximo
r = valor relativo à posição
v = valor relativo à velocidade
0 = valor inicial

Super-escritos

$*$ = valor ótimo
$'$,$''$ = denotam primeira e segunda derivadas

perturbação de outros corpos é assumida, e os dois corpos envolvidos são assumidos como pontos de massa. Todas as fases sem propulsão são assumidas como órbitas Keplerianas. É de longe o modelo mais estudado, devido à sua simplicidade, rapidez no fornecimento de resultados, existência de soluções analíticas e boa precisão na maioria das situações. É sempre o ponto de partida de uma análise de missão, independente da complexidade da mesma.

ii) Modelagem de dois-corpos perturbados. É o passo lógico seguinte. É adotado o modelo matemático do item anterior, acrescido de uma ou mais perturbações no sistema. Entre as perturbações mais comuns estão: não esfericidade do astro principal, atrito atmosférico, existência de pressão de radiação (quando o Sol está presente no sistema), presença de outros corpos, etc. Raramente existem soluções analíticas para esta modelagem, e integração numérica é a ferramenta mais utilizada. Linearizações em torno de uma órbita de referência para obtenção de resultados analíticos aproximados são também muito comuns. É um refinamento comum em análise de missões, após um estudo feito com a modelagem exposta no item i.

iii) Modelagem com três-corpos. É uma modelagem muito comum para o estudo de trajetórias lunares e interplanetárias. É assumido a presença de apenas três corpos no sistema, que são tratados como pontos de massa. Nenhuma outra perturbação é considerada. É muito comum o caso particular denominado "Problema restrito de três corpos", bastante detalhado no livro "Theory of Orbits" (Szebehely, 1967), onde o objetivo é descrever o movimento de um ponto de massa desprezível (por exemplo um veículo espacial) influenciado pela atração gravitacional de dois corpos massivos (que são chamados primários, como por exemplo a Terra e a Lua) durante toda a trajetória. Essa modelagem não possui solução analítica e usualmente integrações numéricas são efetuadas.

iv) Modelagem com N-corpos. Essa modelagem assume a presença de um número arbitrário N de corpos celestes. Outras perturbações geralmente não são incluídas e todos os N corpos são tratados como pontos de massa. Um exemplo para o caso N=4 pode ser encontrado em Pu e Edelbaum (1975). Importantes aplicações para esse tipo de modelagem ocorrem em missões multi-planetárias (diversos planetas e/ou satélites visitados por um mesmo satélite) como por exemplo as missões Voyager I e II, Galileo, etc. Em geral essa modelagem é utilizada para refinar uma solução encontrada por uma modelagem mais simples, como a de dois ou três corpos. Integração numérica e linearizações em torno de uma órbita nominal são recursos usados com frequência. É também muito comum o uso de manobras gravitacionalmente assistidas ("Swing-by") (Broucke, 1988, Szebehely, 1965 e Broucke e Prado, 1993a), onde a passagem por um dos corpos celestes é utilizada para fornecer energia ao veículo espacial para que ele complete a sua missão.

b) Diferenças quanto ao Controle Aplicado (Modo de Atuação dos Propulsores)

Quanto a modelagem do atuador (empuxo a ser aplicado ao veículo espacial) podemos notar a presença de duas grandes categorias:

i) Empuxo infinito: É assumido que o motor seja capaz de aplicar um empuxo instantâneo e de magnitude infinita. O efeito desse impulso é medido através de uma variação instantânea na velocidade do veículo espacial (ΔV), que é suposto ter uma trajetória contínua. É o modelo mais aplicado na literatura, devido a sua simplicidade e razoável precisão.

ii) Empuxo contínuo: É assumido que o motor seja capaz de aplicar um empuxo finito por um tempo diferente de zero. O efeito desse empuxo é medido por integrações numéricas das equações de movimento ou linearizações válidas por um curto período de tempo. Diversas variantes podem ser encontradas na literatura quanto ao grau de liberdade do empuxo: magnitude constante ou variável, possibilidade de mudar a direção do empuxo livremente ou com restrições (restrito a um plano ou cone, etc.), possibilidade de desligar o motor e alternar arcos propulsados com arcos balísticos, etc.

c) Diferenças quanto ao Método de Otimização

Quanto ao método de otimização, podemos agrupar a maioria da literatura existente em três grandes grupos:

i) Método direto. O problema é reduzido à busca direta de valores numéricos para um determinado número de parâmetros. Algorítmos computacionais são empregados para gerarem métodos iterativos que encontrem os valores dos parâmetros que tornem um certo funcional mínimo.

ii) Método indireto. Condições necessárias de primeira ordem (equações de Euler-Lagrange) são escritas e resolvidas analítica e numericamente. Essa solução nos fornece os dados necessários para encontrar a solução final procurada.

iii) Método híbrido. Condições necessárias de primeira ordem (equações de Euler-Lagrange) são escritas e resolvidas através de uma busca direta de parâmetros, a exemplo do método direto. Em outras palavras, as equações de Euler-Lagrange transformam o problema original num outro equivalente, que é então resolvido pelo método direto.

Tipos de Manobras

O número de aplicações do problema de transferências orbitais é bastante grande. Em todo caso, é possível agrupá-las em duas categorias principais, quanto ao tipo de manobras envolvidas:

i) Tranferências de órbita. Manobras de grande amplitude, destinadas a alterar significativamente a órbita do veículo espacial. Bons exemplos são: transferências de um satélite em baixa órbita terrestre para uma órbita alta (como a geoestacionária); transferências à Lua ou outros planetas, etc.

ii) Correções de órbita. Manobras de pequena amplitude, em geral feitas com o objetivo de manter um veículo espacial em determinada órbita, ao invés de alterá-la. Essas manobras são necessárias para compensar efeitos perturbadores que tendem a alterar a órbita nominal do veículo espacial. Bons exemplos são: manutenção de uma estação espacial, manutenção de satélites geossíncronos e heliossíncromos, etc.

Revisão da Literatura

O problema da transferência ótima de um veículo espacial entre dois pontos teve em R. H. Goddard (1919) um de seus primeiros estudiosos, que propôs soluções aproximadas para o problema de enviar um foguete a grandes altitudes, da forma mais econômica possível. É um problema intimamente relacionado ao tratado neste trabalho, embora não exatamente o mesmo.

A Transferência de Hohmann

A seguir veio o trabalho de Hohmann (1925), que obteve a solução ótima do problema de transferência de um veículo espacial entre duas órbitas circulares e coplanares em um campo gravitacional Newtoniano (que atua com uma lei do inverso do quadrado da distância). Essa solução ainda é usada até hoje, sob certas circumstâncias, e foi considerada como a solução final do problema até 1959. Ela estuda o caso de uma transferência bi-impulsiva entre duas órbitas circulares e coplanares com tempo livre. Os passos principais envolvidos nessa transferência estão resumidos abaixo.

Na órbita inicial (O_1) aplica-se um impulso na direção do movimento e de magnitude dada por $\Delta V_0=|\{2(r_f/r_0)/[(r_f/r_0)+1]\}^{1/2}-1|V_0$, onde: r_0= raio da órbita inicial, r_f= raio da órbita final, V_0= velocidade do veículo na órbita inicial, T_0 = período da órbita inicial. Com isso o veículo entra numa órbita de transferência elíptica (O) com periápside r_0 e apoápside r_f. Então, espera-se que o veículo complete meia revolução e atinja o apoápside, quando é aplicado o segundo e último impulso, na direção do movimento e com magnitude dada por $\Delta V_f=(r_f/r_0)^{-1/2}|1-\{2/(1+r_f/r_0)\}^{1/2}|V_0$, que faz com que o veículo entre em uma órbita circular de raio r_f. Com isso tem-se que o tempo de transferência é a metade do período orbital da órbita O, isto é $t=(1/2)\{[1+r_f/r_0]/2\}^{3/2}T_0$. Maiores detalhes na obtenção dos resultados acima podem ser obtidos em Marec (1979) e uma demonstração analítica de que a transferência de Hohmann é a verdadeira transferência ótima bi-impulsiva pode ser encontrada em Barrar (1963).

A transferência de Hohmann obteria, com o passar do tempo, grandes contribuições de outros pesquisadores e seria estendida ao caso elíptico (transferência entre duas órbitas elípticas, com empuxo infinito aplicado nos ápsides), como em Marchal (1965). Smith (1959) obteve soluções exatas e aproximadas para diversos casos de transferências entre duas órbitas coplanares, tais como: órbitas com eixos alinhados ou quase alinhados; uma das órbitas quase circular; as duas órbitas quase circulares. Bender (1962) apresenta uma modelagem abrangente, capaz de resolver qualquer transferência entre órbitas coplanares. Posteriormente os casos de órbitas não-coplanares também foram incluídos, adicionando-se componentes de empuxo fora do plano das órbitas inicial e final. McCue (1963) atacou o problema de uma transferência bi-impulsiva entre duas órbitas elípticas inclinadas, incluindo a possibilidade de "rendezvous". Em Eckel e Vinh (1984) encontra-se a solução ótima para o caso de transferências entre órbitas elípticas não-coplanares com tempo ou combustível fixo em que, quando se faz o tempo tender a infinito, chega-se ao resultado de Hohmann.

Outras colaborações vieram no sentido de obter a diferença entre o caso ideal (empuxo infinito) e o real (empuxo finito), como em Zee (1963) que, aproximando o empuxo aplicado como de direção perpendicular ao raio focal (raio vetor que vai do centro de atração ao veículo) e magnitude constante, obteve expressões analíticas para o consumo extra de combustível (quanto combustível extra seria necessário para efetuar a manobra prevista), deficiência de energia (quanto de energia se teria a menos, caso a manobra fosse efetuada com o combustível previsto pelo caso ideal) e variação dos elementos orbitais (quanto cada elemento orbital da órbita finita seria diferente do nominal, caso a manobra fosse realizada com o combustível previsto pelo caso ideal) devido à situação não ideal do propulsor, para diferentes valores do empuxo real aplicado.

Outra variante encontrada na literatura (Melton e Jin, 1991) consiste no estudo da transferência entre duas órbitas circulares com dois impulsos de magnitudes fixas, onde o objetivo é encontrar as direções dos impulsos.

A Transferência de Hoelker e Silber (Bi-elíptica e Tri-impulsiva)

No final da década de 50, Hoelker e Silber (1959) mostraram que a solução de Hohmann era a solução ótima apenas quando a razão entre os raios das órbitas final e inicial é menor que 11,94. Nos outros casos a transferência bi-elíptica tri-impulsiva é mais econômica. Essa transferência segue os seguintes passos: i) Aplica-se o primeiro impulso (ΔV_0) na órbita inicial, na direção do movimento do veículo, e com a magnitude tal que ele entre em uma órbita elíptica O_1 com periápside r_0 e apoápside r_i. É preciso que $r_i > r_f$, caso contrário a transferência de Hohmann seria mais eficiente; ii) Quando o veículo atinge o apoápside r_i, aplica-se o segundo impulso (ΔV), também na direção do movimento, e com magnitude tal que faça com que o veículo entre em uma órbita elíptica O_2 com apoápside em r_i e periápside em r_f; iii) Quando o veículo atinge o periápside aplica-se o terceiro impulso, agora contrário ao movimento, e com magnitude tal que faça com que o veículo entre em órbita circular de raio r_f.

É importante notar que a transferência é tanto mais eficiente, isto é, apresenta um menor valor na soma dos incrementos de velocidade necessários em cada etapa, quanto maior for o valor de r_i, conforme demonstrado em detalhes em Marec (1979). Essa manobra é mais eficiente que a manobra de Hohmann devido ao fato do segundo impulso ser aplicado longe do centro de atração, o que diminui o combustível necessário, porque a força de atração é muito mais fraca nesse ponto (ela é inversamente proporcional ao quadrado da distância entre os corpos).

Essa linha tri-impulsiva também mereceria a atenção de outros pesquisadores, que a estenderam ao caso elíptico (órbitas inicial e final elípticas), como em Ting (1960) que também mostrou que a aplicação de mais de três impulsos não pode levar a uma solução mais econômica (no caso ideal de empuxo infinito), e de Roth (1967) que obteve a solução de mínimo incremento de velocidade para a transferência bi-elíptica com mudança de plano orbital.

Uma interessante comparação de resultados, com relação ao tempo necessário para uma manobra de "rendezvous" (o problema de transferência completamente vinculado, em que um veículo espacial tem que encontrar um outro veículo espacial em órbita livre), aparece em Billik e Roth (1967) que mostrou que, na maioria dos casos, a transferência de Hohmann leva um tempo bem maior que a bi-elíptica.

A Transferência Bi-Parabólica

Uma vez que se sabe que, quanto maior o valor de r_i (distância do veículo ao foco, no momento do segundo impulso) mais eficiente é a transferência, é lógico se pensar no limite de r_i tendendo ao infinito. É justamente isso o que caracteriza a transferência bi-parabólica, que segue os seguintes passos: i) Na órbita inicial (O_0) aplica-se um impulso, na direção do movimento e com a magnitude (ΔV_0) tal que faça com que o veículo entre em uma órbita parabólica O_1; ii) Quando o veículo atinge o infinito (teoricamente, é claro) aplica-se um segundo impulso, infinitesimal, que faz com que o veículo passe da órbita O_1; para outra órbita parabólica O_2. Esse impulso não consome combustível, devido ao fato de r_i ser infinito; iii) Quando o veículo passa pelo periápside da órbita parabólica O_2 aplica-se o terceiro impulso, na direção oposta ao movimento e com magnitude (ΔV_f) tal que faça com que o veículo entre na órbita O_f. É óbvio que essa transferência não pode ser realizada na prática, pois o tempo necessário seria infinito, devido ao passo ii.

Em Marec (1979) pode-se encontrar gráficos comparando a eficiência dos três tipos de transferências citadas, para diferentes valores da razão r_f/r_0.

Outras Manobras Impulsivas

Uma outra linha de pesquisa, derivada da transferência de Hohmann, é aquela em que se parte do pressuposto de que a transferência será feita por uma série de impulsos no perigeu (em passagens consecutivas) seguida por uma série de impulsos no apogeu. Aqui a transferência leva várias órbitas para se concretizar, mas mantém-se o princípio de que impulsos nos ápsides são mais eficientes. Spencer, Glickman e Bercaw (1982) fornecem, através de gráficos e equações, o impulso extra necessário (em relação a manobra bi-impulsiva de Hohmann) em função dos raios das órbitas inicial e final e do número de revoluções usadas na transferência, para o caso de plano orbital fixo.

Depois disso, Redding (1984) iria um pouco mais a fundo e obteria um método de cálculo para a manobra não-impulsiva equivalente (uso de empuxo finito aplicado em arcos em torno dos ápsides), que forneceria a melhor escolha possível do número de arcos com propulsão em torno do perigeu e do apogeu, em função do tempo limite da transferência, bem como da "gravity loss" associada (diferença entre o incremento de velocidade real e o previsto pelo modelo impulsivo) e do valor do empuxo disponível. Os resultados foram obtidos para três casos distintos: empuxo constante, aceleração constante e aceleração constante por trechos. Matogawa (1983) também usou essa mesma idéia e deduziu expressões para o número e as extensões ótimas dos arcos com propulsão.

Outros trabalhos que utilizam a aproximação impulsiva, que é de longe a mais explorada na literatura (Gobetz e Doll, 1969), podem ser encontrados em Eckel (1962), que encontra a melhor solução bi-impulsiva para o caso de órbitas elípticas não-coplanares, depois generalizada para o caso de N impulsos (porém com N dado a priori) em Eckel (1963); em Prussing (1970) (dois ou três impulsos); Prussing (1969) (quatro impulsos); Moyer (1965), que estuda o caso de uma transferência entre uma órbita circular e uma elíptica; Pines (1964), que encontra e aplica constantes de movimento ao caso impulsivo; e Robbins (1966), que faz um estudo analítico da aproximação impulsiva. Uma abordagem analítica alternativa para o problema de transferências coplanares com N impulsos é encontrada em Broucke e Prado (1993b), onde a vantagem das transferências que passam pelo infinito é discutida em detalhes.

Mais modernamente quase todos os trabalhos buscam, de alguma forma, obter não só as magnitudes e direções dos impulsos, mas também o seu número, não mais se fazendo essa hipótese "a priori". Exemplos são os trabalhos de Lion e Handelsman (1968), Jezewski e Rozendaal (1968), Gross e Prussing (1974), Eckel (1982) e Prussing e Chiu (1986).

Em Redding e Breakwell (1984) encontra-se uma interessante abordagem sobre o caso de propulsão quase-impulsiva, estudada a partir da impulsiva; e em Hazelrigg (1984) o teorema de Green foi utilizado para obter a solução ótima para a transferência entre órbitas coplanares e coaxiais sem restrição de tempo ou ângulo.

Exemplos de abordagens com uma mistura de duas aproximações (linearização e sistema de propulsão impulsivo) podem ser encontrados em Marec (1968) e em Stern (1984).

Um enfoque diferente, usando considerações de energia, pode ser encontrado em May (1986).

Um problema similar, o da transferência bi-impulsiva de um corpo celeste para ele mesmo (algum tempo depois) é discutido em Prado e Broucke (1993).

O Caso com Empuxo Finito

A consideração de hipóteses mais realistas de trabalho leva ao caso mais geral, o de propulsão finita. Dentro dessa linha o trabalho de Tsien (1953) mostrou que um empuxo na direção do movimento é mais eficiente que na sua perpendicular, e o de Lawden (1955) buscou direções ótimas para a aplicação do empuxo (do ponto de vista de máxima transferência de energia por unidade de massa expelida) próximas à direção do movimento.

Ainda nessa linha de busca, foram feitos outros trabalhos. Moskowits (1963) publicou os resultados de dois tipos de aproximação: a linear ($tg[\alpha(t)]=C_1+C_2.t$, onde $\alpha(t)$ é o ângulo entre a força de empuxo aplicada e uma linha adotada como referência, C_1 e C_2 são constantes e "t" é o tempo); e a bilinear ($tg[\alpha(t)]=(C_1+t)/(C_2+C_3.t)$, onde C_1, C_2 e C_3 são constantes), ambas para o caso de pequenas transferências (correções) de órbitas, sem mudança do plano orbital.

Uma outra aproximação linear foi desenvolvida por Biggs (1978), desta vez $\alpha=\alpha_0+\alpha'.s$ e $\beta=\beta_0+\beta'.s$, onde α e β são os ângulos de "pitch" e "yaw", respectivamente, α_0, α', β_0 e β' são constantes e "s" é o "range angle", que é o ângulo que o raio vetor do satélite faz com uma linha arbitrária pertencente ao plano da órbita. O método se aplica à transferências de grande ou pequena amplitude e o método de otimização é paramétrico. Logo depois, Biggs (1979) estenderia esse trabalho ao caso mais genérico ($\alpha(t)$ e $\beta(t)$ livres), utilizando o método híbrido de otimização. Esse mesmo método híbrido é utilizado em Prado (1990) para uma transferência entre a Terra e a Lua. Tratamento híbrido análogo, com a diferença de que são usadas coordenadas polares ao invés de elementos Keplerianos, pode ser encontrado em Weib (1985) ou Erno (1983). Em Tomita e Feiring (1985) encontra-se a mesma abordagem híbrida, mas com a proposta de um novo algorítmo numérico para a solução do problema de minimização; e em Denham e Bryson (1964) o algorítmo "Steepest-Ascent" é utilizado no mesmo problema.

Em trabalhos independentes, usando abordagem com método direto, com parametrização da função de controle do problema de controle ótimo associado, Ceballos (1980) e Ceballos e Rios-Neto (1981), usando programação linear, e Rios-Neto e Bambace (1981), usando estimação linear ótima de parâmetros, resolveram um problema de transferência em tempo mínimo da Terra a Marte, com baixo empuxo de direção variável.

Um outro bom exemplo de resultados analíticos aproximados pode ser encontrado em Broucke (1991), onde é considerado o problema de uma transferência ótima com aplicação de um empuxo baixo e contínuo.

A Teoria do "Primer-Vector"

Durante as décadas de 50 e 60 muitos trabalhos surgiram tratando o problema como um problema de Mayer (Bell, 1968), e a obtenção das condições de otimalidade foram feitas por muitos pesquisadores e para diversos casos.

Nessa mesma época, em dois importantes artigos, Lawden (1953 e 1954) introduziu a noção de "primer vector", ou seja, o multiplicador de Lagrange associado ao vetor velocidade, que desempenha importante papel nas teorias modernas de trajetórias ótimas.

Essa abordagem foi muito explorada na literatura subsequente, e é empregada tanto na sua forma original como nas formas aproximadas (para o caso impulsivo e/ou entre órbitas próximas, usando linearizações em torno de uma órbita intermediária). Exemplos desse tipo de abordagem (linearizações) podem ser encontrados em Carter (1984) e McCue (1967). É importante frisar que existem muitos outros trabalhos teóricos importantes, como por exemplo Contensou (1962) e Culp (1967), mas que não foram tão explorados pela literatura subsequente.

Nessa abordagem ("primer-vector") nenhuma hipótese é feita "a priori", nem de ausência de arcos balísticos, nem de parametrizações para o controle. A abordagem mostrada será para o sistema de propulsão do tipo "CEV" (velocidade de ejeção de gases constante) e campo gravitacional central, variando com o inverso do quadrado da distância, embora qualquer outro caso possa ser estudado, como o de um campo da forma $g=-\mu/r^N$ (Brookes, 1970) ou de um campo genérico da forma $g=g(r,t)$ (Marec, 1979).

Para desenvolver essa teoria é preciso, inicialmente, definir o vetor estado que terá as sete componentes: vetor posição ($\underline{r}$), com três componentes; vetor velocidade ($\underline{v}$), com três componentes; velocidade característica (c), com uma única componente que substitui a massa ($c=\int\Gamma$¶$t=-\int(W/m)dm=W.\ln(m_0/m)$, onde $\Gamma=F/m$ é a aceleração devida ao empuxo, que é estritamente decrescente com a massa e W é a velocidade de ejeção de gases), e que mede o combustível gasto. Com essas definições, as equações de movimento ficam:

$$\dot{\underline{r}}=\underline{v} \tag{1}$$

$$\dot{\underline{v}}=-\mu\underline{r}/r^3+\underline{\Gamma} \tag{2}$$

$$\dot{c}=\Gamma \tag{3}$$

e a hamiltoniana fica:

$$H=\underline{p}.\underline{f}=\underline{p}_r.\underline{v}+\underline{p}_v(\underline{\Gamma}-\mu\underline{r}/r^3)+p_c\Gamma \tag{4}$$

e, para que ela seja máxima (Princípio de Máximo de Pontryagin), deve-se escolher $\underline{\Gamma}$ na direção de $\underline{p}_v$ (que chamaremos $\underline{D}$). Assim, a Hamiltoniana fica:

$$H=\underline{p}_r.\underline{v}+\underline{p}_v.\Gamma-\underline{p}_v\mu\underline{r}/r^3+p_c\Gamma \tag{5}$$

e, novamente com o Princípio de Máximo de Pontryagin, o valor ótimo de Γ (Γ^*) é:

$$\Gamma^*=\Gamma_{max}(c).U(p_v+p_c) \tag{6}$$

onde:

$$U(x)=(1+1.\mathrm{sign}(x))/2 \tag{7}$$

vale 1 se $p_v+p_c>0$ e 0 se $p_v+p_c<0$.

Tem-se, então, o controle do tipo "bang-bang", isto é, arcos balísticos alternados com arcos de empuxo máximo, conforme o sinal de (p_v+p_c). No caso $p_v+p_c=0$, num intervalo finito, tem-se um arco singular. Nesse caso o Princípio de Máximo de Pontryagin não pode determinar o módulo de $\underline{\Gamma}$ (a direção continua a ser $\underline{D}$). Maiores detalhes desse enfoque podem ser encontrados em Marec (1979) e Kopp e Moyer (1965) e enfoques alternativos em Lawden (1962) ou Robbins (1965).

Assim sendo, é necessário estudar o comportamento das equações adjuntas:

$$\dot{\underline{p}}_r=-\partial H/\partial\underline{r}=-\underline{p}_v.\underline{G} \tag{8}$$

$$\dot{\underline{p}}_v=-\partial H/\partial\underline{v}=-\underline{p}_r \tag{9}$$

$$\dot{p}_c=-\partial H/\partial c=-(\Gamma^*/W).(p_v+p_c) \tag{10}$$

onde $\underline{G}$ é o tensor gradiente de gravidade ($\partial\underline{g}/\partial\underline{r}$).

Combinando as duas primeiras equações, tem-se a equação diferencial para $\underline{p}_v$ o chamado "primer-vector":

$$\ddot{\underline{p}}_v=\underline{p}_v.\underline{G} \tag{11}$$

O problema agora fica resumido à integração das equações adjuntas, para obter-se os trechos com propulsão e os com arcos balísticos. Porém, para que isso seja efetuado, é necessária a obtenção de um número suficiente de condições de contorno, já que existem elementos do estado final que podem não possuir valores fixos (a menos de uma manobra de "rendezvous"). As condições de contorno iniciais e algumas finais (relações e/ou valores fixos) do estado são dados pelo próprio enunciado do problema (órbita e massa iniciais e valores desejados para a órbita final). As demais condições de transversalidade (Bryson e Ho, 1975), que variam de missão para missão (interceptação, transferência, "rendezvous", etc.) Para o problema em questão (transferência com tempo livre) elas são:

$$H^*=0 \tag{12}$$

$$\underline{p}_{rf}.\underline{v}_f+\underline{p}_{vf}.\underline{g}_f=0 \tag{13}$$

$$\underline{p}_{r0}.\underline{v}_0+\underline{p}_{v0}\underline{g}_0=0 \tag{14}$$

$$p_c=-1 \tag{15}$$

onde $\underline{g}_0$ e $\underline{g}_f$ representam o campo gravitacional nos instantes inicial e final, respectivamente.

Porém, não é conhecido um conjunto completo de condições de contorno em um mesmo instante. Essa particularidade impede que uma solução analítica geral seja encontrada para esse problema, mas existem soluções numéricas, como por exemplo em Subrahmanyam (1986). Esse problema é conhecido na literatura como "Two Point Boundary Value Problem" (TPBVP).

Na literatura podem ser encontrados trabalhos específicos sobre a integração dos multiplicadores de Lagrange, como os de Vinh (1972), Eckenwiler (1965) e Hempel (1966), que obtém soluções analíticas para os arcos balísticos e comparações dos resultados com a solução numérica; ou o de Handelsmann (1966), que calcula estimativas dos valores iniciais dos multiplicadores de Lagrange a partir da solução bi-impulsiva ótima.

Também surgiram trabalhos mais específicos, tratando com casos particulares, como Zondervan, Wood e Caughey (1984), que otimiza a solução com três arcos de empuxo contínuo e grandes mudanças de plano orbital.

O caso impulsivo também tem espaço dentro da abordagem baseada no "primer-vector". Basta fazer $\Gamma_{max} \rightarrow \infty$ e $t \rightarrow 0$, assim:

$$\Delta c(\text{finito}) = \int \Gamma_{max} dt \tag{16}$$

onde o integrando cresce ao infinito, mas o intervalo de integração vai a zero.

Para se evitar problemas matemáticos devidos à essa aproximação, é conveniente escolher "c" como variável independente, ao invés do tempo. Com isso obtem-se que $\underline{r}$, t, $\underline{p}_r$, $\underline{p}_v$, H^* e p_c são constantes durante o impulso (logo $p_c=1$, pois $\dot{p}_c=0$ e em $t_f p_c=-1$). Para $\underline{p}_v$ sabe-se que $\underline{p}_v \leq p_c=1$, atingindo o valor 1 (com $\dot{\underline{p}}_v=0$) nos instantes de aplicação de empuxo (Marec, 1979).

Uma abordagem semelhante para o caso impulsivo, mas levando em conta o efeito do achatamento da terra nas equações de movimento, pode ser encontrada em Fernandes (1986), Fernandes e Moraes (1989) (que estuda os casos não-singulares) e Fernandes (1989) (que estuda os casos singulares). Outra possibilidade estudada, por Fernandes e Sessin (1989), é essa mesma influência do achatamento da Terra em uma transferência de baixo e contínuo empuxo, através de uma expansão analítica e aplicação do método de Hori para sistemas canônicos.

Uma outra opção, com mais restrições, aparece em Wiesel e Alfano (1985) e resolve o problema da otimização do ponto de vista de tempo mínimo (mas, como o empuxo é contínuo e de magnitude constante, isso também significa combustível mínimo) de uma transferência entre duas órbitas circulares, em que se deseja apenas variação do semi-eixo maior e da inclinação do plano orbital. O autor faz a hipótese de baixo empuxo e começa com os resultados obtidos por Edelbaum (1961) para o problema de transferência em uma única revolução (com alcance limitado, em termos de semi-eixo maior e inclinação) e generaliza o caso de N revoluções (agora sem limites). A abordagem é a da utilização dos métodos convencionais de Controle Ótimo (Bryson e Ho, 1975 e Bryson, (1985), onde se busca a função ótima de controle (o ângulo entre a direção do empuxo aplicado e o plano orbital, e o momento de aplicação dos mesmos), pois os demais parâmetros são fixos.

Um problema comum a todas essas abordagens é que elas fornecem como solução uma trajetória nominal, que nunca pode ser seguida com precisão infinita. Uma das maneiras de se resolver esse problema é acoplar ao método escolhido um algoritmo, em tempo real, de correção do controle em função do erro acumulado, como o desenvolvido por Tapley e Fowler (1966).

O Problema de Três Corpos

A grande maioria dos trabalhos apresentados até o momento trata do problema com o uso da modelagem de dois corpos. O primeiro a utilizar o modelo de três corpos é provavelmente o trabalho feito po D'Amario em sua dissertação de doutorado (D'Amario, 1973), posteriormente transformado no artigo D'Amario e Edelbaum (1974). A teoria do "primer-vector" foi aplicada ao problema restrito de três corpos para obter uma transferência impulsiva ótima. O número de impulsos não é dado "a priori", mas sim encontrado pelas condições de otimalidade. O trabalho combina resultados analíticos com métodos numéricos. Essa mesma técnica foi posteriormente utilizada em Hiday e Howell (1992) em um problema de transferência entre órbitas "Halo", que são órbitas existentes no problema restrito de três corpos, quando formulado em três dimensões, e que permanecem aproximadamente em um plano perpendicular ao plano orbital dos dois primários. Maiores detalhes sobre esse tipo de órbita podem ser encontrados em Breakwell e Brown (1979), Richardson (1980) e Howell (1983). Também podem ser encontradas variantes tratando especificamente de transferências entre os pontos Lagrangeanos do sistema Terra-Lua e a Lua (Broucke, 1979).

Uma outra possibilidade aberta pela modelagem de três corpos é o uso de órbitas de transferência cíclicas. Nesse caso é utilizada uma órbita que faz com que o veículo espacial faça sucessivas passagens pelos dois corpos envolvidos na transferência, de modo a manter um sistema de transporte contínuo (pequenos veículos fazem o transporte da superfície até o encontro com o veículo transportador). Exemplos dessa linha de pesquisa são: Aldrin (1985) que explica os conceitos básicos desse sistema para transferências entre Terra-Lua e Terra-Marte; Uphoff e Crouch (1991) que estuda em mais detalhes o caso Terra-Lua; Sponaugle et. al. (1991) que estuda transferências cíclicas entre os pontos Lagrangeanos dos sistemas Terra-Lua e Terra-Marte.

Outra variante interessante, aberta pela modelagem de três corpos, é a demonstrada em Bond et. al. (1991) que utiliza o ponto Lagrangeano intermediário entre a Terra e a Lua como um nó intermediário de transferência.

O Problema de N-Corpos

A modelagem de missões espaciais como um problema de N-corpos é uma inovação recente. A grande motivação surgiu com a possibilidade de uma missão completa a todos os planetas dos sistema solar exterior com um único veículo explorador (como as missões Voyager I e II). Por essa razão, a maioria dos trabalhos foi desenvolvido nas duas últimas décadas e por um número reduzido de pesquisadores. Um dos primeiros trabalhos foi desenvolvido por Breakwell e Perko (1966), onde uma sucessão de cônicas heliocêntricas são combinadas para produzir uma trajetória completa. Mais tarde, D'Amario et al. (1979) desenvolveria um método para otimização de trajetórias com passagens próximas por vários corpos, baseado numa aproximação analítica do problema de três corpos feita por Wilson (1970) e aplicada ao problema em questão por Byrnes (1979). Esse mesmo método seria aperfeiçoado em D'Amario, Byrnes e Stanford (1981) com o objetivo de reduzir o tempo necessário ao cálculo da solução através de eliminação de funções de penalidade e substituição de variáveis. Depois disso, o custo para o veículo escapar do planeta original e ser inserido no planeta final seria acrescentado ao modelo em D'Amario, Byrnes e Stanford (1982). Usando esses procedimentos, várias missões foram estudadas: uma missão Galileo visitando o cometa de Halley e Júpiter (Byrnes e D'Amario, 1982); uma missão Galileo indo direto a Júpiter (D'Amario e Byrnes, 1983); missões Galileo indo a vários asteróides e cometas (Byrnes e D'Amario, 1983).

Conclusões

O problema da transferência de órbitas para um veículo espacial foi definido e as diversas modelagens de dinâmica, atuadores e métodos de otimização foram descritos.

A literatura disponível foi estudada, e mais de uma centena de referências foram apresentadas com comentários. As transferências mais utilizadas foram descritas em maiores detalhes.

Agradecimentos

Os autores agradecem o Instituto Nacional de Pesquisas Espaciais pelo suporte durante o desenvolvimento desse trabalho e o CNPq (Conselho de Desenvolvimento Científico e Tecnológico) pelo suporte financeiro fornecido através da bolsa de estudo.

Referências

Aldrin, B., 1985, "Cyclic trajectory concepts", SAIC presentation to the interplanetary rapid transit meeting, Pasadena, CA, EUA.

Barrar, R. B., 1963, "An analytic proof that the Hohmann-type transfer is the true minimum two-impulse transfer", Astronautica Acta, Vol. 9, pp 1-11.

Battin, R. H. e Vaughan, R. M., 1984, "An elegant Lambert algorithm", Journal of Guidance, Control, and Dynamics, Vol. 7, pp. 662-670.

Bell, D. J., 1968, "Optimal space trajectories - a review of published work", The Aeronautical Journal of the Royal Aeronautical Society, vol. 72, pp. 141-146.

Bender, D. F., 1962, "Optimal coplanar two-impulse transfers between elliptic orbits", Aerospace Engineering, pp. 44-52.

Biggs, M. C. B., 1978, "The optimisation of spacecraft orbital manoeuvres. Part I: Linearly varying thrust angles", The Hatfield Polytechnic Numeric Optimisation Centre.

Biggs, M. C. B., 1979, "The optimisation of spacecraft orbital manoeuvres. Part II: Using Pontryagin's maximum principle", The Hatfield Polytechnic Numerical Optimisation Centre.

Billik, B. H. e Roth, H. L., 1967, "Studies relative to rendezvous between circular orbits", Astronautica Acta, Vol. 13, pp. 23-36.

Bond, V.R., Sponaugle, S. J., Fraietta, M. F. e Everett, S. F., 1991, "Cislunar libration point as a transportation node for lunar exploration", AAS paper 91-103, AAS/AIAA Spaceflight Mechanics Meeting, Houston, TX, EUA.

Breakwell, J. V. e Brown, J. V., 1979, "The 'Halo' family of 3-dimensional periodic orbits in the Earth-Moon restricted 3-body problem", Celestial Mechanics, Vol. 20, pp 389-404.

Breakwell, J. V. e Perko, L. M., 1966 "Matched asymptotic expansions, pathed conics the the computation of interplanetary trajectories", AIAA Progress in Astronautics and Aeronautics: Methods in Astrodynamics and Celestial Mechanics, edited by R. L. Duncombe and V. G. Szebehely, Academic Press, New York, Vol. 17, pp. 159-182

Brookes, C. J. e Smith, J., 1970, "Optimal rocket trajectories in a general force-field", Astronautica Acta, Vol. 15, pp. 129-132.

Broucke, R. A., 1979, "Traveling between the Lagrange points and the Moon", Journal of Guidance, Control, and Dynamics, Vol. 2, pp. 257-263.

Broucke, R. A., 1988, "The celestial mechanics of gravity assist", AIAA papel 88-4220, AIAA/AAS Astrodynamics Conference, Minneapolis, MN, EUA.

Broucke, R. A., 1991, "Low-thrust trajectories optimization in and inverse square force field", AAS paper 91-159, AAS/AIAA Spaceflight Mechanics Meeting, Houston, TX, EUA.

Broucke, R. A. e Prado A. F. B. A., 1993a, "Jupiter swing-by trajectories passing near the Earth", AAS paper 93-117, AAS/AIAA Spaceflight Mechanics Meeting, Pasadena, CA, EUA.

Broucke, R. A. e Prado, A. F. B. A., 1993b, "Optimal N-impulse transfer between coplanar orbits", AAS/AIAA Astrodynamics Conference, Victoria, BC, Canada.

Bryson, A. E. e Ho, Y. C., 1975, "Applied optimal control", Wiley, New York, NY, EUA.

Bryson, A. E., 1985, "New concepts in control theory, 1959-1984", Journal of Guidance, Control, and Dynamics, Vol. 8, pp. 417-425.

Byrnes, D. V., 1979, "Application of the pseudostate theory to the three-body Lambert problem", AAS paper 79-163, ASS/AIAA Astrodynamics Specialists Conference, Provincetown, MA, EUA.

Byrnes, D. V. e D'Amario, L. A., 1982, "A combined Halley flyby mission" AIAA paper 82-1462, AIAA/AAS Astrodynamics Conference, San Diego, CA, EUA.

Byrnes, D. V. e D'Amario, L. A., 1983, "Asteroid/comet mission possibilities using a Galileo spacecraft", AAS paper 83-309, Astrodynamics Conference, Lake Placid, NY, EUA.

Carter, T. E., 1984, "Fuel-optimal maneuvers of a spacecraft relative to a point in circular orbit", Journal of Guidance, Control, and Dynamics, Vol. 7, pp. 710-716.

Ceballos, D. C., 1980, "Aproximações sub-ótimas para o controle em programas dinâmicos de otimização", Dissertação de Mestrado, Instituto Nacional de Pesquisas Espaciais, São José dos Campos, SP, Brasil.

Ceballos, D. C. e Rios Neto, A., 1981, "Linear programming and suboptimal solutions of dynamical systems control problems", Proceedings of the International Symposium on Spacecraft Flight Dynamics, pp. 239-244, Darmstadt, Federal Republic of Germany.

Contensou, P., 1962, "Etude théorique de trajectoires optimales dans un champ de gravitation. Application au cas d'un centre d'attraction unique", Astronautica Acta, Vol. 8, pp. 134-150.

Culp, R. D., 1967, "Contensou-Busemann conditions for optimal coplanar orbit transfer", AIAA Journal, Vol. 5, pp. 371-372.

D'Amario, L. A., 1973, "Minimum impulse three body trajectories", Ph.D. Dissertation, MIT, Cambridge, MA, EUA.

D'Amario, L. A., Byrnes, D. V., Sackett, L. L. e Stanford, R. H., 1979, "Optimization of multiple-flyby trajectories", AAS paper 79-162, AAS/AIAA Astrodynamics Specialists Conference, Provincetown, MA, EUA.

D'Amario, L. A., Byrnes, D. V. e Stanford, R. H., 1981, "A new method for optimizing multiple-flyby trajectories", Journal of Guidance, Control and Dynamics, Vol. 4, pp 591-596.

D'Amario, L. A., Byrnes, D. V. e Stanford, R. H., 1982, "Interplanetary trajectory optimization with application to Galileo", Journal of Guidance, Control, and Dynamics, Vol. 5, pp. 465-471.

D'Amario, L. A. e Byrnes D. V., 1983, "Interplanetary trajectory design for the Galileo mission", AIAA paper 83-0099, AIAA 21st Aerospace Sciences Meeting, Reno, NV, EUA.

D'Amario, L. A. e Edelbaum, T. N., 1974, "Minimum impulse three-body trajectories", AIAA Journal, Vo. 12, pp. 455-462.

Denham, W. F. e Bryson, A. E., 1964, "Optimal programming problems with inequality contrants II: Solution by steepest-ascent", AIAA Journal, Vol. 2, pp. 25-34.

Eckel, K. G., 1962, "Optimum transfer between non-coplanar elliptical orbits", Astronautica Acta, Vol. 8, pp. 177-192.

Eckel, K. G., 1963, "Optimum transfer in a central force field with n impulses", Astronautica Acta, Vol. 9, pp. 302-324.

Eckel, K. G., 1982, "Optimal impulsive transfer with time contraint", Astronautica Acta, Vol. 9, pp. 139-146.

Eckel, K. G. e Vihn, N. X., 1984, "Optimal switching conditions for minimum fuel fixed time transfer between non coplanar elliptical orbits", Astronautica Acta, Vol. 11, pp. 621-631.

Eckenwiler, M. W., 1965, "Closed-form Lagrangian multipliers for coast periods of optimum trajectories", AIAA Journal, Vol. 3, pp. 1149-1151.

Edelbaum, T. N., 1961, "Propulsion requirements for controllable satellites", American Rocket Society Journal, Vol. 31, pp. 1079-1089.

Erno, 1984, "Orbit manoeuvers with finite thrust", ESA Report.

Fernandes, S. S., 1986, "Efeito do achatamento da Terra sobre transferência impulsional ótima", Dissertação de Mestrado, Instituto Tecnológico da Aeronautica, São José dos Campos, SP, Brasil.

Fernandes, S. S., 1989, "Earth oblateness effect on the optimal impulsive transfer between close orbits. Part 2: singular solutions", Acta Astronautica, Vol. 19, pp. 393-399.

Fernandes, S. S. e Moraes, R. V., 1989, "Earth oblateness effect on the optimal impulsive transfer between close orbits. Part 1: nonsingular solutions", Acta Astronautica, Vol. 19, pp. 281-285.

Fernandes, S. S. e Sessin, W., 1989, "Optimal low-thrust power transfer between neighbouring quasi-circular orbits of small inclinations around an oblate planet", Acta Astronautica, Vol. 19, pp. 401-409.

Gobetz, F. W. e Doll, J. R., 1969, "A survey of impulsive trajectories", AIAA Journal, Vol. 7, pp. 801-834.

Goddard, R. H., 1919, "A method of reaching extreme altitudes", Smithsonian Inst. Publ. Misc. Collect. Vol. 71.

Gross, L. R. e Prussing, J. E., 1974, "Optimal multiple-impulse direct ascent fixed-time rendezvous", AIAA Journal, Vol. 12, pp. 885-889.

Handelsman, M., 1966, "Optimal free-space fixed-thrust trajectories using impulsive trajectories as starting iteratives", AIAA Journal, Vo. 4, pp. 1077-1082.

Hazelrigg Jr., G. A., 1984, "Globally optimal impulsive transfer via Green's theorem", Journal of Guidance, Control, and Dynamics, Vol. 7, pp 462-470.

Hempel, P. R., 1966, "Representation of the Lagrangian multipliers for coast periods of optimum trajectories", AIAA Journal, Vol. 4, pp. 729-730.

Hiday, L. A. e Howell, K. C., 1992, "Impulsive time-free transfers between Halo orbits", AIAA paper 92-4580, AIAA/AAS Astrodynamics Conference, Hilton Head, SC, EUA.

Hoelker, R. F. e Silber, R., 1959, "The bi-elliptic transfer between circular co-planar orbits", Alabama, Army Ballistic Missle Agency, Redstone Arsenal, EUA.

Hohmann, W., 1925, "Die erreichbarkeit der himmelskörper", Oldenburg, Munique, Alemanha.

Howell, K. C., 1983, "Effects of eccentricity on Halo orbits in the restricted three-body problem", AAS paper 83-335.

Jezewski, D. J. e Rozendaal, H. L., 1968, "An efficient method for calculating optimal free-space N-impulsive trajectories", AIAA Journal, Vol. 6; pp. 2160-2165.

Kopp, R. E. e Moyer, H. G., 1965, "Necessary conditions for singular extremals", AIAA Journal, Vol. 3, pp. 1439-1444.

Lawden, D. F., 1953, "Minimal rocket trajectories", ARS Journal, Vol. 23, pp. 360-382.

Lawden, D. F., 1954, "Fundamentals of space navigation", JBIS, Vol. 13, pp. 87-101.

Lawden, D. F., 1955, "Optimal programming of rocket thrust direction", Astronautical Acta, Vol. 1, pp. 41-56.

Lawden, D. F., 1962, "Optimal intermediate-thrust arcs in a gravitational field", Astronautical Acta, Vol. 8, pp. 106-123.

Lion, P. M. e Handelsman, M., 1968, "Primer vector on fixed-time impulsive trajectories", AIAA Journal, Vol. 6, pp. 127-132.

Marchal, C., 1965, "Transferts optimaux entre orbites elliptiques coplanaires (Durée indifférente)", Astronautica Acta, Vol. 11, pp. 432-445.

Marec, J. P., 1968, "Transferts impulsionnels, economiques, entre orbites quasi-circulaires, proche, non coplanaires", Astronautica Acta, Vol. 15, pp. 47-55.

Marec, J. P., 1979, "Optimal Space Trajectories", Elsevier, New York, NY, EUA.

Matogawa, Y., 1983. "Optimum low thrust transfer to geosynchronous orbit", Astronautica Acta, Vol. 10, pp. 467-478.

May, D. H., 1986, "An energy approach for orbital transfers", Journal of Guidance, Control, and Dynamics, Vol. 9, pp. 23-26.

McCue, G. A., 1963, "Optimum two-impulse orbital transfer and rendezvous between inclined elliptical orbits", AIAA Journal, Vol. 1, pp. 1865-1872.

McGue, G. A., 1967, "Quasilinearization determination of optimum finite-thrust orbital transfers", AIAA Journal, Vol. 5, pp. 755-763.

Melton, R. G. e Jin, H., 1991, "Transfers between circular orbits using fixed impulses", AAS paper 91-161, AAS/AIAA Spaceflight Mechanics Meeting, Houston, TX, EUA.

Moskowitz, S. E., 1963, "On the accuracy of approximate thrust steering schedules in optimal correction maneuvers", Astronautica Acta, Vol. 9, pp. 20-30.

Moyer, H. G, 1965, "Minimum impulse coplanar circle-ellipse transfer", AIAA Journal, Vol. 3, pp. 723-726.

Pines, S., 1964, "Constants of the motion for optimum thrust trajectories in a central force field", AIAA Journal, Vol. 2, pp, 2010-2014.

Prado, A. F. B. A., 1989, "Análise, seleção e implementação de procedimentos que visem manobras ótimas de satélites artificiais". Dissertação de Mestrado, Intituto Nacional de Perquisas Espaciais (INPE), São José dos Campos, SP, Brasil.

Prado, A. F. B. A., 1990, "Earth-moon trajectories for the lunar polar orbit mission", IAF paper ST-90-016, International Astronautical Congress, 41 st, Dresden, Federal Republic of Germany.

Prado, A. F. B. A. e Broucke, R. A., 1993, "The problem of transfer orbits from one body back to the same body", AAS paper 93-183, AAS/AIAA Spaceflight Mechanics Meeting, Pasadena, CA, EUA.

Prussing, J. E., 1969, "Optimal four-impulse fixed-time rendezvous in the vicinity of a circular orbit", AIAA Journal, Vol. 7, pp. 928-935.

Prussing, J. E., 1970, "Optimal two- and tree-impulse fixed-time rendezvous in the vicinity of a circular orbit", AIAA Journal, Vol. 8, pp. 1221-1228.

Prussing, J. E. e Chiu, J. H,, 1986, "Optimal multiple-impulse time-fixed rendezvous between circular orbits", Journal of Guidance, Control, and Dynamics, Vol. 9, pp. 17-22.

Pu, C. L. e Edelbaum, T. N., 1975, "Four-body trajectory optimization", AIAA Journal, Vol. 13, pp. 333-336.

Redding, D. C., 1984, "Highly efficiente, very low thrust transfer to geosynchronous orbit: exact and approximate solutions", Journal of Guidance, Control, and Dynamics, Vol. 7, pp. 141-147.

Redding, D. C. e Breakwell, J. V., 1984, "Optimal low-thrust transfers to synchronous orbit", Journal of Guidance, Control, and Dynamics, Vol. 7, pp. 148-155.

Richardson, D. L., 1980, "Halo orbit formulation for the ISEE-3 mission", Journal of Guidance, Control, and Dynamics, Vol. 3, pp. 543-548.

Rios Neto, A. e Bambace, L. A. W., 1981, "Optimal linear estimation and suboptimal numerical solutions of dynamical systems control problems", Proceedings of the International Symposium on Spacecraft Flight Dynamics, pp. 233-238, Darmstadt, Federal Republic of Germany.

Robbins, H. M., 1965, "Optimality of intermediate-thrust arcs of rocket trajectories", AIAA Journal, Vol. 3, pp. 1094-1098.

Robbins, H. M., 1966, "An analytical study of the impulsive approximation", AIAA Journal, Vol. 4, pp. 1417-1423.

Roth, H. L., 1967, "Minimization of the velocity increment for a bi-elliptic transfer with plane change", Astronautica Acta, Vol. 13, pp. 119-130.

Smith, G. C., 1959, "The calculation of minimal orbits", Astronautica Acta, Vol. 5, pp. 253-265.

Spencer, T. M., Glickman, R. e Bercaw, W., 1982, "Low thrust orbit raising for Shuttle payloads", Journal of Guidance, Control, and Dynamics, Vol. 5, pp. 372-378.

Sponaugle, S. J., Rishikof, B. H., Davis, S. F., Pesek, D. A., Walyus, D. R. e Bond, V. R., 1991, "Optimal cycling between cislunar and cismartian libration points with reusable nuclear electric transfer vehicles", AAS paper 91-104, AAS/AIAA Spaceflight Mechanics Meeting, Houston, TX, EUA.

Stern, S. A., 1984, "A rectilinear guidance strategy for short orbital transfers", Journal of Spacecrafts and Rockets, Vol. 21, pp. 542-545.

Subrahmanyam, M. B., 1986, "Computation of optimal controls by Newton's method using a discretized Jacobian", Journal of Guidance, Control, and Dynamics, Vol. 9, pp. 371-374.

Szebehely, V. G., 1965, "Special orbits for the exploration of Mars and Venus", Conference on "The exploration of Mars and Venus", Virginia Polytechnic Institute, Blacksburg, VA, EUA.

Szebehely, V. G., 1967, "Theory of orbits", Academic Press, New York, EUA.

Tapley, B. D. e Fowler, W. T., 1966, "Terminal guidance for continuous powered space vehicles", AIAA Journal, Vol. 4, pp. 1683-1684.

Ting, L., 1960, "Optimal orbital transfer by several impulses", Astronautica Acta, Vol. 6, pp. 256-265.

Tomita, K. e Feiring, B. R., 1985, "Trajectory optimization for maneuvering satellites", Systems and Control Letters, Vol. 5, pp. 223-228.

Tsien, H. S., 1953, "Take-off from satellite orbit", Journal of the American Rocket Society, Vol. 23, pp. 233-236.

Uphoff, C. e Crouch, M. A., 1991, "Lunar cycler orbits with alternating semi-monthly transfer windows", AAS paper 91-105, AAS/AIAA Spaceflight Mechanics Meeting, Houston, TX, EUA.

Vinh, N. X., 1972, "Integration of the primer vector in a central force field", Journal of the Optimization Theory and Applications, Vol. 9, pp. 51-58.

Yablon'Ko, Y. P., 1982, "Optimal control in orbital rendezvous", Kosmicheskie Issledovaniya, Vol. 20, pp. 499-504.

Weib, J., 1985, "Orbit manoeuvres with finite thrust", ESA Journal, Vol. 9, pp. 49-63.

Weisel, W. E. e Alfano, S., 1985, "Optimal many-revolution orbit transfer", Journal of Guidance, Control, and Dynamics, Vol. 8, pp. 155-157.

Wilson, S. W., 1970, "A pseudostate theory for the approximation of three-body trajectories", AIAA paper 70-1061, AIAA Astrodynamics Conference, Santa Barbara, CA, EUA.

Wolfsberger, W., Weib, J. e Rangnitt, D., 1983, "Strategies and schemes for rendezvous on geostationary transfer orbit", Astronautica Acta, Vol. 10, pp. 527-538.

Zee, C. H., 1963, "Effect of finite thrusting time in orbital maneuvers", AIAA Journal, Vol. 1, pp. 60-64.

Zondervan, K. P., Wood, L. J. e Caughey, T. K., 1984, "Optimal low-thrust, three-burn orbit transfers with plane changes", The Journal of The Astronautical Sciences, Vol. 32, pp. 407-427.

RBCM - J. of the Braz. Soc. Mechanical Sciences
Vol. XV - nº 1 - 1993 - pp. 79-87

ISSN 0100-7386
Printed in Brazil

Simulação Numérica de Escoamentos Turbulentos atrás de Grelhas com o Modelo K-ε e com uma Equação para Prever Flutuações de Temperatura

Numerical Simulation in Grid-Generated Turbulent Flows with the K-ε Model and one Equation for the Temperature Fluctuations

Gilmar Mompean Munhoz da Cruz
Departamento de Energia, FEM, UNICAMP

Sumário

Neste trabalho apresenta-se um modelo de turbulência de três equações para a determinação de grandezas turbulentas, como as flutuações de temperatura, energia cinética de turbulência e sua taxa de dissipação. As equações de conservação são discretizadas pelo método dos volumes finitos. O modelo é comparado com resultados experimentais de dois tipos de escoamentos turbulentos de ar atrás de grelha. O primeiro, turbulência homogênea isotérmica atrás de grelhas (Warhaft e Lumley, 1978), permitiu validar o modelo em configurações com temperatura média constante. O segundo, com gradiente de temperatura (Sirivat e Warhaft, 1982), permitiu validar o modelo nas situações onde o termo de produção das flutuações de temperatura, devido ao gradiente de temperatura, é importante.

Palavras-chave: Turbulência - Escoamento atrás de Grelhas - Flutuação de Temperatura - Modelo k-ε.

Abstract

In order to predict the temperature fluctuations in turbulent flows, we have used a turbulence model with three transport equations for mean square temperature variance, turbulent kinetic energy and the rate of kinetic energy dissipation. The governing field equations are the Navier-Stokes, continuity and energy equations. The finite volume method is employed to solve numerically these equations. The results of calculations with this model are compared with the measures of two experiments. The first one, an homogeneous hot turbulence below a grid (Warhaft and Lumley, 1978), allows us to test the model in a configuration with a constant mean temperature. The second experiment, a grid turbulence with cross-stream temperature gradient (Sirivat e Warhaft, 1982), allows us to test the model in a situation where the generation rate term of $\overline{\theta}^2$ due to mean temperature gradient plays an important part.

Keywords: Turbulence - Grid-generated flows - Temperature Fluctuations - k-ε model.

Introdução

Afim de prever as flutuações de temperatura em escoamentos turbulentos, foi desenvolvido um modelo de turbulência com três equações de transporte para a variância da flutuação de temperatura ($\overline{\theta^2}$), energia cinética de turbulência (k) e a taxa de dissipação de energia cinética (ε). O fluido é considerado incompressível e Newtoniano. As propriedades viscosidade, condutividade térmica e calor específico são consideradas constantes. Para a densidade, foi considerada a sua dependência com a temperatura utilizando a aproximação de Boussinesq. Para tratar o escoamento turbulento, a velocidade, pressão e temperatura são decompostas em partes médias e flutuantes nas equações de Navier-Stokes, continuidade e energia. O tensor de Reynolds é determinado, utilizando a viscosidade turbulenta com o modelo k-ε. Os fluxos de calor turbulento, são determinados usando uma difusividade turbulenta com um valor constante para o número de Prandtl turbulento. A equação para a flutuação de temperatura é "fechada" com a lei do primeiro gradiente para os termos de difusão turbulenta. A relação entre as escalas de tempo da turbulência térmica e hidrodinâmica é empregada na determinação da taxa de dissipação das flutuações de temperatura. O método dos volumes finitos é utilizado para resolver numericamente esse sistema de equações diferenciais. Todas as grandezas escalares são tratadas no centro dos volumes de controle e as velocidades são localizadas no centro das faces do volume de controle; esta escolha é o princípio da malha entrelaçada. As equações são discretizadas no tempo na forma semi-implícita. Este método é derivado do método SOLA desenvolvido por Hirt,

Manuscript received March 1993. Associate Technical Editor: Agenor de Toledo Fleury

Nichols e Romero (1975). O código usado é o TRIO:VF/CEA, e o computador foi um CRAY-1. Os resultados desse modelo foram comparados com medidas de duas experiências. A primeira, turbulência homogênea atrás de grelhas (Warhaft e Lumley, 1978), permitiu testar o modelo numa configuração de temperatura média constante. A segunda, escoamento atrás de grelha com gradiente de temperatura cruzado (Sirivat e Warhaft, 1982), permitiu testar o modelo numa situação onde os termos de produção de flutuação de temperatura são importantes.

Equações de Transporte das Grandezas Médias

O fluido é considerado incompressível e Newtoniano. No que concerne as propriedades físicas, considera-se a viscosidade, condutividade térmica e o calor específico como constantes. Para a densidade prevê-se sua dependência da temperatura a partir da aproximação de Boussinesq:

$$\rho(T)=\rho^{\circ}-\rho^{\circ}\beta(T-T^{\circ}) \tag{1}$$

onde ρ° representa a densidade na temperatura de referência (T°) e β o coeficiente de expansão volumétrica.

As variações da densidade são levadas em consideração somente no termo de força de volume da equação da quantidade de movimento.

A fim de tratar o escoamento turbulento usa-se a decomposição de Reynolds, que iguala as variáveis instantâneas, velocidade (U), temperatura (T) e pressão (P) à soma de um valor médio e um valor flutuante:

$$U_i=\bar{U}_i+u_i \ ; \quad P=\bar{P}+p \quad ; \quad T=\bar{T}+\theta \tag{2}$$

$\bar{U}$, $\bar{P}$ e $\bar{T}$ representam os valores médios das componentes instantâneas e u, p e θ as componentes flutuantes.

Aplicando-se essa decomposição para as variáveis em questão nas equações locais instantâneas, obtem-se as seguintes equações de conservação para as grandezas médias.

Conservação da massa

$$\frac{\partial \bar{U}_i}{\partial x_i}=0 \tag{3}$$

Conservação da quantidade de movimento

$$\frac{\partial \bar{U}_i}{\partial t}+\frac{\partial}{\partial x_j}(\overline{\bar{U}_i\bar{U}_j})=-\frac{\partial \bar{P}}{\rho^0 \partial x_i}+\frac{\partial}{\partial x_j}(\nu\frac{\partial \bar{U}_i}{\partial x_j}-\overline{u_iu_j})+g_i(1-\beta(\bar{T}-\bar{T}^{\circ})) \tag{4}$$

Conservação de energia

$$\frac{\partial \bar{T}}{\partial t}+\frac{\partial}{\partial x_i}(\overline{\bar{U}_i\bar{T}})=\frac{\partial}{\partial x_i}(\alpha\frac{\partial \bar{T}}{\partial x_i}-\overline{u_i\theta}) \tag{5}$$

Esse sistema de equações apresenta duas novas incógnitas, o tensor de Reynolds ($\overline{u_iu_j}$) e o fluxo de calor turbulento ($\overline{u_i\theta}$). O tensor de Reynolds será determinado com o modelo de turbulência hidrodinâmico k-ε. O modelo que emprega o conceito de número de Prandtl turbulento será utilizado na determinação do fluxo de calor turbulento.

Modelo de Turbulência para a Hidrodinâmica

Para a determinação do tensor de Reynolds foi utilizada a hipótese da viscosidade turbulenta (ν_t). Nessa modelagem postula-se a proporcionalidade entre o tensor de Reynolds e o tensor de deformação média (D), com ajuda da viscosidade turbulenta:

$$u_iu_j=\nu_tD-2/3k\delta_{ij} \qquad (6)$$

sendo

$$D=\frac{\partial\overline{U}_i}{\partial x_j}+\frac{\partial\overline{U}j}{\partial x_i}$$

A viscosidade turbulenta é determinada a partir do modelo k-ε, onde k é a energia cinética de turbulência e ε a sua taxa de dissipação:

$$\nu_t=C_\mu\frac{k^2}{\varepsilon}\text{, onde } C_\mu=0{,}09 \qquad (7)$$

Energia cinética de turbulência (k)

A equação da energia cinética de turbulência na forma diferencial modelada é escrita como (Rodi, 1978) :

$$\frac{Dk}{Dt}=\frac{\partial}{\partial x_j}\left(\frac{\nu_t}{Pr_k}\frac{\partial k}{\partial x_j}\right)+P+G-\varepsilon \qquad (8)$$

$$P=-\overline{u_iu_j}\frac{\partial\overline{U}_i}{\partial x_j} \quad ; \quad G=-\beta g_i\overline{u_i\theta} \quad \text{e} \quad Pr_k=1{,}0$$

P representa a produção de energia cinética turbulenta devido aos gradientes de velocidade e G a produção de energia cinética devido às forças de volume.

Taxa de dissipação de k (ε)

A equação da taxa de dissipação da energia cinética de turbulência é utilizada na seguinte forma (Rodi, 1978):

$$\frac{D\varepsilon}{Dt}=\frac{\partial}{\partial x_j}\left(\frac{\nu_t}{Pr_\varepsilon}\frac{\partial\varepsilon}{\partial x_j}\right)+\text{Fonte }(\varepsilon) \qquad (9)$$

$$\text{Fonte }(\varepsilon)=C_{\varepsilon1}(1+C_{\varepsilon3}R_f)(P+G)\frac{\varepsilon}{k}-C_{\varepsilon2}\frac{\varepsilon^2}{k}$$

com $Pr_\varepsilon=1{,}3$; $C_{\varepsilon1}=1{,}44$; $C_{\varepsilon2}=1{,}92$; $C_{\varepsilon3}=0{,}8$ e R_f é o número de Richardson

Nomenclatura

B = passo da grelha colocada no túnel de vento
C = constantes dos modelos
D = tensor de deformação
G = produção de k devido aos efeitos de empuxo
k = energia cinética de turbulência
P = produção da energia cinética de turbulência
Pr_t = número de Prandtl turbulento
Pr_k = constante da equação de k
R = razão entre as escalas de tempo da turbulência térmica e da turbulência hidrodinâmica
R_f = número de Richardson turbulento, -G/(*P*+G)
Z = coordenada vertical
α_t = difusividade turbulenta
ε = dissipação de k
ν_t = viscosidade turbulenta
$\overline{u_iu_j}$ = tensor de Reynolds
$\overline{u_i\theta}$ = fluxo de calor turbulento
$\overline{\theta^2}$ = variância das flutuações de temperatura
P_θ = produção de $\overline{\theta^2}$
ε_θ = dissipação de $\overline{\theta^2}$
τ = escala de tempo da turbulência hidrodinâmica
τ_θ = escala de tempo da turbulência térmica

Modelo de Turbulência para a Parte Térmica

Para a determinação do fluxo de calor turbulento, a hipótese da difusividade térmica turbulenta é empregada. Essa difusividade é determinada a partir de um número de Prandtl constante Pr_t:

$$\overline{u_i\theta}=-\alpha_t\frac{\partial\overline{T}}{\partial x_i}\text{, onde } \alpha_t=\frac{\nu_t}{Pr_t} \qquad (10)$$

Frequentemente, o valor 0,9 é utilizado para Pr_t.

Equação da flutuação de temperatura:

A equação para a variância da flutuação de temperatura é obtida a partir da equação da energia, com a decomposição de Reynolds, pela diferença entre as formas instantânea e média:

$$\frac{D\overline{\theta^2}}{Dt}=\frac{\partial}{\partial x_j}(\alpha\frac{\partial\overline{\theta^2}}{\partial x_j}-\overline{u_j\theta^2})-2\overline{u_j\theta}\frac{\partial\overline{T}}{\partial x_j}-2\alpha\overline{\frac{\partial\theta}{\partial x_j}\frac{\partial\theta}{\partial x_j}} \qquad (11)$$

1 2 3 P_θ ε_θ

Os termos acima possuem os seguintes significados:

1 Termo transiente e convectivo do campo de velocidade média

2 Difusão molecular

3 Difusão devida à convecção turbulenta

P_θ Produção pelo gradiente de temperatura média

ε_θ Dissipação das flutuações de temperatura

Como estamos testando o modelo para escoamentos em regime turbulento, estamos trabalhando com grandes números de Reynolds (~10.000), então o termo de difusão molecular pode ser desprezado (Cruz, 1989). O termo de difusão devido a convecção turbulenta é modelado a partir da lei do primeiro gradiente:

$$-\overline{u_j\theta^2}=C_\theta\frac{k^2}{\varepsilon}\frac{\partial\overline{\theta^2}}{\partial x_j} \qquad (12)$$

O valor aqui empregado para C_θ é 0,13 (Spalding, 1971).

Com as hipóteses acima, a equação para a variância da flutuação de temperatura a ser resolvida é:

$$\frac{D\overline{\theta^2}}{Dt}=\frac{\partial}{\partial x_j}(C_\theta\frac{k^2}{\varepsilon}\frac{\partial\overline{\theta^2}}{\partial x_j})-2\overline{u_j\theta}\frac{\partial\overline{T}}{\partial x_j}-2\varepsilon_\theta \qquad (13)$$

O termo de dissipação das flutuações de temperatura é aqui modelado a partir da relação entre o tempo de decaimento de turbulência térmica e o tempo de decaimento da turbulência hidrodinâmica. Por definição essa relação pode ser expressa como:

$$R=\frac{\tau_\theta}{\tau}=\frac{\overline{\theta^2}}{2\varepsilon_\theta}\frac{\varepsilon}{k} \qquad (14)$$

Vários trabalhos foram realizados no sentido de determinar o valor do fator R a partir de escoamentos atrás de grelhas. Em (Warhaft e Lumley, 1978) encontra-se uma revisão dos valores obtidos por diversos autores, em escoamentos atrás de grelha aquecida. Eles mostram que os valores do fator R encontrados podem variar de 0,4 a 1,6 para os casos estudados.

Nesse trabalho vamos mostrar uma análise de sensibilidade numérica do valor do fator R, dentre os valores utilizados usualmente, no nível da variância da flutuação de temperatura.

Tratamento Numérico:

Para a discretização espacial das equações de conservação emprega-se o método dos volumes finitos. Essas equações são integradas sobre um volume de controle e aplica-se o teorema de Gauss para a transformação das integrais de volume em integrais de superfície. As grandezas escalares, temperatura, pressão, energia de turbulência (k) e a sua taxa de dissipação (ε), são tratadas no centro dos volumes de controle. As grandezas vetoriais, velocidades e fluxo de calor turbulento, são localizadas no centro das faces dos volumes de controle. Essa escolha de localização das variáveis constitui o princípio da malha entrelaçada. Para a discretização temporal o método SOLA, (Hirt et al., 1975) é empregado. Esse é um método de discretização semi-implícito para o termo de gradiente de pressão na equação de conservação da quantidade de movimento. Para as equações da energia, de k e ε, o esquema de discretização é explicito. Esse método numérico está mostrado em detalhes em (Cruz, 1989).

O código de cálculo usado foi o TRIO/VF do Centre d' Études Nucleaires de Grenoble (CENG), e o computador foi um CRAY-1. A malha utilizada para os cálculos é composta de 31 pontos na direção horizontal e 32 pontos na direção vertical.

Resultados e Comentários:

Esse modelo é aplicado para dois tipos de configurações: a) escoamento turbulento de ar isotérmico atrás de uma grelha, b) escoamento de ar atrás de uma grelha com gradiente de temperatura. As comparações dos resultados, entre valores obtidos pelo modelo com as medidas experimentais, serão realizados para o regime permanente, apesar do modelo permitir a simulação do regime transiente.

A primeira experiência (a) utiliza uma grelha com um passo B=2,54 cm, colocada no interior de um tunel de vento vertical. A secção de teste tem um comprimento de 167B e uma área de 16Bx16B. A velocidade média do ar é de 6,5 m/s. O número de Reynolds, baseado no passo da grelha, é de 10.000. A porosidade da grelha é 0,66, constituída de barras quadradas de 0,476x0,476 cm. Os valores obtidos experimentalmente são fornecidos por Warhaft e Lumley (1978). Entre as várias medidas experimentais fornecidas por Warhaft e Lumley, dois casos foram selecionados para a comparação com o modelo. O primeiro caso com uma temperatura média do ar de 300 K e o segundo com uma temperatura de 308 K.

Para essas configurações foram utilizadas quatro tipos de condições limites. Na entrada do domínio computacional (Z/B=80), foram impostos os valores medidos experimentalmente para a velocidade, temperatura e grandezas turbulentas. No centro do tunel foi utilizada a condição de simetria. A direita foi imposta uma parede adiabática. Na saída do domínio foi fornecida a pressão atmosférica. A Fig. 1 mostra essas posições:

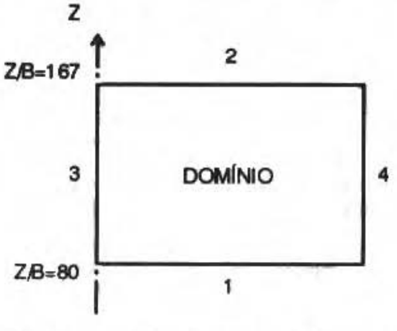

1 Velocidade e grandezas escalares impostas (T, k e ε)
2 Pressão atmosférica
3 Simetria
4 Parede adiabática

Fig. 1 Posição das condições limites

Para essa experiência, os termos de produção P (devido aos gradientes de velocidade) e G (devido as forças de volume) são nulos. Então, os termos devido à convecção e a difusão apresentam um papel importante no balanço das equações de k (8) e de ε (9). A ausência de gradiente de temperatura, permite validar o modelo para o caso onde somente os termos de transporte e dissipação são considerados na equação da flutuação de temperatura (13). Os valores utilizados para o fator R no modelo numérico são valores encontrados experimentalmente por Warhaft e Lumley (1978).

Para a segunda experiência (b), foram utilizados os valores obtidos experimentalmente por Sirivat eWarhaft (1982), que utilizaram a mesma geometria da experiência anterior. A única diferença, da segunda com a primeira, foi a imposição de um gradiente de temperatura na grelha. Esse gradiente foi obtido aquecendo-se diferentemente as barras da grelha. Para efeito de comparação entre o cálculo e as medidas, foi selecionado o ensaio com velocidade do ar de 3,4 m/s (número de Reynolds de 5200) e o gradiente de temperatura de 8,1 K/m.

A Fig. 2 fornece os resultados da comparação entre o modelo utilizado e as medidas experimentais para a flutuação de temperatura na primeira experiência. Essas curvas mostram o excelente acordo existente entre cálculo e medidas. O desvio máximo entre cálculo e medidas está em torno de 5% na região de saída do domínio (Z/B=165) para o caso de T=308 K. Pode-se salientar que o único inconveniente é a utilização de valores diferentes de R (obtidos experimentalmente) em função da temperatura, R=0,95 para T=308 K e R=1,05 para T=300 K.

A seguir apresentam-se os resultados obtidos para a segunda experiência. Nessa experiência todos os termos das equação (13) da flutuação de temperatura, convecção, difusão e produção devido ao gradiente de temperatura apresentam valores não desprezíveis. A Fig. 3 mostra os resultados obtidos com a equação (13), utilizando o fator R=0,8 e dois valores de número de Prandtl turbulento 0,35 e 0,9. Verifica-se que o valor usualmente utilizado de 0,9 em diversos modelos de turbulência térmica produz valores subestimados de flutuação de temperatura. Os valores para R=0,8 e Prt=0,35, utilizados aqui foram obtidos experimentalmente por Sirivat eWarhaft (1982). Para esse caso o desvio máximo encontrado é de 15% para Z/B=100.

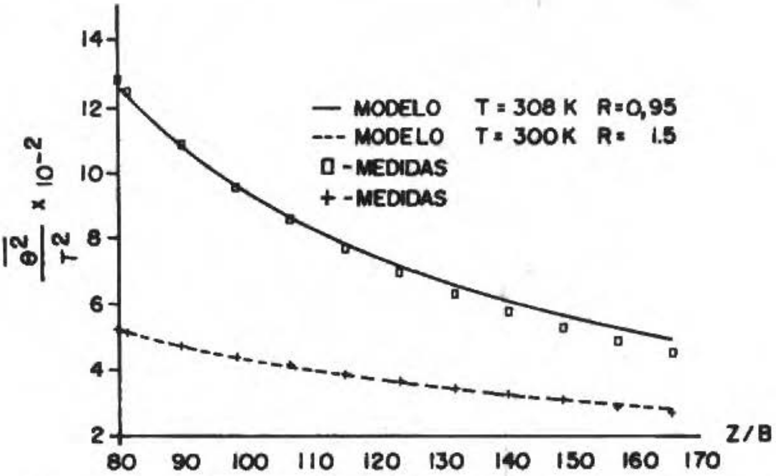

Fig. 2 Comparação entre cálculo e medidas da evolução da variância de flutuação de temperatura - grelha isotérmica

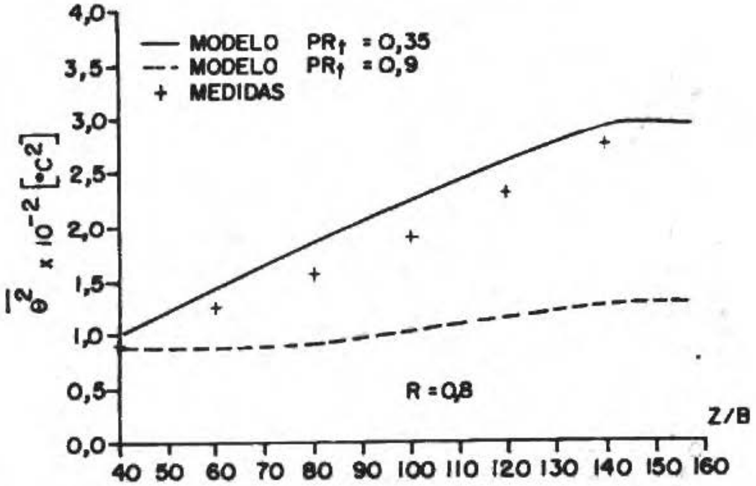

Fig. 3 Comparação entre cálculo e medidas de flutuação de temperatura - grelha com gradiente térmico

Os valores obtidos para a dissipação da flutuação de temperatura (ε_θ) foram comparados com os valores medidos, e estão presentes na Fig. 4. O desvio máximo encontrado para os valores da dissipação da flutuação de temperatura é de 16% para Z/B=80.

Nas Figs. 5 e 6 apresentam-se respectivamente as comparações entre cálculo e medida para a evolução da energia cinética de turbulência (k) e sua taxa de dissipação (ε). Os resultados mostram uma excelente previsão do modelo k-ε, entre as cotas verticais Z/B=60 e Z/B=160. O desvio máximo verificado entre valores calculados e medidos de k e ε é de 9% para os valores de k em Z/B=120 (Fig. 5).

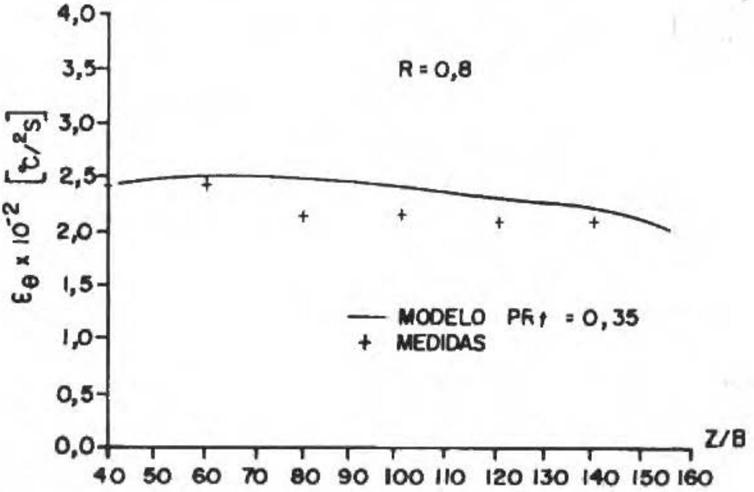

Fig. 4 Comparação entre cálculo e medidas da evolução da dissipação de flutuação de temperatura - grelha com gradiente térmico

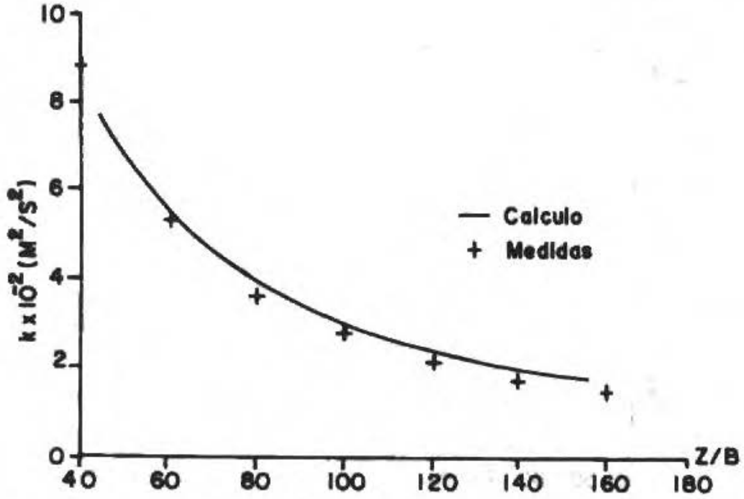

Fig. 5 Comparação entre cálculo e medidas da evolução de k - escoamento de ar atrás de grelha

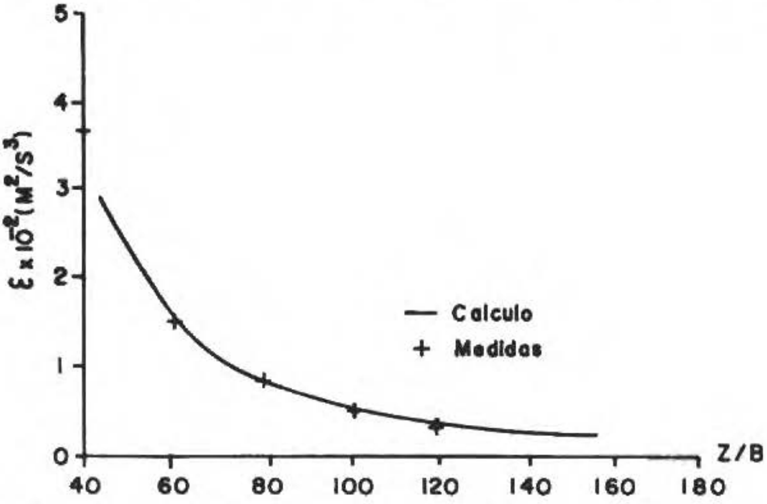

Fig. 6 Comparação entre cálculo e medidas da evolução de ε - escoamento de ar atrás de grelha

Conclusões

O modelo de turbulência a três equações aqui empregado permitiu que fossem estimados os valores de grandezas turbulentas, como as flutuações de temperatura, energia cinética de turbulência e sua taxa de dissipação em escoamentos atrás de grelha com temperatura uniforme e com gradiente de temperatura. Os resultados obtidos com esse modelo mostram um bom acordo com valores obtidos experimentalmente, apresentando um desvio máximo da ordem de 16% para as grandezas turbulentas (o desvio máximo foi obtido no cálculo da dissipação das flutuações de temperatura). Constata-se que essa concordância depende fundamentalmente dos valores utilizados para as constantes presentes no modelo, como o fator R e o número de Prandtl turbulento. Nos casos estudados de turbulência atrás de grelhas, já largamente explorados experimentalmente, dispomos de valores medidos para essas constantes e de bons valores para as condições limites necessárias para o modelo numérico. Esse fato possibilitou a validação do modelo para aplicações em turbulência de grelha isotérmica e com gradiente de temperatura.

Deve-se trabalhar ainda na construção de modelos finos para a descrição da turbulência. O conhecimento de valores medidos de grandezas turbulentas, para diversos tipos de escoamentos facilitará o ajustamento de constantes para as equações das escalas características e a validação desses modelos.

Agradecimentos:

O autor agradece a preciosa colaboração e discussões na elaboração desse trabalho ao Prof. D. Jeandel e ao Sr. D. Grand, bem como o apoio recebido do Centre d'Études Nucleaires de Grenoble. O assunto integra também o doutoramento do autor, enquanto bolsista do CNPq (Conselho Nacional de Pesquisas Tecnológicas) na Ecole Centrale de Lyon.

Referências

Cruz, G.M.M., 1989, "Modélisation des écoulements turbulents avec transferts thermiques en convection mixte", These de Doctorat, École Centrale de Lyon.

Hirt, C.W., Nichols, B.D. and Romero, N.C., 1975, "SOLA - Numerical Solution Algorithm for Transient Fluid Flow", Los Alamos Laboratory, Report LA-5852.

Rodi, W., 1978, "Turbulence models and their aplication in hydraulics. A state of the art review", SFB/80/T/127, Universidade de Karlsruhe, Germany.

Sirivat, A. and Warhaft, Z., 1982, "The effect of a passive cross-stream temperature gradient on the evolution of temperature variance and heat flux in grid turbulence". J. Fluid Mech., Vol. 128, pp. 323-346.

Warhaft, Z. and Lumley, J.L., 1978, "An experimental study of decay of temperature fluctuation in grid-generated turbulence", J. Fluid Mechanics, Vol. 88, pp. 659-684.

RBCM - J. of the Braz. Soc. Mechanical Sciences
Vol. XV - nº 1 - 1993 - pp. 88-100

ISSN 0100-7386
Printed in Brazil

Pool Boiling of Aqueous Polyacrylamide Solutions: The Influence of two Surface Active Agents

A.T.A. Wang
J.P. Hartnett
Energy Resources Center
University of Illinois at Chicago

Abstract

The influence of surfactants on the pool boiling behavior of aqueous polyacrylamide solutions has been studied. The test section consisted of an electrically heated horizontal platinum wire submerged in a saturated pool of liquid at atmospheric pressure. The polymer selected for these studies was Separan AP-30, an anionic polyacrylamide. Two surfactants were used in these studies, the anionic sodium lauryl sulfate (SLS), and the non-ionic polyoxyethylene sorbitan monooleate (Tween-80).

Various combinations of polyacrylamide and surfactant dissolved in deionized water were studied. For each solution the steady shear viscosity η, the dynamic phase shift angle (a measure of elasticity) δ, and the surface tension σ were measured. In general, the values of η and δ are dominated by the amount of polymer additive, whereas the values of σ are dominated by the surfactant concentration. The presence of surfactants generally results in a decrease in elasticity relative to the values found for the aqueous polyacrylamide solution.

The surface tension values of the aqueous solution of SLS or Tween-80 were significantly lower than the values for deionized water. Surprisingly the boiling performance of the aqueous surfactant solutions did not differ from that found for water alone. For the 250 wppm aqueous Separan solution the boiling performance is inferior to that found for deionized water alone.

The presence of the surfactant Tween-80 in the aqueous polyacrylamide solution resulted in a reduction in the surface tension but the boiling performance was not affected. In contrast, the presence of SLS in the 250 wppm aqueous polyacrylamide solution resulted in a significant increase in the heat transfer coefficient relative to the boiling performance of deionized water.

On the basis of these results, it can be concluded that lowering the surface tension of an aqueous polymer solution does not guarantee enhancement of the boiling heat transfer performance. Therefore the enhancement in boiling heat transfer reported earlier for aqueous Natrosol solutions is not due to its lower surface tension value.

Keywords: Non-Newtonian Fluids; Pool Boiling; Heat Transfer Enhancement; Experimental Methods

Introduction

Boiling heat transfer is acknowledged to be a convenient means of transferring large amounts of heat with relatively small temperature differences. Applications range from cooking to steel making, from evaporators to rocket engines, and from the power industry to computer design. Westwater (1969) has pointed out that the boiling process may involve as many as 42 variables: the physical properties of the liquid, the conditions of the heating surface, the geometry and orientation of the heating surface, the level of the superheat, etc. Given this background it is not surprising that boiling heat transfer cannot be predicted from first principles. However, within the last few decades a great number of empirical or semi-empirical correlations have been proposed for predicting boiling behavior. Among these, the most popular are the correlations of Rohsenow (1952); Forster and Zuber (1955); Forster and Greif (1959); Kutateladze (1963); and Nishikawa and Yamagata (1960). Recently, Nishikawa and Fujita (1990) have proposed a new correlation which is based on the thermodynamic similarity of thermal properties, but a number of empirical factors are still required. Recognizing that the majority of traditional heat transfer fluids are Newtonian, most of the pool boiling research has concentrated on such fluids and the available boiling correlations are restricted to Newtonian fluids.

A noted exception is the pioneering work of Kotchaphakdee and William (1970) who studied the nucleate pool boiling of aqueous polymer solutions. They reported that the heat transfer coefficients of HEC (hydroxyethyl cellulose) and PAM (polyacrylamide) solutions were as much as 250% higher than those of water on an upward facing heated flat plate; they also concluded that surface tension is

Invited Lecture - II CEM - NNE/92 - João Pessoa - PB - Brazil

a minor variable. In the intervening twenty years, a limited number of studies of the nucleate boiling behavior of aqueous polymer solutions have been reported. Some of these investigators, Gannett and William (1971), Wagle (1972), Papaioannou and Koumoutsos (1982), Wei and Maa (1982), reported findings which are consistent with those of Kotchaphakdee and William (1970). However other researchers reported results that disagree with those of Kotchaphakee and Williams. On the basis of all of these studies, it is difficult to draw any definite conclusions. A systematic study of the pool boiling performance of aqueous polymer solutions on various surfaces and surface geometries is still needed.

The recent studies of Hu (1989) of nucleate pool boiling from a horizontal wire in polyacrylamide (Separan AP-30) and hydroxyethyl cellulose (Natorsol 250HHR) aqueous solutions represent a step in that direction. For a fixed heat flux q" the value of the heat transfer coefficients h for the Separan solutions were somewhat lower than the values found for water alone. In contrast, the boiling heat transfer coefficients for the Natrosol solutions were found to be considerably higher than those found for water in the high heat flux regions, as illustrated in Fig. 1. Both of these aqueous polymer solutions are viscoelastic and their physical properties such as density, specific heat, and thermal conductivity are about the same. An exception is the surface tension values which for the Separan solutions were found to be equal to the values for water while the surface tension of the Natrosol solutions were found to be 10% lower as shown in Fig. 2. These measurements raised the question of the influence of surface tension on the pool boiling behavior of aqueous polymer solutions.

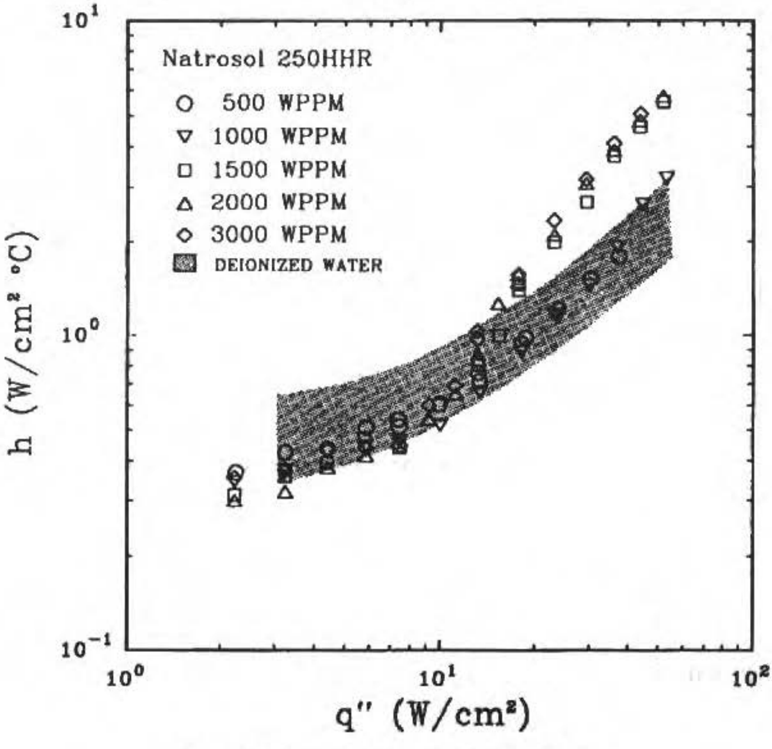

Fig. 1. Natrosol 250HHR solutions boiling data

Nomenclature

h = heat transfer coefficient (W/cm^2°C)
q" = heat flux (W/cm^2)
η = steady apparent viscosity (poise)
γ = shear rate (sec^{-1})
δ = phase shift angle (degree)
σ = surface tension (dyne/cm)
ω = oscillatory frequency (rad/sec)

For pure Newtonian liquids, it has been reported that the values of the boiling heat transfer coefficient h are proportional to σ^n, Westwater (1969), where n varies from -1.65 to -0.5. A number of studies have been carried out with the goal of increasing the heat transfer coefficient of nucleate boiling by adding a surfactant to the working fluid to depress the values of σ. In these investigations involving surfactants the value of the exponent n is reported to vary from -3.30 to 1.28, Yang and Maa (1983). In fact Lowery and Westwater (1957) reported that it is possible to improve the heat transfer performance of a Newtonian fluid by adding special wetting agents which do not reduce the surface tension.

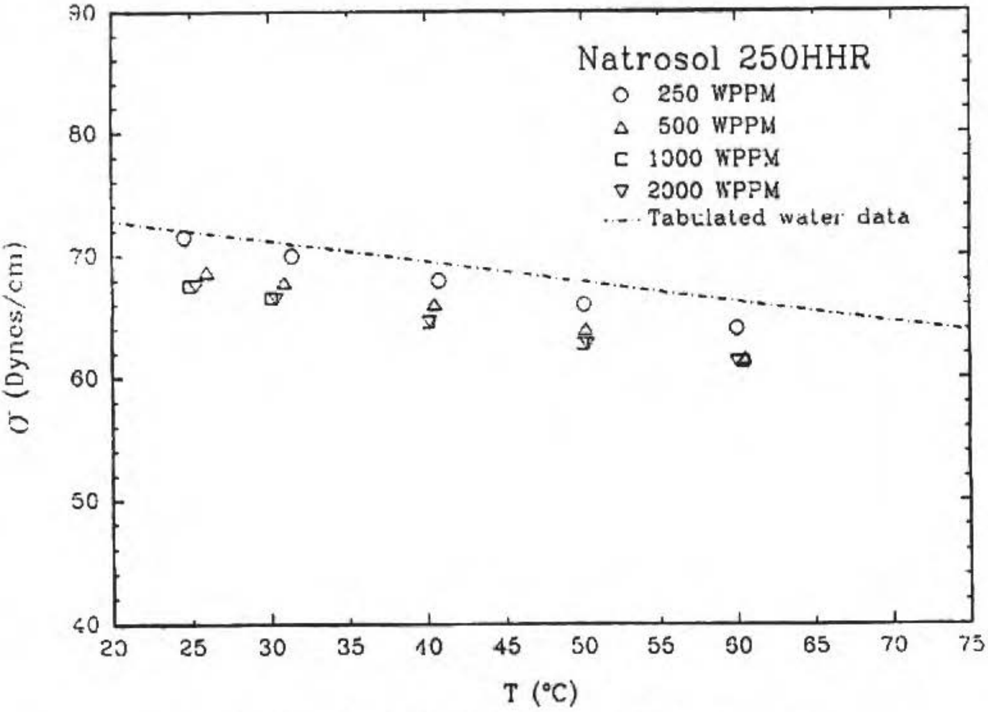

Fig. 2 Natrosol 250HHR solutions surface tension measurements

Against this background, it appears that the effects of surface tension on boiling heat transfer are not well understood for both Newtonian an non-Newtonian fluids. A study of the influence of surfactants on the pool boiling behavior of aqueous polymer solutions was initiated in the hope that it might provide some insight into the pool boiling process.

Experimental Method

Deionized water was used as the solvent for each solution studied in this investigation. An anionic modified linear polyacrylamide with a very high molecular weight, Separan AP-30 (Dow Chemical Company, Midland, MI) was used in this study. The selected surfactants for this study were sodium lauryl sulfate, SLS ($C_{12}H_{25}NaSO_4$), and polyoxyethylene sorbitan monooleate, Tween-80 ($C_{64}H_{124}O_{26}$). Both surfactants are produced by Sigma Company (St. Louis, MO). The combinations of AP-30 and SLS, and AP-30 and Tween-80 aqueous solutions listed on Table 1 were investigated. Fig. 3 illustrates the chemical structures of Natrosol 250HHR, AP-30, SLS, and Tween-80.

Table 1 Combinative concentrations of polymer and surfactant used in pool boiling experiments

AP-30 (wppm)	SLS (wppm)	Tween-80 (wppm)
0	0	0
0	250	0
0	1000	0
0	0	125
0	0	500
250	0	0
250	250	0
250	1000	0
250	0	125
250	0	500

The surface tension and the steady shear apparent viscosity of each solution were measured before and after each boiling experiment. A Sensadyne 6000 tensiometer (CSC, Scientific, Fairfax, VA) was used for the surface tension measurements, Hu et al (1991). The apparent viscosity values were measured over a wide range of shear rates, requiring a Rheometrics Fluids Spectrometer Model 8400 (RFS-4000) (Rheometery Inc., Piscataway, NJ,1986), a Brookfield Viscometer (Brookfield Engineering Laboratories Inc, Stoughton, MA, 1985) and a laboratory built capillary tube, Yoo (1974).

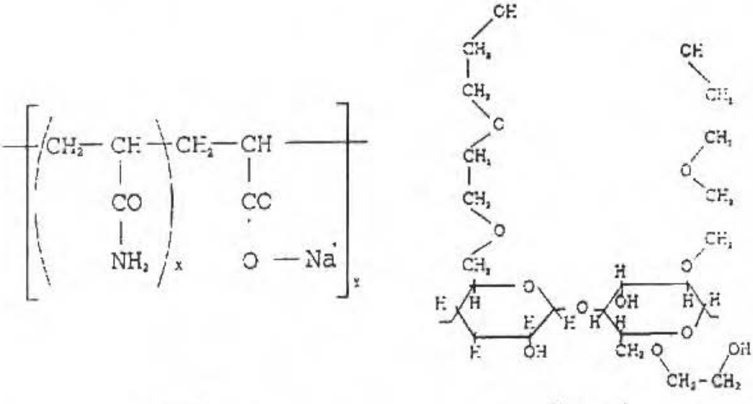

Fig. 3a. Polymer's chemical structure

Dynamic oscillatory viscometric measurements were carried out to obtain a quantitative measure of the fluid elasticity. The phase shift between the input frequency of oscillation and the output response when the testing liquid is subjected to an oscillatory motion provides this information. A 90° phase shift corresponds to a purely viscous fluid while a 0° phase shift corresponds to a purely elastic material.

The studies of the pool boiling heat transfer of each solution were carried out on an electrically heated platinum wire 0.0254 cm in diameter and 15.24 cm in lenght. The wire also served as the wire temperature measuring device. The detailed experiment setup is described in Hu (1989).

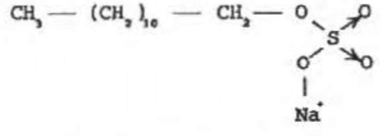

Sodium Lauryl Sulfate

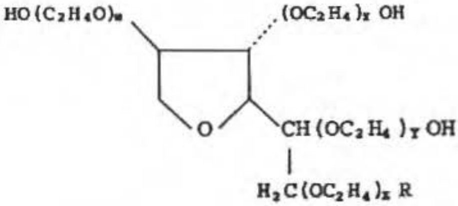

$x+y+z+w=20$; R is $(C_{17}H_{33})COO$

Tween-80

Fig. 3b. Surfactant's chemical structure

Results and Discussion - Property Measurements

It is reasonable to assume that the addition of polyacrylamide and surfactant to deionized water has little influence on properties such density, specific heat, thermal conductivity, Yoo (1974). The major properties influenced by the present additives are the apparent viscosity, the surface tension, and the dynamic phase shift. However, these three physical properties - the surface tension, the apparent viscosity, and the phase shift angle - are greatly affected by the additive concentrations.

Separan AP-30 with SLS Solutions

Aqueous solutions of AP-30 with and without SLS are first considered. Fig. 4 reveals that the presence of 250 wppm of SLS in deionized water results in a significant reduction in surface tension relative to the value for water alone. An increase in the concentration of SLS to 1000 wppm results in a further decrease in the surface tension to values below 50 dynes/cm. The addition of 250 wppm of polyacrylamide to the SLS solutions makes very little difference in the surface tension values.

The steady shear viscosity measurements shown on Fig. 5 reveal that the aqueous polymer solution has the highest steady shear viscosity values. The values of η decreases as the concentration of SLS increases, especially in the low shear rate range. In the absence of the polymer, the value of the apparent viscosity of the aqueous SLS solutions is equal to that for ionized water. Finally, it should be noted that the aqueous polymer solutions containing the surfactant show a large decrease in the low shear rate viscosity as a result of the boiling process, reflecting the fact that the Separan-SLS solutions are more susceptible to degradation.

The oscillatory phase shift measurements presented on Fig. 6 reveal that the 250 wppm polyacrylamide aqueous solution is the most elastic of the solutions studied. The presence of SLS results in an increase of the phase shift, refleting a decrease in elasticity, over the frequency range studied.

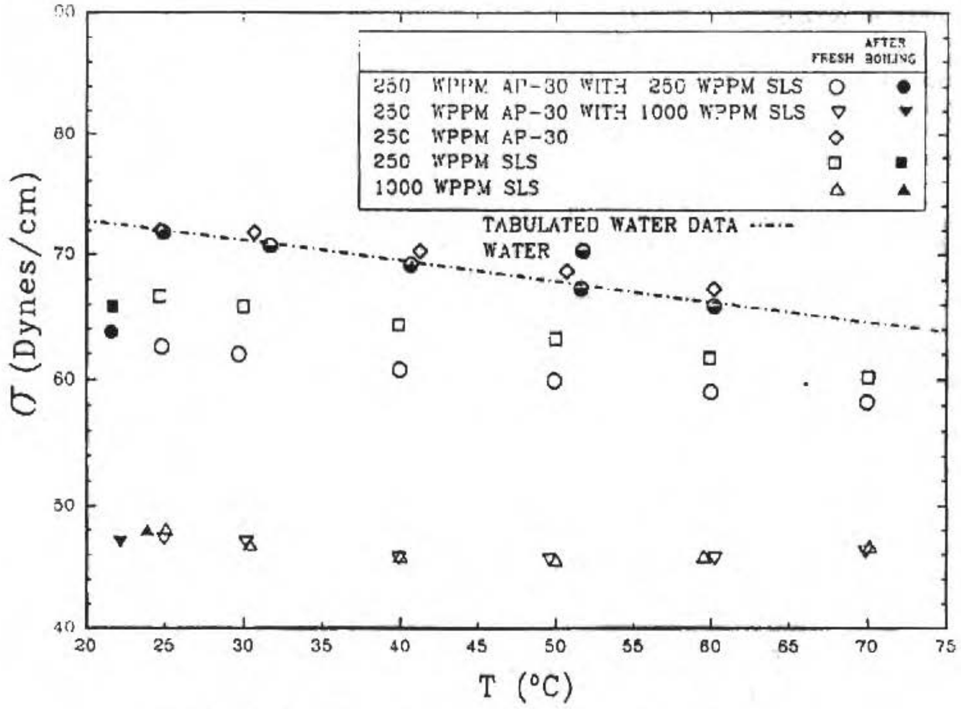

Fig. 4 AP-30 Separan with SLS solutions surface tension measurements

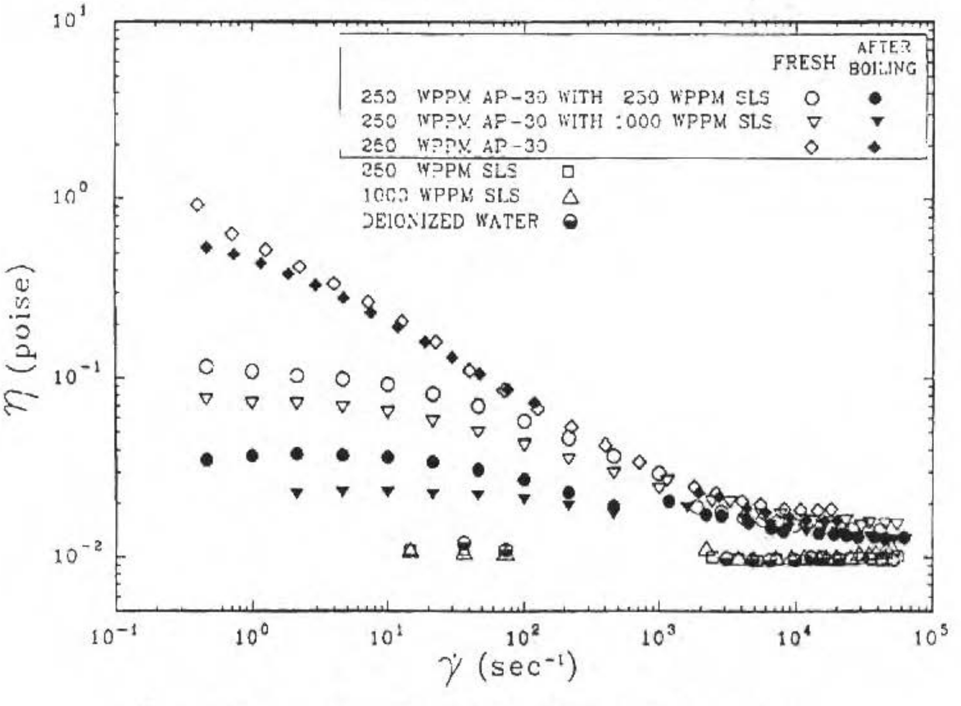

Fig. 5 AP-30 Separan with SLS solutions apparent viscosity measurements

Tween-80 with Separan Solutions

Figs. 7 and 8 depict the results of the surface tension and steady apparent viscosity measurements, respectively. The values of surface tension for Tween-80 solution decrease with an increase in concentration of Tween-80. The surface tension of these solutions are not affected by the presence of 250 wppm of AP-30. The surface tension measurements at room temperature taken after the boiling experiment are about the same as those found for the fresh solutions.

The apparent viscosity for aqueous Tween-80 solutions indicates that these solutions behave as Newtonian fluids with the viscosity equal to the values for deionized water. The addition of 250 wppm AP-30 to the Tween-80 solutions resulted in a dramatic increase in the low shear rate viscosities. In fact, the three aqueous solutions containing 250 wppm polyacrylamide all showed the same steady shear viscosity values (i.e. the viscosity was dependent on the concentration of polyacrylamide and independent of the concentration of Tween-80). Finally it should be noted that the polymer solutions containing Tween-80 showed significant degradation as a result of boiling as compared to the Separan solution alone.

The oscillatory viscometric measurements revealed that the addition of 125 wppm of Tween-80 to 250 wppm of polyacrylamide resulted in a slight increase in the phase shift, δ, reflecting a slight decrease in elasticity as compared to the aqueous polymer solution. However, an increase in the surfactant concentration to 500 wppm resulted in an aqueous solution having the same elasticity as the aqueous Separan solution. In general, the fresh solutions with Tween-80 showed a higher value of elasticity than the SLS solutions. However, the Tween-80 solutions, after boiling showed a substantial increase in δ, reflecting a loss of elasticity due to degradation of the polymer-surfactant solution.

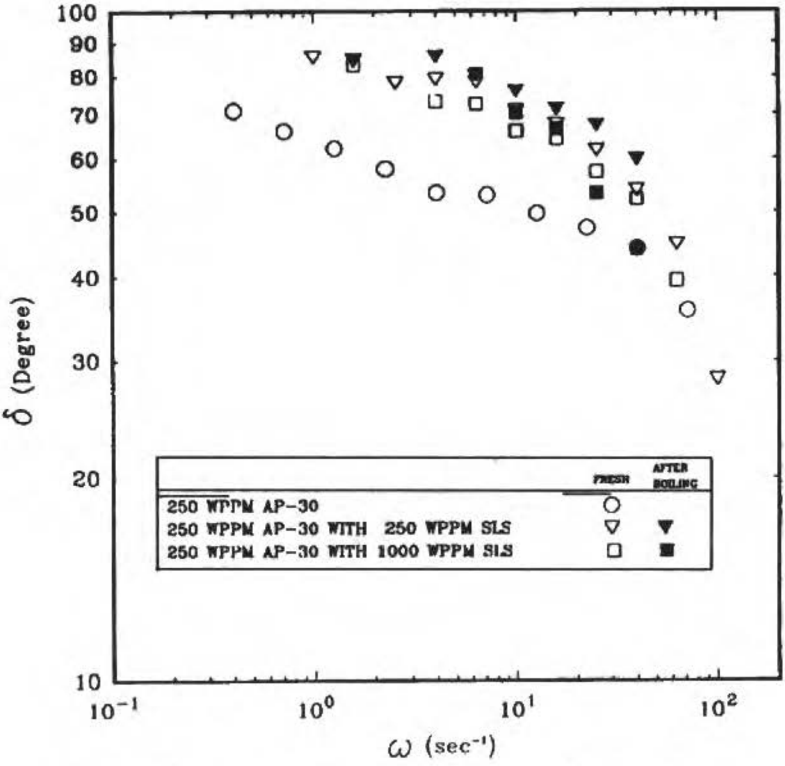

Fig. 6 AP-30 Separan with SLS solutions oscillatory phase shift measurements

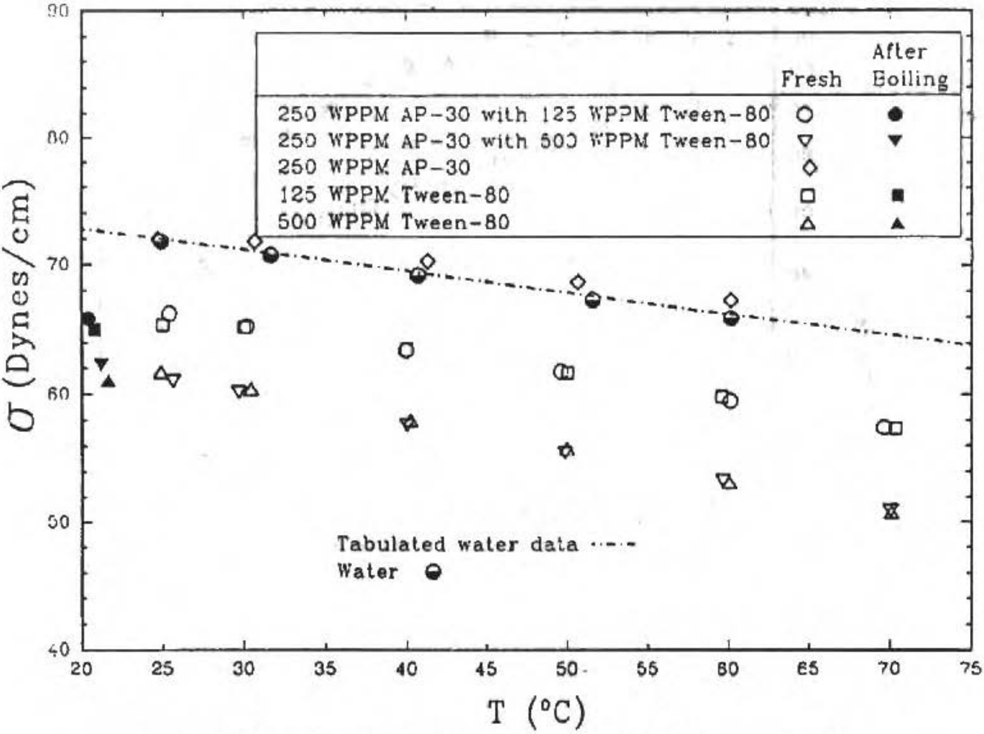

Fig. 7 AP-30 Separan with Tween-80 solutions surface tensions measurements

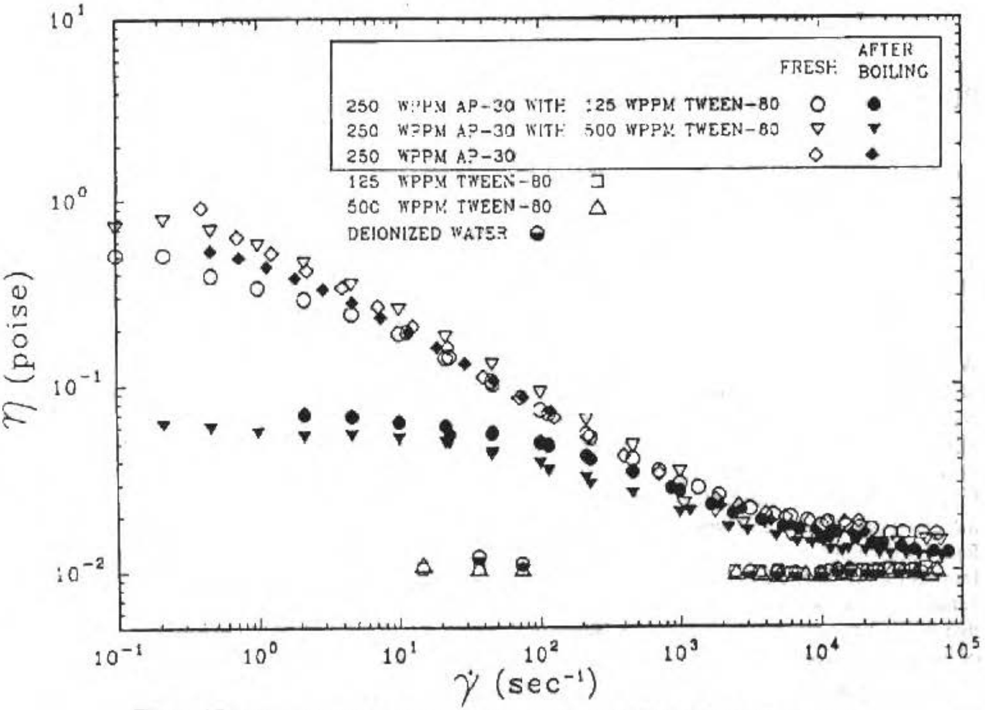

Fig. 8 AP-30 Separan with Tween-80 solutions apparent viscosity measurements

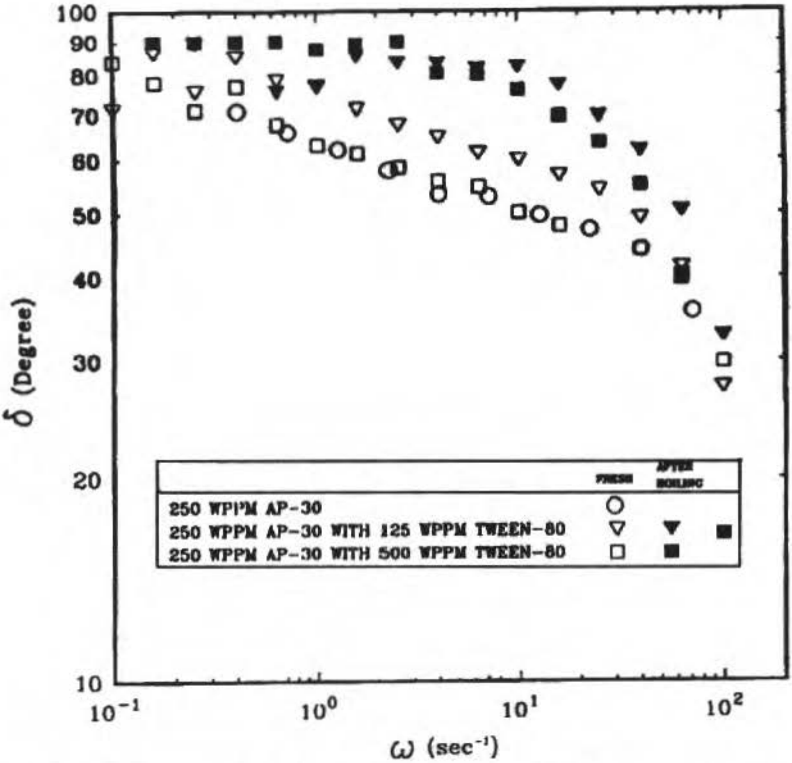

Fig. 9 AP-30 Separan with Tween-80 solutions oscillatory phase shift measurements

Pool Boiling Results and Discussion

The pool boiling data for deionized water are portrayed in Fig. 10. Generally, the measurements agree reasonably well with the predictions of Kutateladze (1963) and Nishikawa (1960), at high heat fluxes and with Rohsenow (1952) at low heat fluxes.

The pool boiling results for the 250 wppm aqueous polyacrylamide solutions with and without sodium lauryl sulfate are given on Fig. 11. The shaded area represents the range of values found for deionized water alone as given on Fig. 10. To begin with, it can be seen that the lowest value of the boiling heat transfer coefficient is associated with the 250 wppm polyacrylamide solution and that the boiling performance of the polyacrylamide solution is generally inferior to that of deionized water. With the exception of a few experimental results in the low heat flux region the addition of the surfactant SLS to deionized water does not influence the pool boiling behavior, even though the surface tension values of the aqueous surfactant solutions are substantially reduced as compared to water. Perhaps the most interesting results are those of aqueous polyacrylamide solutions with the surfactant SLS. At the lower heating rates, the boiling performance of these solutions are in general agreement with those found for deionized water. However at the higher heating rates the boiling heat transfer coefficient for the 250 wppm SLS - 250 wppm polyacrylamide solution yielded values which were higher than those found for water alone and dramatically higher than that found for the aqueous polyacrylamide solution. Increasing the SLS concentration to 1000 wppm results in further heat transfer enhancement and this behavior begins to approach the results found for Natrosol as shown on Fig. 1. At this point it may appear that the higher heat transfer results for Natrosol reported earlier are related to the lower surface tension of Natrosol as compared to water and to the polyacrylamide solution.

Fig. 12 presents the pool boiling data for the polyacrylamide-Tween 80 aqueous solutions. As in the case of SLS, the Tween-80 in deionized water showed a substantial decrease in surface tension, but the boiling performance was in the same range as found for deionized water alone. For the Tween-80 in the aqueous polyacrylamide solution, the measured boiling heat transfer coefficients were somewhat higher than the values found for the aqueous polyacrylamide solution, but were on the low side of the values found for deionized water alone. In contrast to the enhanced heat transfer results found with SLS in the aqueous polyacrylamide solution, the results with the surfactant Tween-80 gave no evidence of heat transfer enhancement. Thus these studies reveal that a reduction in the surface tension of an aqueous polymer solution does not guarantee an increase in the heat transfer performance.

On the basis of these measurements it is concluded that the observed enhancement of the pool boiling heat transfer coefficient of aqueous Natrosol solutions is not associated with its lower surface tension value.

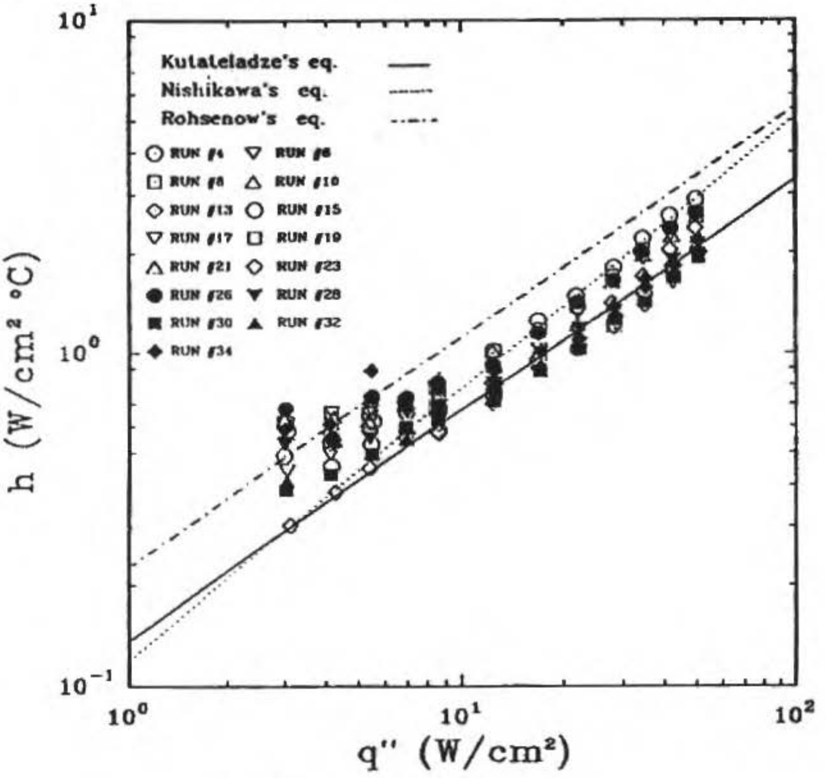

Fig. 10 Deionized water boiling data

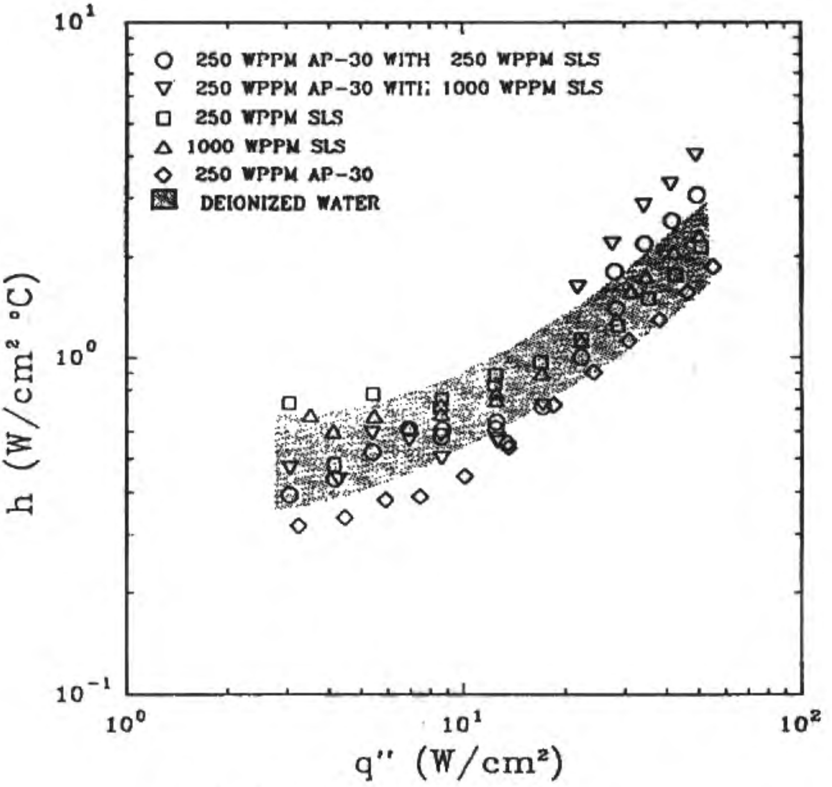

Fig. 11 AP-30 Separan with SLS solutions boiling data

Conclusions

The addition of two different surface acting agents (Tween-80 and SLS) to water and to aqueous polyacrylamide (AP-30) solutions resulted in significant reductions in the values of the surface tension. In the case of the surfactant-deionized water solutions the boiling behavior was indistinguishable from the pool boiling behavior of water alone. In the case where the surfactants were added to the aqueous polyacrylamide solution, the addition of SLS resulted in a significant increase of the boiling heat transfer coefficient at high heat fluxes as compared to the measured values for water and for the aqueous polyacrylamide solution. In contrast the addition of the Tween-80 surfactant to the aqueous polymer solution resulted in a boiling performance which was no better than the boiling performance of water alone.

It can be concluded that the reduction of surface tension induced by the addition of a surface active agent to a boiling fluid does not always lead to improved heat transfer performance. Therefore the enhancement in the boiling heat transfer reported earlier for aqueous Natrosol solutions is not due to its lower surface tension value.

Acknowledgements

The authors acknowledge the financial support of the Division of Engineering of the Office of Basic Energy Sciences of the U.S. Department of Energy under its Grant No. 85Er13311.

References

Chou, C.C. and Yang, Y.M., 1991, "Surfactant effects on the temperature profile within the superheated boundary layer and the mechanism of nucleate pool boiling", J. CIhE., 22(2) : 71-80.

Dunskus, T., and Westwater, J.W., 1961, " The effect of trace additives on the heat transfer to boiling isopropanol", Chem. Engng. Prog. Symp. Series, 57(32) : 173-181.

Forst, W. and Kippenhan, C.J., 1967, "Bubble growth and heat transfer mechanisms in the forced convection boiling of water containing a surface active agent", Int. J. Heat Mass Transfer, 10 : 931-949.

Forster, H.K., and Zuber, N., 1955, "Dynamics of vapor bubbles and boiling heat transfer", AIChE J., 1 : 531-535.

Forster, H.K., and Greif, R., 1959, "Heat transfer to boiling liquid-mechanism and correlation", J. Heat Transfer, 81C(1) : 43-53.

Gannett, H.J., and William, M.C., 1971 "Pool boiling in dilute non-aqueous polymer solutions", Int. J. Heat Mass Transfer, 14: 1001-1005.

Hu, R.Y.Z., 1989, "Nucleate pool boiling from a horizontal wire in viscoelastic fluids", Ph.D. thesis, Univ. of Illinois at Chicago, Chicago.

Hu, R.Y.Z., Wang, A.T.A. and Hartnett, J.P., 1991, "Surface tension measurements of aqueous polymer solutions", Experimental Thermal and Fluid Science, 4(6) : 723-729.

Jontz, P.D., and Myers, J.E., 1960, "The effect of dynamic surface tension on nucleate boiling coefficient", AIChE J., 6: 34-38.

Kotchaphakdee, P., and William, M.C., 1970, "Enhancement of nucleate pool boiling with polymer additives.", Int. J. Heat Mass Transfer, 13(6) : 835-848.

Kutateladze, S.S., 1963, "Fundamental of Heat Transfer", Pergamon Press, Inc., New York.

Lowery, A.J.Jr., and Westwater, J.W., 1957, "Heat transfer to boiling methanol - Effect of added agents", Ind. and Engng. Chem., 49(9) : 1445-1447.

Miaw, C.B., 1978, "A study of heat transfer to dilute polymer solutions in nucleate pool boiling", Ph. D. thesis, Univ. of Michigan, Ann Arbor.

Morgan, A.I., Bromley, L.A. and Wilke, C.R., 1949, "Effect of surface tension on heat transfer in boiling", Ind. and Engng. Chem., 41: 2767-2769.

Nishikawa, K., and Yamagate, K., 1960, "On the correlation of nucleate boiling heat transfer", Int. J. Heat Mass Transfer, 1: 219-235.

Nishikawa, K., and Fujita, Y., 1990, "Nucleate boiling heat transfer", Advances in Heat Transfer, 20: 1-82, Hartnett, J.P., and Irvine, T.J.Jr., eds, Academic Press, New York.

Papaioannou, A.T., and Koumoutsos, N.G., 1982, "The effects of polymer additives on nucleate boiling", Proc. 7th Int. Heat Transfer Conference, 4: 67-72, Munich, West Germany.

Paul, D.D., and Abdel-Khalik, S.I., 1983, "Nucleate boiling in drag-reducing polymer solutions", J. Rheol., 27(1) : 59-76.

Rheometrics Fluids Spectrometer Model 8400 Operator Manual, Rheometers Inc., Piscataway, NJ., 1986.

Rohsenow, M.W., 1952, " A method of correlating heat transfer data for surface boiling of liquids.", Trans. ASME, 74(8) : 969-975.

Roll, J.B. and Myers, J.E., "The effect of surface tension on factors in boiling heat transfer", AIChE J., 10(4) : 530-534, 1964.

SensaDyne 6000 Surface Tensiometer Operator Manual, CSC Scientific Company, Inc., Fairfax, Va., 1988.

Shah, B.H., and Darby, R., 1973, "The effect of surfactant on evaporative heat transfer in vertical film flow", Int. J. Heat Transfer, 16: 1889-1903.

Shibayama, S., 1979, "A study on boiling heat transfer in a thin liquid film: Part 1: In the case of pure water and an aqueous solution of surface active agent", Heat Transfer (Jap. Res.), 8(2) : 12-40.

Stroebe, G.W., Baker, E.M. and Badger, W.L., 1939, "Boiling-film heat transfer coefficients in a long-tube vertical evaporator", Ind. and Engng. Chem., 31: 200-206.

The Brookfield Digital Viscometer Model DV-II Operating Instructions, Manual No. M/85-160-c, Brookfield Engineering Laboratories, Inc., Stoughton, MA, 1985.

Tzan, Y.L. and Yang, Y.M., 1990, "Experimental study of surfactant effects on pool boiling heat transfer", J. Heat Transfer, 112: 207-212.

Ulicny, J.C., 1984, "Nucleate pool boiling in dilute polymer solutions", Ph.D. thesis, Univ. of Michigan, Ann Arbor.

Wagle, A.K., 1972, "Boiling heat transfer in viscoelastic fluids", Ph.D. thesis, Univ. of Delaware, Newark.

Wei, H. and Maa, J.R., 1982, "Enhancement of flow boiling heat transfer with polymer additives", Int. J. Heat Mass Transfer, 25(3) : 431-434.

Westwater, J.W., 1969, "Nucleate pool boiling. Advanced Heat Transfer.", Chao, B.T., ed., 217-232, Univ. of Illinois Press.

Yang, Y.M. and Maa, J.R., 1982, "Effects of polymers additives on pool boiling phenomena", Lett. Heat Mass Transfer, 9: 237-244.

Yang, Y.M. and Maa, J.R., 1983, "Pool boiling of dilute surfactant solutions", J. Heat Transfer, 105: 190-192.

Yoo, S.S., 1974, "Heat transfer and friction factors for Non-Newtonian fluids in turbulent pipe flow", Ph.D. thesis, Univ. of Illinois at Chicago.

RBCM - J. of the Braz. Soc. Mechanical Sciences
Vol. XV - nº 1 - 1993 - pp. 101-108

ISSN 0100-7386
Printed in Brazil

Numerical Simulation of Two-phase Flow Separation in a T-junction

Luiz Felipe M. Moura and Fernando Antonio S. Carneiro
UNICAMP - FEM - DETF
C.P. 6122
13081 Campinas, SP
Brazil

Abstract

The principal objective of this paper is to investigate numerically the gas-liquid phase separation in a vertical T-junction. A two-dimensional computer code was used to solve the two-fluid model equations, using the finite volume method. Special attention is directed to the modeling of the viscous diffusion term and the constitutive equation for the interfacial friction term.

The phase separation was simulated considering two different values of the branch to inlet diameter ratio, 0.5 and 1.0, according to the reported experimental results. The flow conditions in the T-junction inlet were related to the churn-turbulent flow pattern.

Detailed distributions of the void fraction, pressure and velocity of both phases are presented. A good agreement was obtained between the computer code results and the experimental data. For the mass split ratios greater then 0.3, the mean deviation was about 10%. However, for lower split ratios, a three-dimensional model would be more suitable. This work includes also the investigation of the boundary conditions, gravity, viscosity and mesh size on the phase separation phenomena.

Keywords: Finite Volume Method, Numerical Simulation, Two-phase Flow, T-junction.

Introduction

The two-phase gas-liquid flows in T-junction has several applications in petroleum production plants such as offshore production manifolds (Oliveira, 1989), steam injection process and offshore phase separators. There are other applications in power and chemical plants.

The petroleum engineers are often interested on the multiphase flow pressure drop and the flow configuration in branching geometries. It is well know that the operation, maintenance and the efficiency of many petroleum processes depend on the flow distribution in the branching pipes.

Many investigations has been undertaken on T-junction two-phase flow during the past 10 years (Hwang, Soliman and Lahey Jr., 1988). It can be observed from these works that the two phases are distributed unequally among the T-junction outlet sections. However, the manner in witch the phases are distributed is not yet well understood.

The objective of the present work is to investigated the ability of the two-dimensional two-phase flow computer code developed by Moura (1989) to predict the phase separation in vertical T-junctions.

Theoretical Model

The theoretical modeling of the two-phase flow separation in T-junctions is very complex, because of the dynamic interaction between the two phases. The more suitable model for this flow configuration is the two-fluid model. This model is expressed in terms of two sets of conservation equations governing the mass, momentum and energy in each phase. However, since the averaged fields of one phase are not independent of the other phase, the interaction terms witch couple the transport of mass, momentum and energy across the interface appears in the conservation equations as source terms.

The two-phase flow in T-junction region is supposed to be isothermal with no mass transfer. This simplification is acceptable because the small branching region, thus the heat and mass transfer in this region don't have a significant influence on the mass and momentum balances. In addition, the turbulent diffusion processes are neglected. Then the two-dimensional formulation of the two-fluid model conservation equations (Ishii, 1975) becomes:

Manuscript received January 1993. Associate Technical Editor: Carlos A. C. Altemani

Liquid mass balance:

$$\frac{\partial}{\partial t}(\alpha_l \rho_l) + \frac{\partial}{\partial x}(\alpha_l \rho_l u_l) + \frac{\partial}{\partial y}(\alpha_l \rho_l v_l) = 0 \tag{1}$$

Gas mass balance:

$$\frac{\partial}{\partial t}(\alpha_g \rho_g) + \frac{\partial}{\partial x}(\alpha_g \rho_g u_g) + \frac{\partial}{\partial y}(\alpha_g \rho_g v_g) = 0 \tag{2}$$

Liquid momentum balance in the x direction:

$$\begin{aligned}&\frac{\partial}{\partial t}(\alpha_l \rho_l u_l) + \frac{\partial}{\partial x}(\alpha_l \rho_l u_l^2) + \frac{\partial}{\partial y}(\alpha_l \rho_l u_l v_l) = \\ &= -\alpha_l \frac{\partial P}{\partial x} + \alpha_l \rho_l g_x + K_{lg}(u_l - u_g) + \mu_l \left[\frac{\partial}{\partial x}\left(\alpha_l \frac{\partial}{\partial x} u_l\right) + \frac{\partial}{\partial y}\left(\alpha_l \frac{\partial}{\partial y} u_l\right)\right]\end{aligned} \tag{3}$$

Gas momentum balance in the x direction:

$$\begin{aligned}&\frac{\partial}{\partial t}(\alpha_g \rho_g u_g) + \frac{\partial}{\partial x}(\alpha_g \rho_g u_g^2) + \frac{\partial}{\partial y}(\alpha_g \rho_g u_g v_g) = \\ &= -\alpha_g \frac{\partial P}{\partial x} + \alpha_g \rho_g g_x + K_{lg}(u_l - u_g) + \mu_g \left[\frac{\partial}{\partial x}\left(\alpha_g \frac{\partial}{\partial x} u_g\right) + \frac{\partial}{\partial y}\left(\alpha_g \frac{\partial}{\partial y} u_g\right)\right.\end{aligned} \tag{4}$$

Liquid momentum balance in the y direction:

$$\begin{aligned}&\frac{\partial}{\partial t}(\alpha_l \rho_l v_l) + \frac{\partial}{\partial x}(\alpha_l \rho_l u_l v_l) + \frac{\partial}{\partial y}(\alpha_l \rho_l v_l^2) = \\ &= -\alpha_l \frac{\partial P}{\partial y} + \alpha_l \rho_l g_y + K_{lg}(v_g - v_l) + \mu_l \left[\frac{\partial}{\partial x}\left(\alpha_l \frac{\partial}{\partial x} v_l\right) + \frac{\partial}{\partial y}\left(\alpha_l \frac{\partial}{\partial y} v_l\right)\right]\end{aligned} \tag{5}$$

Gas momentum balance in the y direction:

$$\begin{aligned}&\frac{\partial}{\partial t}(\alpha_g \rho_g v_g) + \frac{\partial}{\partial x}(\alpha_g \rho_g u_g v_g) + \frac{\partial}{\partial y}(\alpha_g \rho_g u_g^2) = \\ &= -\alpha_g \frac{\partial P}{\partial y} + \alpha_g \rho_g g_y + K_{lg}(v_l - v_g) + \mu_g \left[\frac{\partial}{\partial x}\left(\alpha_g \frac{\partial}{\partial x} v_g\right) + \frac{\partial}{\partial y}\left(\alpha_g \frac{\partial}{\partial y} g_g\right)\right]\end{aligned} \tag{4}$$

where:

l = liquid
g = gas
P = pressure
u = velocity in the x direction
v = velocity in the y direction
α = volumetric fraction
ρ = density
μ = viscosity
g = gravity
K_{lg} = interfacial friction coefficient

The terms $K_{lg}(u_g - u_l)$ and $K_{lg}(v_g - v_l)$ represent the interfacial momentum transfer in the x and y directions, respectively.

The equations (1) to (6) constitute a system of six equations that represent the mass and momentum conservation for each phase. However, there are nine dependent variables. Then, to complete the equation set, the following relations are used:

$$\rho_l = \rho_l(P) \tag{7}$$

$$\rho_g = \rho_g(P) \tag{8}$$

$$\alpha_l + \alpha_g = 1 \tag{9}$$

To solve this set of equations we need to specify a constitutive relation for the interfacial friction coefficient.

For dispersed two-phase flow the interfacial friction coefficient can be modeled (Ishii and Zuber, 1979) by the following equation:

$$K_{lg} = \frac{1}{8} a_i C_D \rho_c |V_r| \tag{10}$$

where:

a_i = interfacial area
C_D = drag coefficient
ρ_c = continuous phase density
V_r = relative velocity

The drag coefficient has been modeled (Ishii and Mishima, 1984) for different flow patterns such as bubbly, slug and churn flow. The interfacial area has been studied (Kataota, Ishii and Serizawa, 1984; DeJesus and Kawaji, 1989) but until now no general model is available.

The two-phase flow in a T-junction exhibit a complex interfacial structure with the phase distribution quite different from the two-phase flow in a straight tube. Moreover, two or more different flow patterns may exist in the branching region. In order to overcome these limitations the interfacial friction expression (10) was extended to a general form by using the mixture density:

$$K_{lg} = a_i C_D \rho_m |V_r| \tag{11}$$

where the mixture density is given by:

$$\rho_m = \alpha_g \rho_g + \alpha_l \rho_l \tag{12}$$

The interfacial area and the drag coefficient are supposed to a function of the volumetric fractions. The interfacial area must vanish when the volumetric fraction of one phase goes to zero. Then, the interfacial friction coefficient may be given by:

$$K_{lg} = C \alpha_l \alpha_g \rho_m |V_r| \tag{13}$$

In this expression the constant C has the dimension of the interfacial area (#) and takes into account the mean value of the drag coefficient (about one). Equation (13) was used to predict some experimental phase separation data (Davis and Fungtamasan, 1990). Different values for the constant C were used ranging from 200 to 800 m^{-1} and the more appropriate value to predict the experimental data was:

$C = 400\ m^{-1}$

Numerical Model

The model equations (1) to (9) are discretized following the finite volume method with staggered grid proposed by Patankar (1980). The numerical algorithm used to solve the discretized equations is described elsewhere (Moura, 1991) and only the principal steps are presented below.

The momentum equations are rewritten in a non-conservative form. The liquid mass conservation equation (1) is multiplied by the liquid velocity in the x and y directions and the resulting equations are subtracted from the liquid momentum equations in the x and y directions, respectively. The non-conservative gas momentum equations are obtained following the same procedure.

The liquid and the gas mass conservation equations are integrated over the volume centered on the scalar variables. The value of the scalar variables on the volume faces are calculated by using the full donorcell scheme.

The liquid and the gas non-conservative momentum equations in both directions are integrated over the volumes centered on the velocities. The convective and the viscous diffusion terms calculation are explicit, that is, from the variables values obtained at the previous time step.

The momentum discretized equations are rewritten in order to explicit the phase velocity. In each of these equations appears the velocity of the other phase. Then the liquid (gas) velocity is eliminated in the gas (liquid) momentum equation.

Finally, the liquid mass conservation equation is combined with the liquid momentum equation, resulting in an equation to the pressure and the liquid volumetric fraction. The same procedure is applied to the gas mass and momentum equations. The resulting equations may be solved by the Newton iterative method. The difference pressure equation for each phase are combined in order to eliminate the volumetric fractions.

The final system of pressure equation represent a set of linear equations where the pressure of each node is related to the pressure of the neighbouring nodes. This system of equations may be solved by the Tri-Diagonal Matrix Algorithm iterative method.

Results

Some of the available experimental data (Honan and Lahey, 1981; Davis and Fungtamasan, 1990) about the two-phase flow separation in a vertical T-junction was used to verify the numerical simulation performance.

A diagram of the vertical T-junction with the notation for inlet and outlet sections is presented below.

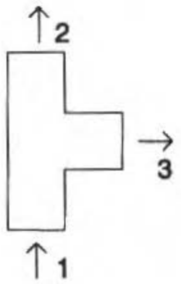

Davis and Fungtamasan (1990) studied the flow separation for low values of the mass ratio $(0,1 < W3/W1 < 0,5)$. The tube diameter was 0.050 m and the branch to the main outlet diameter ratio (D3/D1) was equal to one.

Honan and Lahey (1981) studied the flow separation for higher mass split ratios $(0,3 < W3/W1 < 0,7)$. They worked with a 0.038m diameter T-junctions with D3/D1=1 and D3/D1=0,5 .

There are 69 experimental data points for D3/D1=1 and 32 data points for D3/D1=0,5 . Each data point is characterized by the inlet mass flow rate and quality, the mass split ratio and phase separation or the branch to the main outlet quality ratio $(x3/x1)$.

The two numerical grids used for the flow simulation in a T-junction with D3/D1=1 presented in Figure 1.

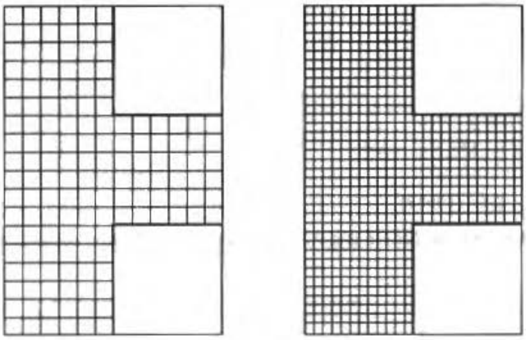

a) 12x18 b) 24x36

Fig. 1 Numerical grids for D3/D1=1

The inlet boundary conditions for the numerical simulation were the gas and the liquid velocities and the gas volumetric fraction (void fraction). These values are calculated from the homogeneous model.

The outlet boundary conditions were the branch and the main outlet pressures. The pressure difference between both outlets was adjusted to provide the measured mass split ratio.

The initial conditions for all flow domain were chosen as a constant pressure (100kPa) and the same void fraction and velocity as the inlet boundary conditions.

The numerical simulations were carried out until the steady state flow conditions were reached.

Figure 2 shows the experimental (Davis and Fungtamasan, 1990) and the numerical values of the phase separation ratio for D3/D1=1, using the coarse and the finer grids. The flow conditions are summarized in Table 1. for the coarse grid (12x18) the mean deviation between predicted and measured phase separation is about 25%, with a tendency to over predict the experimental data. However, for the finner grid (24x36) the mean deviation to 17%.

A better agreement is obtained for the experimental data of Honan and Lahey (1981). The phase separation ratio was predicted using the coarse grid with a mean deviation of less then 9%. Figure 3 shows the comparison between numerical and experimental results.

Finally, the Figure 4 shows the predicted and the experimental (Davis and Fungtamasan, 1990) values of the phase separation ratio for D3/D1=0,5 , using a coarse grid (12x15) and a finer grid (14x30). The mean deviation for the coarse and the finer grids are 23 and 20%, respectively.

A typical numerical result of the two-phase flow distribution in a vertical T-junction is show in Figure 5 for D3/D1=1 . The mass flux, the air-water quality and the mass split ratio were 1356 kg/m^2s, 0.1% and 0.32, respectively. It can be observed in the Figure 5 that the gas turns to the branch more easy then the liquid (Figure 5.a and 5.b), certainly because the negative pressure gradient (Figure 5.d) in the branch. The gas acceleration near the junction produces a high void fraction region (Figure 5.c) in the lower half of the branch.

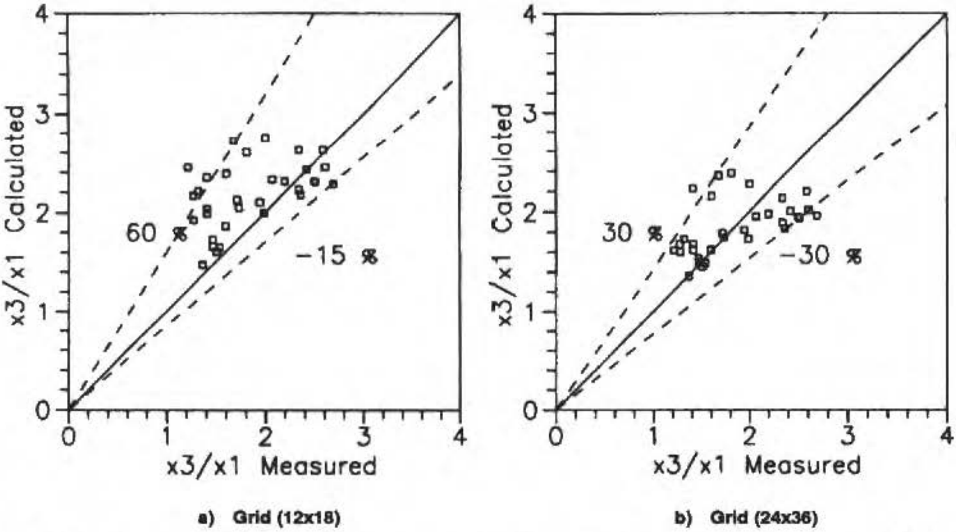

a) Grid (12x18) b) Grid (24x36)

Fig. 2 Numerical and experimental (Davis and Fungtamasan, 1990) phase separation in a T-junction. D3/D1=1

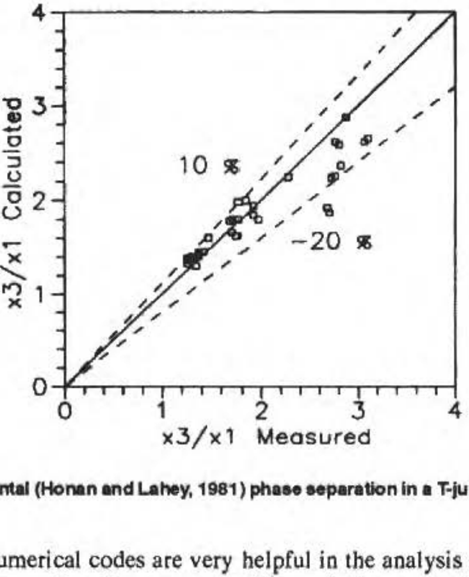

Fig. 3 Numerical and experimental (Honan and Lahey, 1981) phase separation in a T-junction. D3/D1=1, grid (12x18)

The two-phase flow numerical codes are very helpful in the analysis of the influence of some parameters on the phase separation phenomena. In this work the parameters investigated were the viscous and gravitational forces, and the inlet boundary conditions.

The influence of the gravitational field on the phase separation is only significant for low values of the mass split ratio. The fluid viscosities also have a very small influence, and only with a 500 higher viscosity the phase separation results showed a significant change.

The inlet boundary condition has an important influence on the phase separation. The specification of the fully developed velocities and void fraction profiles instead of the constant homogeneous boundary conditions improves the numerical predictions.

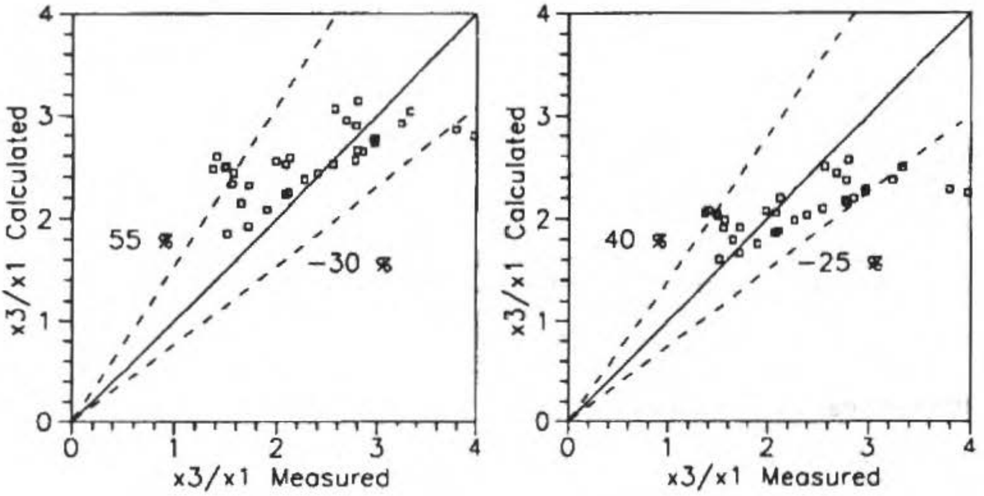

a) Grid (12x15)

b) Grid (24x30)

Fig. 4 Numerical and experimental (Davis and Fungtamasan, 1990) phase separation in a T-junction. D3/D1=0,5

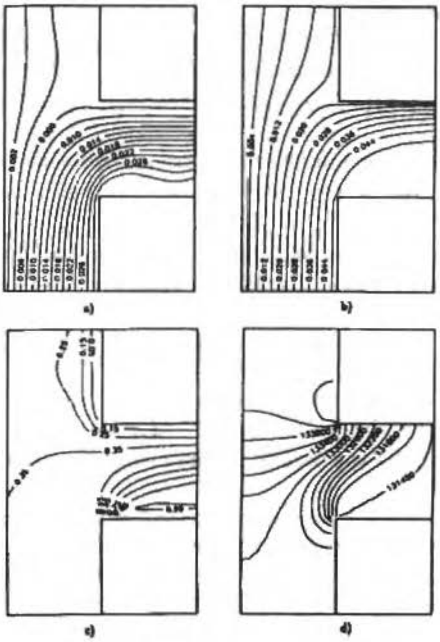

Fig. 5 Two-phase flow distribution in a T-junction: a) Gas stream function; b) Liquid stream function; c) Void fraction; d) Pressure.

Conclusions

A two-dimensional two-phase flow computer code was used to investigate the phase separation of dispersed gas-liquid flows in a vertical T-junction.

A general constitutive equation for the interfacial friction coefficient was developed in this work. The obtained numerical results for the phase separation ratio are in good agreement with the experimental data. The mean deviation was about 10% for mass split ratios greater then 0.3. However, for low values of the mass split ratio the experimental data are under predicted, and the mean deviation was about 25%.

The influence of the viscous and the gravitational forces on the phase separation was insignificant, showing that the dominant forces are the inertial and the interfacial forces. In the other hand, the inlet boundary conditions have a significant influence on the phase separation and the numerical result can be improved with the specification of the fully developed profiles.

References

Azzopardi, B.J. and Whalley, P.B., 1982, "The Effect of Flow Patterns on Two-Phase Flow in a T-Junction". Int. J. Multiphase Flow, 8, 491-507.

Carneiro, F.A.S., 1991, "Simulação Numérica de Separação de um Escoamento Bifásico Gás-Líquido em um Tê", M. Sc. Thesis, Universidade Estadual de Campinas, Brazil.

Davis, M.R. and Fungtamasan, B.,1990, "Two-Phase Flow Trough Pipe Branch Junctions", Int. J. Multiphase Flow, 16, 799-817.

DeJesus, J.M. and Kawaji, M., 1989, "Measurement of Interfacial Area and Void Fraction in Upward, Concurrent Gas-Liquid Flow", ANS National Heat Transfer Conference, USA.

Henry, J.A.R., 1981, "Dividing Annular Flow in a Horizontal Tee", Int. J. Multiphase Flow, 7, 343-355.

Honan, T.J. and Lahey Jr., R.T., 1981, "The measurement of Phase Separation in Wyes and Tees", Nuclear Engrg. Design, 64, 93-102.

Hong, K.C., 1978, "Two-Phase Flow Splitting at a Pipe Tee", Journal of Petroleum Technology, February, 290-296.

Hwang, S.T.; Soliman, H.M. and Lahey Jr., R.T., 1988, "Phase Separation in Dividing Two-Phase Flows", Int. J. Multiphase Flow, 14, 439-458.

Ishii, M., 1975, "Thermo-Fluid Dynamic Theory of Two-Phase Flow", Eyrolles, France.

Ishii, M. and Zuber, N., 1979, "Drag Coefficient and Relative Velocity in Bubbly, Droplet or Particulate Flows", AIChE. Journal, 25, 842-855.

Ishii, M. and Mishima, K., 1984, "Two-Fluid Model and Hydrodynamic Constitutive Relations", Nuclear Engrg. Design, 82, 107-126.

Kataota, I.; Ishii, M. and Serizawa, A., 1986, "Local Formulation and Measurement of Interfacial Area Concentration in Two-Phase Flow", Int. J. Multiphase Flow, 12, 505-529.

Lahey Jr., R.T., 1990, "The Analysis of Phase Distribution Phenomena Using Two Fluid Models", Nuclear Engrg. Design, 122, 17-40.

Moura, L.F.M., 1989, "Etude de la Redistribution d'un Ecoulement Diphasique Entre Deux Passes d'un Echangeur de Chaleur", Ph. D. Thesis, Institut National Polytechnique de Grenoble, France.

Moura. L.F.M., 1991, "Desenvolvimento de um Modelo Numérico para a Simulação de Escoamentos Bifásicos Baseado no Modelo de Dois Fluidos", XI Brazilian Congress of Mechanical Engineering, São Paulo, Brazil.

Oliveira, L.C.G., 1989, "Simulador para Rede Coletora de Produção", M. Sc. Thesis, Universidade Estadual de Campinas, Brazil.

Orange, L., 1973, "Condensate Behavior in Gas Pipelines is Predictable", Oil and Gas Journal, July, 39-44.

Patankar, S.V., 1980, "Numerical Heat Transfer and Fluid Flow", McGraw-Hill, New York.

Rubel, M.T.; Soliman, H.M. and Sims, G.E., 1988, "Phase Distribution During Steam-Water Flow in a Horizontal T-Junction", Int. J. Multiphase Flow, 14, 425-438.

Shoham, O.; Brill, J.P. and Taitel, Y., 1987, "Two-Phase Flow Splitting in a Tee Junction", Experimental and Modeling. Chemical Eng. Science, 42, 2667-2676.

RBCM - J. of the Braz. Soc. Mechanical Sciences
Vol. XV - nº 1 - 1993

ISSN 0100-7386
Printed in Brazil

Abstracts

Savi, A. M. and Braga, A. M. B., 1993, "Chaotic Vibrations of an Oscillator with Shape Memory", RBCM - J. of the Braz. Soc. Mechanical Sciences, Vol 15, n. 1, pp. 1-20.

This article reports results from some investigation on the dynamical behavior of mechanical systems containing elements with shape memory. some phenomenological theories that describe shape memory and pseudoelastic effects in metallic alloys that undergo thermoelastic martensitic transformations are reviewed. One of these theories is used to model a helical spring. The dynamic response of an oscillator with a shape memory spring is investigated. It is shown that the system may behave chaotically under certain conditions.
Keywords: Chaotic Vibrations - Nonlinear Dynamics - Shape Memory

Misici, L and Zirilli, F., 1993, "An Inverse Problem for the Three Dimensional Vector Helmholtz Equation for a Perfectly Conducting Obstacle with Incomplete Data", RBCM - J. of the Braz. Soc. Mechanical Sciences, Vol 15, n. 1, pp. 21-30.

Let $D \subset R^3$ be a simply connected bounded domain with smooth boundary ∂D. We assume that ∂D is a perfectly conducting surface. In this paper we present a numerical method to reconstruct ∂D from the knowledge of the far field patterns generated by D when hit by time harmonic linearly polarized electromagnetic waves coming from several incoming directions.
Keywords: Inverse problem - Electromagnetic Theory - Obstacle Reconstructing.

Menezes, J. C. and Mistry, J., 1993, "Vibration Tests of Liquid Storage Thin Cylindrical Vessels", RBCM - J. of the Braz. Soc. Mechanical Sciences, Vol 15, n. 1, pp. 31-41.

Theoretical investigations employing a Finite Element solution of the dynamic behavior of a cylindrical vessel filled with liquid have been published previously by the authors. This paper describes the experimental procedure utilised in the verification of the theoretical predictions of the coupled problem. Five steel specimens were prepared from thick tubes using a numerically controlled lathe. The base of the cylindrical specimens was attached to a large circular disk. Tests were carried out with the cylinders filled without any liquid in the first instance to determine and identify their natural frequencies. The cylinders were then filled to different heights with water and tested. The experimental procedure involved mounting the empty cylinder vertically on a shaker which was oscillated sinusoidally. The work describes a novel method of using only two piezoelectric accelerometers and placing them at two pre-determined angular locations, for the clear identification of the circumferential wave numbers of the normal modes.
Keywords: Fluid Structure Interation, Vibration Tests, Liquid Storage Vessels.

Dedini, F. G. and Cheli, F., 1993, "Modal Parameters Identification Techniques for Supporting Structure in Rotating Machinery Vibrations", RBCM - J. of the Braz. Soc. Mechanical Sciences, Vol 15, n. 1, pp. 42-53.

The frequency response of a rotating machine can be significantly affected by the dynamic behaviour of the supporting structure. This paper presents an experimental verification of two identification methods based on the comparison between the experimental frequency response measured at the journal bearings and the theoretical values obtained through a mathematical model of the system. In this case, an inaccurate evaluation of the bearings stiffness and damping coefficients can significantly affect the theoretical frequency response of the rotor. So, the oil film forces at the bearings were measured and compared with those obtained using the equivalent stiffness and damping coefficients analytically evaluated and the experimental displacement data at the bearings.
Keywords: Identification, Foundation, Bearings, Oil film, Frequency response

Pacheco, P. M. C. L., Hubscher, F. P. and Mattos, H. C., 1993, "High Temperature Lifetime Prediction in Metallic Materials Subjected to Cyclic Loadings", RBCM - J. of the Braz. Soc. Mechanical Sciences, Vol 15, n. 1, pp. 54-64.

The present paper is concerned with the high temperature lifetime prediction in metallic materials. It is proposed an elasto-viscoplastic constitutive model, developed within the framework of Continuous Damage Mechanics, that takes into account the coupling between the creep and low-cycle fatigue mechanism. The basic features of this model are shown by simulating a stainless steel bar subjected to cyclic loadings at different temperatures. The applicability and the usefulness of the theory are verified by means of examples concerning the lifetime prediction of a stainless steel pipe at 600°C under complex pressure loadings.
Keywords: High Temperature Lifetime Prediction, Continuous Damage Mechanics, Creep, Fatigue, Mettalic Materials

Almeida, A. F. B. and Rios-Neto, A., 1993, "A Survey on the Orbit Transfer Problem" (in Portuguese), RBCM - J. of the Braz. Soc. Mechanical Sciences, Vol 15, n. 1, pp. 65-78.

This paper presents the results obtained from a search in the literature about the problem of minimum fuel consumption spacecraft orbit transfer. The problem and several of its models are presented to allow a non-expert reader to understand them. More than one hundred papers are discussed allowing the reader to have a first idea about their contents before a more detailed study. The majority of these papers are available in Brazilian libraries.
Keywords: Orbit Transfer, Spacecraft Maneuvers, Satellite Orbit Control.

Cruz, G. M. M., 1993, "Numerical Simulation in Grid-Generated Turbulent Flows with the K-ε Model and one Equation for the Temperature Fluctuations" (in Portuguese), RBCM - J. of the Braz. Soc. Mechanical Sciences, Vol 15, n. 1, pp. 79-87.

In order to predict the temperature fluctuations in turbulent flows, we have used a turbulence model with three transport equations for mean square temperature variance, turbulent kinetic energy and the rate of kinetic energy dissipation. The governing field equations are the Navier-Stokes, continuity and energy equations. The finite volume method is employed to solve numerically these equations. The results of calculations with this model are compared with the measures of two experiments. The first one, an homogeneous hot turbulence below a grid (Warhaft and Lumley, 1978), allows us to test the model in a configuration with a constant mean temperature. The second experiment, a grid turbulence with cross-stream temperature gradient (Sirivat e Warhaft, 1982), allows us to test the model in a situation where the generation rate term of θ^2 due to mean temperature gradient plays an important part.
Keywords: Turbulence, Grid-generated flows, Temperature Fluctuations, k-ε model.

Wang, A. T. A. and Hartnett, J. P., 1993, "Pool Boiling of Aqueous Polyacrylamide Solutions: The Influence of Two Surface Active Agents", RBCM - J. of the Braz. Soc. Mechanical Sciences, Vol 15, n. 1, pp. 88-100.

The influence of surfactants on the pool boiling behavior of aqueous polyacrylamide solutions has been studied. The test section consisted of an electrically heated horizontal platinum wire submerged in a saturated pool of liquid at atmospheric pressure. The polymer selected for these studies was Separan AP-30, an anionic polyacrylamide. Two surfactants were used in these studies, the anionic sodium lauryl sulfate (SLS), and the non-ionic polyoxyethylene sorbitan monooleate (Tween-80).
Various combinations of polyacrylamide and surfactant dissolved in deionized water were studied. For each solution the steady shear viscosity h, the dynamic phase shift angle (a measure of elasticity) d, and the surface tension s were measured. In general, the values of h and d are dominated by the amount of polymer additive, whereas the values of s are dominated by the surfactant concentration. The presence of surfactants generally results in a decrease in elasticity relative to the values found for the aqueous polyacrylamide solution.
The surface tension values of the aqueous solution of SLS or Tween-80 were significantly lower than the values for deionized water. Surprisingly the boiling performance of the aqueous surfactant solutions did not differ from that found for water alone. For the 250 wppm aqueous Separan solution the boiling performance is inferior to that found for deionized water alone.
The presence of the surfactant Tween-80 in the aqueous polyacrylamide solution resulted in a reduction in the surface tension but the boiling performance was not affected. In contrast, the presence of SLS in the 250 wppm

aqueous polyacrylamide solution resulted in a significant increase in the heat transfer coefficient relative to the boiling performance of deionized water.

On the basis of these results, it can be concluded that lowering the surface tension of an aqueous polymer solution does not guarantee enhancement of the boiling heat transfer performance. Therefore the enhancement in boiling heat transfer reported earlier for aqueous Natrosol solutions is not due to its lower surface tension value.

Keywords: Non-Newtonian Fluids, Pool Boiling, Heat Transfer Enhancement, Experimental Methods

Moura, L. F. M. and Carneiro, F. A. S., 1993, "Numerical Simulation of Two-Phase Flow Separation in a T-junction", RBCM - J. of the Braz. Soc. Mechanical Sciences, Vol 15, n. 1, pp. 101-108.

The principal objective of this paper is to investigate numerically the gas-liquid phase separation in a vertical T-junction. A two-dimensional computer code was used to solve the two-fluid model equations, using the finite volume method. Special attention is directed to the modeling of the viscous diffusion term and the constitutive equation for the interfacial friction term.

The phase separation was simulated considering two different values of the branch to inlet diameter ratio, 0.5 and 1.0, according to the reported experimental results. The flow conditions in the T-junction inlet were related to the churn-turbulent flow pattern.

Detailed distributions of the void fraction, pressure and velocity of both phases are presented. A good agreement was obtained between the computer code results and the experimental data. For the mass split ratios greater then 0.3, the mean deviation was about 10%. However, for lower split ratios, a three-dimensional model would be more suitable. This work includes also the investigation of the boundary conditions, gravity, viscosity and mesh size on the phase separation phenomena.

Keywords: Numerical Simulation, Two-Phase Flow, T-junction

Information for Authors

SCOPE AND POLICY

- The purpose of the Journal of the Brazilian Society of Mechanical Sciences is to publish papers of permanent interest dealing with research, development and design related to science and technology in Mechanical Engineering, encompassing interfaces with Civil, Electrical, Chemical, Naval, Nuclear, Agricultural, Materials, Petroleum, Aerospace, Food, System Engineering, etc., as well as with Physics and Applied Mathematics.
- The Journal publishes Full-Length Papers, Review Papers and Letters to the Editor. Authors must agree not publish elsewhere a paper submitted to and accepted by the Journal. Exception can be made for papers previously published in proceedings of conferences. In this case it should be cited as a footnote on the title page. Copies of the conference referees reviews should be also included. Review articles should constitute a critical appraisal of published information.
- The decision of acceptance for publication lies with the Editors and is based on the recommendations of at least two ad hoc reviewers, and of the Editorial Board, if necessary.

SUBMISSION

- Manuscripts and all the correspondence should be sent to the Editor or, alternatively, to the appropriate Associate Editor.
- Four (4) copies of the manuscript are required. The author should submit the original figures, which will be returned if the paper is not accepted after the review process.
- Manuscripts should be submitted in English or Portuguese. Spanish will also be considered.
- A manuscript submitted for publication should be accompanied by a cover letter containing the full name(s) of author(s), mailing adresses, the author for contact, including phone and fax number, and, if the authors so wish, the names of up to five persons who could act as referees.

FORMAT

- Manuscripts should begin with the title, including the english title, the abstract and up to five key words. If the paper's language is not English, an extended summary of about 500 words should be included. The manuscript should not contain the author(s) name(s).
- In research papers, sufficient information should be provided in the text or by refering to papers in generally available Journals to permit the work to be repeated.
- Manuscripts should be typed double-spaced, on one side of the page, using A-4 sized paper, with 2 cm margins. The pages should be numbered and not to excess 24 pages, including tables and figures. The lead author of a RBCM paper which exceeds the standard length of pages will be assessed a excess page charge.
- All symbols should be defined in the text. A separate nomenclature section should list, in alphabetical order, the symbols used in the text and their definitions. The greek symbols follow the English symbols, and are followed by the subscripts and superscripts. Each dimensional symbol must have SI (Metric) units mentioned at the end. In addition, English units may be included parenthetically. Dimensionless groups and coefficients must be so indicated as dimensionless after their definition.
- Uncertainties should be specified for experimental and numerical results.

ILLUSTRATIONS AND TABLES

- Figures and Tables should be referred in consecutive arabic numerals. They should have a caption and be placed as close as possible to the text first reference.
- Line drawings should be prepared on tracing paper or vellum, using India ink; line work must be even and black. Laser print output is acceptable. The drawings with technical data/results should have a boundary on all four sides with scale indicators (tick marks) on all four sides. The legend for the data symbols should be put in the figure as well as labels for each curve wherever possible.
- Illustrations should not be larger than 12 x 17 cm. Lettering should be large enough to be clearly legible (1.5-2.0 mm).
- Photographs must be glossy prints.

REFERENCES

- References should be cited in the text by giving the last name of the author(s) and the year of publication of the reference: either "Recent work (Smith and Jones, 1985) ... or "Recently Smith and Jones (1985) With four or more names, use the form "Smith et al.(1985)" in the text. When two or more references would have the same text identification, distinguish them by appending "a", "b", etc., to the year of publication.
- Acceptable references include: journal articles,dissertations, published conference proceedings, numbered paper preprints from conferences, books, submitted articles if the journal is identified, and private communications.
- References should be listed in alphabetical order, according to the last name of the first author, at the end of paper. Some sample references follow:

Bordalo, S.N., Ferziger, J.H. and Kline, S.J., 1989, "The Development of Zonal Models for Turbulence", Proceedings, 10th ABCM - Mechanical Engineering Conference, Vol. I, Rio de Janeiro, Brazil, pp. 41-44.

Clark, J.A., 1986, Private Communication, University of Michigan, Ann Arbor, MI.

Coimbra, A.L., 1978, "Lessons of Continuum Mechanics", Editora Edgard Blucher Ltda, São Paulo, Brazil.

Kandlikar, S.G. and Shah, R.K., 1989, "Asymptotic Effectiveness - NTU Formulas for Multiphase Plate Heat Exchangers", ASME Journal of Heat Transfer, Vol. 111, pp. 314-321.

McCormak, R.W., 1988, "On the Development of Efficient Algorithms for Three Dimensional Fluid Flow", Journal of The Brazilian Society of Mechanical Sciences, Vol. 10, pp. 323-346.

Silva, L.H.M., 1988. "New Integral Formulation for Problems in Mechanics", (in portuguese), Ph.D. Thesis, Federal University of Santa Catarina, Florianópolis, SC, Brazil.

Sparrow, E.M., 1980a, "Forced-Convection Heat Transfer in a Duct Having Spanwise-Periodic Rectangular Protuberances", Numerical Heat Transfer, Vol. 3, pp. 149-167.

Sparrow, E.M., 1980b, "Fluid-to-Fluid Conjugate Heat Transfer for a Vertical Pipe-Internal Forced Convection and External Natural Convection", ASME Journal of Heat Transfer, Vol. 102, pp. 402-407.

ISSN 0100 - 7386

REVISTA BRASILEIRA DE CIÊNCIAS MECÂNICAS
JOURNAL OF THE BRAZILIAN SOCIETY OF MECHANICAL SCIENCES

VOL. XV - Nº 1 - 1993

Non-Linear Vibration

Acoustics

Fluid Structure Interaction

Rotating Machinery

Fatigue end Fracture

Space Mechanics

Turbulent Flow

Boiling

Two-Phase Flow